A COUPLED MODELLING ATTEMPT OF HYDRODYNAMICS AND ECOSYSTEM OF NORTHERN LEVANTINE BASIN

A THESIS SUBMITTED TO
THE INSTITUTE OF MARINE SCIENCES
OF
MIDDLE EAST TECHNICAL UNIVERSITY

BY

ALİ AYDOĞDU

IN PARTIAL FULFILLMENT OF THE REQUIREMENTS
FOR
THE DEGREE OF MASTER OF SCIENCE
IN
PHYSICAL OCEANOGRAPHY

JULY 2012

Approval of the thesis:

A COUPLED MODELLING ATTEMPT OF HYDRODYNAMICS AND ECOSYSTEM OF NORTHERN LEVANTINE BASIN

submitted by **ALİ AYDOĞDU** in partial fulfillment of the requirements for the degree of **Master of Science in Physical Oceanography Department, Middle East Technical University** by,

Prof.Dr. Ahmet Erkan Kıdeyş _____
Head of Institute, Institute of **Marine Sciences**

Prof. Dr. Emin Özsoy _____
Head of Department, **Physical Oceanography**

Prof. Dr. Emin Özsoy _____
Supervisor, **Physical Oceanography**

Examining Committee Members:

Prof. Dr. Emin Özsoy
Institute of Marine Sciences, METU _____

Dr. Heather Cannaby
Institute of Marine Sciences, METU _____

Assoc. Prof. Mustafa Koçak
Institute of Marine Sciences, METU _____

Date: _____

I hereby declare that all information in this document has been obtained and presented in accordance with academic rules and ethical conduct. I also declare that, as required by these rules and conduct, I have fully cited and referenced all material and results that are not original to this work.

Name, Last Name: ALİ AYDOĞDU

Signature :

ABSTRACT

A COUPLED MODELLING ATTEMPT OF HYDRODYNAMICS AND ECOSYSTEM OF NORTHERN LEVANTINE BASIN

Aydoğdu, Ali

M.S., Department of Physical Oceanography

Supervisor : Prof. Dr. Emin Özsoy

July 2012, 96 pages

A three-dimensional ocean model, ROMS, has been utilized to simulate the hydrodynamics and the ecosystem dynamics of the Northern Levantine Basin circulation. The model is one-way nested inside a coarser resolution Mediterranean Sea eco-hydrodynamics model, forced with realistically updated surface and lateral fluxes of momentum, mass, heat and nutrients. Scenario runs representing present and future time-slices of 5 years each have been used to investigate sensitivity to climate in the near future. Other sensitivity tests depending on model parameters and options have been performed. It is revealed that the Asia Minor Current, dominating the basin circulation, divides the basin into the two basic regions of coastal and open sea characteristics. Although satisfactory results are reached for the general behaviour of the ecosystem, the model tends to overestimate the surface chlorophyll concentration. Sea surface patterns of variables predicted by the model are compared with satellite data indicate general agreement in the seasonal patterns. Based on the selected climate change scenario for 30-40 year difference of the time slices, rises of 0.33° C and 0.035 respectively in surface temperature and salinity are estimated in daily average properties. As a result, surface chlorophyll concentrations are increased by 8%. Moreover, significant changes in the periodicity of seasonal phytoplankton blooms are found. Results of the parameter and option sensitivity

tests have revealed the need for better representation of surface fluxes and a careful tuning of the mixing achieved by the model, especially at the surface levels. Sensitivity runs also showed that the temperature and salinity at the surface were overestimated because of the need for better representation of the penetration of radiation in the surface waters. The results are promising, whereas there is need for further investigation of basic processes such as the Levantine Intermediate Water (LIW) formation.

Keywords: Eastern Mediterranean, Northern Levantine Basin, circulation, ecosystem model, climate

ÖZ

KUZEY LEVANT BASENİNİN HİDRODİNAMİĞİNİ VE EKOSİSTEMİNİ BÜTÜNLEŞİK MODELLEME ÇALIŞMASI

Aydoğdu, Ali
Yüksel Lisans, Fiziksel Oşinografi Bölümü
Tez Yöneticisi : Prof. Dr. Emin Özsoy

Temmuz 2012, 96 sayfa

Bu çalışmada Kuzey Levant Havzası akıntılarının hidrodinamik ve ekosistem özelliklerinin simülasyonu için bir üç boyutlu okyanus modeli (ROMS) kullanılmıştır. Model, daha düşük çözünürlüklü bir Akdeniz eko-hidrodinamik modelinden elde edilen verilerin gerçekçi şekilde güncellenmesiyle yüzey ve yan sınırlardan beslendi. Yakın zamanda iklime duyarlılığını araştırmak için geçmişteki ve gelecekteki 5 yıllık zaman aralıkları için senaryo çalışmaları yapıldı. Model parametrelerine ve seçeneklerine dayalı duyarlılık senaryoları da uygulandı. Sonuçlarda, havzayı etkisi altına alan Küçük Asya Akıntısı'nın baseni kıyı ve açık deniz şeklinde iki ana bölgeye böldüğü ortaya konuldu. Ekosistem dinamikleri için tatmin edici sonuçlar elde edilmesine rağmen, yüzey klorofil konsantrasyonları aşırı tahmin edildi. Yüzey dağılımları uydu resimleriyle karşılaştırıldığında genel bir uyum gözlenmiştir. 30-40 yıl sonrası için gerçekleştirilen iklim değişikliği senaryosu, yüzey sıcaklığının ve tuzluluğunun günlük ortalama değerlerinde sırasıyla 0.33° C ve 0.035 psu artış hesaplanmıştır. Bunun yanında, yüzey klorofil ortalamalarında da %8'lik bir artış tahmini yapılmıştır. Ayrıca, fitoplankton verimliliğinin en fazla olduğu dönemlerde de zamansal kayma olduğu belirlendi. Model parametreleri ve seçeneklerinin duyarlılıklarını belirlemek amacıyla gerçekleştirilen testler yüzey akılarının ve karışımın daha iyi ayarlanması gerektiğini ortaya koymuştur. Du-

yarlılık testleri, ek olarak, yüzey sıcaklık ve tuzluluk değerlerinin gerektiği gibi ayarlanmamış atmosferik ışıma dolayısıyla aşırı tahmin edildiğini göstermiştir. Genel olarak sonuçların tatmin edici olduğu söylenebilmekle beraber, Levant Ara Suyu oluşumu gibi süreçlerin daha fazla araştırmaya ihtiyaç duyduğu belirtilemelidir.

Anahtar Kelimeler: Doğu Akdeniz, Kuzey Levant Havzası, sirkülasyon, ekosistem modellemesi, iklim

Annem Şerife'ye ve Babam Tuncay'a

ACKNOWLEDGMENTS

I would like to thank to Prof. Emin Özsoy for supervising this thesis and supporting me in any aspect since I came to IMS-METU. Adil Sözer, a fellow doctoral candidate, has acted as if he is my unofficial co-supervisor during this study. I learned from him a lot and owe to him a great deal. Also Sinan Hüsrevoğlu was a perfect guide at the beginning of my graduate education. I wish we could study together for a longer period.

I want to thank to my friend and flat-mate Özge Yelekçi for her patience and sharing her priceless comments on the study. My friends and collegues Ersin Tutsak, Çağlar Yumruktepe and Özgür Gürses have had great contributions during this study. I thank all of them.

The members of the examining committee, Dr. Heather Cannaby and Dr. Mustafa Koçak, generously shared their experience and knowledge during revisions. Thanks to them for their valuable contributions.

No collective progress could be achieve without the help of the non-academic members of IMS-METU. I would like to thank them all.

My friends Dilek Kadıoğlu, Erman Pulgat, Mustafa Kaplan and Erçin Savur have encouraged and supported me in any occasion. I can't just pass without mentioning their names.

And finally, I want to thank to my family for everything, and to my nephew, Meriç, for being my joy of living in the last two years.

TABLE OF CONTENTS

ABSTRACT iv

ÖZ vi

ACKNOWLEDGMENTS ix

TABLE OF CONTENTS x

LIST OF TABLES xiii

LIST OF FIGURES xiv

CHAPTERS

1 INTRODUCTION 1

1.1 Aim of the Study 1

1.2 Overview of the Study Area 3

1.2.1 Geometry and General Topography 3

1.2.2 Meteorology and Hydrodynamic Structure 5

1.2.3 Biochemistry and Northern Levantine Rivers 10

2 REGIONAL OCEAN MODELING SYSTEM 14

2.1 Model Description 15

2.1.1 Equations of Motion 15

2.1.2 Boundary Conditions 16

2.1.2.1 Vertical boundary conditions 16

2.1.2.2 Horizontal boundary conditions 17

2.1.3 Coordinate Systems 18

2.1.3.1 Terrain-following coordinate system 18

2.1.3.2 Horizontal curvilinear coordinates 19

2.2 Numerical Solution Technique 20

2.2.1 Vertical and horizontal discretization 20

2.2.1.1 Vertical grid 20
2.2.1.2 Horizontal grid 20
2.2.2 Timestepping 21
2.2.3 Advection schemes 21
2.2.4 Vertical and horizontal mixing 22
2.3 Ecosystem Modules 22
2.3.1 Fennel ecosystem submodel 23
3 NORTHERN LEVANTINE BASIN MODEL (NLEV) SETUP AND RUN DATA 26
3.1 Bathymetry 27
3.2 1996-2000 and 2030-2034 Coupled Simulations 27
3.2.1 Model Setup 27
3.2.2 Initialization 29
3.2.3 Boundary Fluxes 29
3.2.4 Surface Atmospheric Forcing 32
3.3 2009 Hydrodynamical Simulations 34
3.3.1 Model Setup 34
3.3.2 Initialization 36
3.3.3 Boundary Fluxes 36
3.3.4 Atmospheric Surface Forcings 36
3.4 River input 37
4 RESULTS 40
4.1 General Circulation 41
4.2 Vertical Mixing 49
4.3 Thermohaline Structure 55
4.4 Validation 58
4.4.1 Sea Surface Temperature (SST) 59
4.4.2 Sea Level Anomaly (SLA) 63
4.4.3 Sea Surface Chlorophyll 67
4.5 Ecosystem 70
4.6 Comparison of 1996-2000 and 2030-2034 Simulations 74

4.7 Improvements for Hydrodynamical Model 80
5 DISCUSSIONS and CONCLUDING REMARKS 83
REFERENCES 86
A LIST OF ABBREVIATIONS 91
B BIOGEOCHEMISTRY cont'd 92

LIST OF TABLES

TABLES

Table 2.1 The variables used in the description of the ocean model 16

Table 2.2 The variables used in the vertical boundary conditions for the ocean model . 17

Table 3.1 Parameters used in the Fennel ecosystem model 29

Table 3.2 Comparison of spatio-temporal averages of atmospheric parameters for simulations 1996-2000 and 2030-2034 33

Table 3.3 Switches used sensitivity test runs of hydrodynamical model 36

Table 3.4 Monthly water discharges ($m^3 s^{-1}$) of the Northern Levantine rivers included in simulation 1996-2000 38

Table 3.5 Monthly NO_3 discharges (μM) of the Northern Levantine rivers included in simulation 1996-2000 38

Table 3.6 Monthly NH_4 discharges (μM) of the Northern Levantine rivers included in simulation 1996-2000 38

Table 4.1 Comparison of surface and total basin spatio-temporal averages of model variables for simulations 1996-2000 and 2030-2034 77

LIST OF FIGURES

FIGURES

Figure 1.1 Geometry and Topography of the Mediterranean Sea and the Northern Levantine Basin 4

Figure 1.2 MODIS-Aqua April2008 and September2008 SST distributions in the Eastern Mediterranean 5

Figure 1.3 General Circulation of the Mediterranean Sea (adapted from Robinson et al., 2001) 6

Figure 1.4 Water formations in the Northern Levantine Basin (adapted from Malanotte-Rizzoli et al., 1999) 7

Figure 1.5 General Surface Circulation of the Eastern Mediterranean Sea (adapted from Robinson et al., 2001) 9

Figure 1.6 MODIS-Aqua April2008 and September2008 surface chlorophyll distributions in the Eastern Mediterranean 11

Figure 1.7 Monthly averages of MODIS-Aqua surface chlorophyll in the five different regions of the Levantine Sea 12

Figure 1.8 Vertical profiles of (a) Dissolved Oxygen (b) Nitrate (c) Phosphate (d) Silicate (e) Chlorophyll-a annually in three different regions of Eastern Mediterranean (retrieved from Manca et al., 2004) 13

Figure 2.1 Placement of variables on (a) staggered vertical grid (b) Arakawa C-grid . 21

Figure 2.2 Fennel model scheme (Adapted from Fennel et al., 2006) 25

Figure 3.1 Horizontal Curvilinear Grid 28

Figure 3.2 Vertical Staggered Grid 28

Figure 3.3 Initial surface data for hydrodynamic variables temperature, salinity, velocity, sea surface height (from top-left to bottom-right, respectively) 30

Figure 3.4 Initial surface data for ecosystem variables chlorophyll, phytoplankton, zooplankton, total inorganic carbon (from top-left to bottom-right, respectively) . 30

Figure 3.5 Initial surface data for ecosystem variables NH4, NO3, oxygen, alkalinity (from top-left to bottom-right, respectively) 31

Figure 3.6 Initial surface data for ecosystem variables large nitrogen detritus, large carbon detritus, small nitrogen detritus, small carbon detritus (from top-left to bottom-right, respectively) 31

Figure 3.7 Temporal average of wind stress for years 1996-2000 32

Figure 3.8 Temporal wind speed variation for 5-year time sliced hydrodynamics-ecosystem coupled simulations and 2009 hydrodynamical simulations 33

Figure 3.9 Temporal long wave radiation variation for 5-year time sliced hydrodynamics-ecosystem coupled simulations and 2009 hydrodynamical simulations 33

Figure 3.10 Temporal short wave radiation variation for 5-year time sliced hydrodynamics-ecosystem coupled simulations and 2009 hydrodynamical simulations 34

Figure 3.11 Temporal surface air temperature variation for 5-year time sliced hydrodynamics-ecosystem coupled simulations and 2009 hydrodynamical simulations 34

Figure 3.12 Temporal surface air pressure variation for 5-year time sliced hydrodynamics-ecosystem coupled simulations and 2009 hydrodynamical simulations 35

Figure 3.13 Temporal surface air relative humidity variation for 5-year time sliced hydrodynamics-ecosystem coupled simulations and 2009 hydrodynamical simulations 35

Figure 3.14 Temporal rain fall variation for 5-year time sliced hydrodynamics-ecosystem coupled simulations and 2009 hydrodynamical simulations 35

Figure 3.15 Temporal cloud fraction variation for 5-year time sliced hydrodynamics-ecosystem coupled simulations and 2009 hydrodynamical simulations 35

Figure 3.16 Monthly fluxes of (a) water discharge, (b) NO_3, (c) NH_4 for the Northern Levantine rivers 39

Figure 4.1 Daily spatial maximum and average of current speed between years 1996 and 2000 at depths 0m, 10m, 20m, 50m, 100m, 500m, 1000m 41

Figure 4.2 Monthly averaged sea surface circulation between 1996-2000 in January, February, March, April, May and June 43

Figure 4.3 Monthly averaged sea surface circulation between 1996-2000 in July, August, September, October, November and December 44

Figure 4.4 Monthly averaged circulation for 28.95E (Rhodes Gyre) and 36.02N (AMC) horizontal section between 1996-2000 in January, February, March 45

Figure 4.5 Monthly averaged circulation for 28.95E (Rhodes Gyre) and 36.02N (AMC) horizontal section between 1996-2000 in April, May and June 46

Figure 4.6 Monthly averaged circulation for 28.95E (Rhodes Gyre) and 36.02N (AMC) horizontal section between 1996-2000 in July, August, September 47

Figure 4.7 Monthly averaged circulation for 28.95E (Rhodes Gyre) and 36.02N (AMC) horizontal section between 1996-2000 in October, November, December 48

Figure 4.8 Monthly averaged temperature for 28.95E (Rhodes Gyre) and 36.02N (AMC) horizontal sections over years 1996 - 2000 in January, February and March 50

Figure 4.9 Monthly averaged temperature for 28.95E (Rhodes Gyre) and 36.02N (AMC) horizontal sections over years 1996 - 2000 in April, May and June 51

Figure 4.10 Monthly averaged temperature for 28.95E (Rhodes Gyre) and 36.02N (AMC) horizontal sections over years 1996 - 2000 in July, August and September 52

Figure 4.11 Monthly averaged temperature for 28.95E (Rhodes Gyre) and 36.02N (AMC) horizontal sections over years 1996 - 2000 in October, November and December . 53

Figure 4.12 Monthly averaged vertical profile of temperature and salinity for 36.02N - 28.95E in Rhodes Gyre over years 1996 - 2000 54

Figure 4.13 Daily spatial MAXIMUM MINIMUM and MEAN of temperature between 1996 and 2000 at depths 0m, 10m, 20m, 50m, 100m, 500m, 1000m 55

Figure 4.14 Daily spatial MEAN MAXIMUM and MINIMUM of salinity between 1996 and 2000 at depths 0m, 10m, 20m, 50m, 100m, 500m, 1000m 56

Figure 4.15 Monthly averaged salinity at the surface between 1996-2000 in April . . . 56

Figure 4.16 TS-diagram of monthly averaged temperature and salinity at the surface for each month 57

Figure 4.17 Comparison of monthly averaged SST of PODAAC satellite and ROMS between 1996-2000 in January, February, March and April 60

Figure 4.18 Comparison of monthly averaged SST of PODAAC satellite and ROMS between 1996-2000 in May, June, July, August 61

Figure 4.19 Comparison of monthly averaged SST of PODAAC satellite and ROMS between 1996-2000 in September, October, November, December 62

Figure 4.20 Daily spatial MAXIMUM MINIMUM and MEAN of sea surface height between 1996 and 2000 63

Figure 4.21 Comparison of monthly averaged SLA of Aviso satellite and ROMS between 1996-2000 in January, February, March and April 64

Figure 4.22 Comparison of monthly averaged SLA of Aviso satellite and ROMS between 1996-2000 in May, June, July, August 65

Figure 4.23 Comparison of monthly averaged SLA of Aviso satellite and ROMS between 1996-2000 in September, October, November, December 66

Figure 4.24 Comparison of monthly averaged chlorophyll of SEAWIFS satellite and ROMS between 1996-2000 in January, February 67

Figure 4.25 Comparison of monthly averaged chlorophyll of SEAWIFS satellite and ROMS between 1996-2000 in March, April, May, June, July 68

Figure 4.26 Comparison of monthly averaged chlorophyll of SEAWIFS satellite and ROMS between 1996-2000 in August, September, October, November, December 69

Figure 4.27 Time series for daily spatial MEAN of chlorophyll between 1996 and 2000 at depths 0m, 10m, 20m, 50m, 100m, 500m, 1000m 70

Figure 4.28 Monthly averaged vertical profile of chlorophyll for 36.02N - 28.95E grid point in Rhodes Gyre over years 1996 - 2000 71

Figure 4.29 Time series for daily spatial MEAN of phytoplankton between 1996 and 2000 at depths 0m, 10m, 20m, 50m, 100m, 500m, 1000m 72

Figure 4.30 Time series for daily spatial MEAN of zooplankton between 1996 and 2000 at depths 0m, 10m, 20m, 50m, 100m, 500m, 1000m 72

Figure 4.31 Time series for daily spatial MEAN and MAXIMUM of nitrate between 1996 and 2000 at depths 0m, 10m, 20m, 50m, 100m, 500m, 1000m 73

Figure 4.32 Monthly averaged vertical profile of nitrate for 36.02N (AMC) - 28.95E (Rhodes Gyre) over years 1996 - 2000 74

Figure 4.33 Time series for daily spatial MEAN of ammonium between 1996 and 2000 at depths 0m, 10m, 20m, 50m, 100m, 500m, 1000m 74

Figure 4.34 Time series for daily spatial surface and basin average of temperature along years 1996-2000 and 2030-2034 75

Figure 4.35 Time series for daily spatial surface and basin average of salinity along years 1996-2000 and 2030-2034 76

Figure 4.36 Time series for daily spatial surface and basin average of chlorophyll along years 1996-2000 and 2030-2034 76

Figure 4.37 Time series for daily spatial surface and basin average of current speed along years 1996-2000 and 2030-2034 77

Figure 4.38 Time series for daily spatial surface and basin average of chlorophyll along years 1996-2000 and 2030-2034 78

Figure 4.39 Time series for daily spatial surface and basin average of phytoplankton along years 1996-2000 and 2030-2034 78

Figure 4.40 Time series for daily spatial surface and basin average of zooplankton along years 1996-2000 and 2030-2034 79

Figure 4.41 Time series for daily spatial surface and basin average of nitrate along years 1996-2000 and 2030-2034 79

Figure 4.42 Time series for daily spatial surface and basin average of ammonium along years 1996-2000 and 2030-2034 80

Figure 4.43 Spatial average of sea level height for hydrodynamic test simulations . . . 80

Figure 4.44 Time series for spatial average of surface and basin current velocity for hydrodynamic test simulations 81

Figure 4.45 Time series for spatial average of surface and basin temperature for hydrodynamic test simulations 82

Figure 4.46 Time series for spatial average of surface and basin salinity for hydrodynamic test simulations 82

Figure B.1 Time series for daily spatial MEAN of oxygen between 1996 and 2000 at depths 0m, 10m, 20m, 50m, 100m, 500m, 1000m 92
Figure B.2 Time series for daily spatial MEAN of alkalinity between 1996 and 2000 at depths 0m, 10m, 20m, 50m, 100m, 500m, 1000m 92
Figure B.3 Time series for daily spatial MEAN of large carbon detritus between 1996 and 2000 at depths 0m, 10m, 20m, 50m, 100m, 500m, 1000m 93
Figure B.4 Time series for daily spatial MEAN of small carbon detritus between 1996 and 2000 at depths 0m, 10m, 20m, 50m, 100m, 500m, 1000m 93
Figure B.5 Time series for daily spatial MEAN of large nitrogen detritus between 1996 and 2000 at depths 0m, 10m, 20m, 50m, 100m, 500m, 1000m 93
Figure B.6 Time series for daily spatial MEAN of small nitrogen detritus between 1996 and 2000 at depths 0m, 10m, 20m, 50m, 100m, 500m, 1000m 94
Figure B.7 Time series for daily spatial surface and basin average of oxygen along years 1996-2000 and 2030-2034 94
Figure B.8 Time series for daily spatial surface and basin average of alkalinity along years 1996-2000 and 2030-2034 94
Figure B.9 Time series for daily spatial surface and basin average of large carbon detritus along years 1996-2000 and 2030-2034 95
Figure B.10 Time series for daily spatial surface and basin average of small carbon detritus along years 1996-2000 and 2030-2034 95
Figure B.11 Time series for daily spatial surface and basin average of large nitrogen detritus along years 1996-2000 and 2030-2034 95
Figure B.12 Time series for daily spatial surface and basin average of small nitrogen detritus along years 1996-2000 and 2030-2034 96

CHAPTER 1

INTRODUCTION

1.1 Aim of the Study

In this modelling study, the Northern Levantine Sea, located in northeastern Mediterranean, is chosen as the study area. Physical and biological structure of the Mediterranean is described by various observational programmes (e.g. POEM, SESAME) and modelling studies (e.g. *Zavatarelli and Mellor, 1995*; *Demirov and Pinardi, 2002*). A large number of sub-basin wide modelling studies on the Levantine Sea also exist (e.g. *Lascaratos et al., 1993*; *Alhammoud et al., 2005*).

The hydrodynamical structure of the Northern Levantine is important not only in its regional scale but also for the whole Mediterranean Sea and even the North Atlantic Ocean. Levantine Intermediate Water, which circulates across the Mediterranean and spreads into the Atlantic Ocean, is generated by air-sea interactions which is peculiar to the Northern Levantine and the Rhodes Basin (*Ovchinnikov, 1966*; *Özsoy et al., 1989*; *The POEM Group, 1992*; *Lascaratos et al., 1993*). Moreover, the Asia Minor Current, spreading to the Aegean Sea and the Ionian Sea through different channels, is one of the principal features of the surface circulation of the Levantine Basin. In addition, the Rhodes Gyre is another significant feature to study for determination of large scale and mesoscale hydrodynamical activities along the basin.

The Eastern Mediterranean is one of the most oligotrophic waters of the world ocean. The behaviour of lower trophic level in the ecosystem of the region, the response of ecosystem variables to different atmospheric forcings and the effects of rivers around Asia Minor on biology are some of the reasons to study the ecosystem of the Northern Levantine.

Motivated by the factors mentioned above, a study was carried out in the context of the European project entitled 'Southern European Seas: Assessing and Modelling Ecosystem Changes' (SESAME). Climate scenarios based on two 5-year time-slices with different atmospheric forcing and river flux data sets were tested on the regional level. The future climate of the next 30-40 years was based on the hydro-meteorological climate forecasts downscaled according to the IPCC global warming scenarios. Main objectives of this study were:

1. To modify and adapt Regional Ocean Modelling System (ROMS) according to the requirements of the study area for investigation of the regional circulation patterns, subbasin and mesoscale features, thermohaline properties and ecosystem components.

2. To reveal the effects of the variable atmospheric forcing on the circulation, vertical stratification and ecosystem dynamics of the basin on intermediate time scales of global warming.

3. To see the dispersion of river waters along the basin and their impact on the generally oligotrophic Northern Levantine basin ecosystem contrasted with the river dominated coastal / continental shelf areas (regions of fresh water influence - ROFI).

In the framework of these objectives, the following sections of this chapter are devoted to introductory background information for study area. Its meteorology, physical oceanography and ecosystem will be described in detail, to form a basis for the rest of the study required. Next two chapters will be on materials and methods used in this work. In Chapter 2, after giving a general opinion about Regional Ocean Modelling System (ROMS), principals related to this study will be elaborated. Data sets which are used to initialize and force the model at the surface and the boundries will be presented in Chapter 3, including the model configuration adapting ROMS to the study of the Northern Levantine basin. Results attained in this work will be the focus of Chapter 4. Results obtained on the circulation, hydrological and ecosystem structure will be presented and validated. Moreover, comparison of simulations on the effects of atmospheric variability linked to climate scenarios will be presented in this chapter. Some results on sensitivity tests to improve the hydrodynamical model are also decsribed. Finally, in Chapter 5, outcomes presented in Chapter 4 will be discussed in and concluding remarks be stated. Cited works and abbreviations used are listed at the end.

1.2 Overview of the Study Area

1.2.1 Geometry and General Topography

The Mediterranean Sea, surrounded by continents of Europe in the north, Africa in the south and Asia in the east, is a marginal and semi-enclosed sea (see *Fig. 1.1 in page 4* for the rest of section). It covers an area of 2.5 million km^2 and is 3700 *km* wide from west to east and 1600 *km* long from north to south. It is connected to the Atlantic Ocean via the Strait of Gibraltar. Dardanelles-Marmara-Bosphorus system connects the Mediterranean to the Black Sea. The average depth of the sea is 1500 *m* where the maximum is placed in the Ionian Sea with a 5150 *m* depth (*Lionello et al., 2006*).

The study area, the Northern Levantine basin is geographically located between 35.12*N* - 36.92*N* latitudes and 28.15*E* - 36.23*E* longitudes. Estimated total sea area is about 111000 km^2 (*Ludwig et al., 2009*).

Lateral boundaries of the basin are determined by highly indented Anatolian coasts from the north, Rhodes Island from west, Cyprus from south and coasts of İskenderun and Syria from east. Orographic features such as the Taurus Mountains in the north play important role in air-sea interactions and water formations along the basin. Three major gaps near the Gulf of İskenderun, the Goksu Valley and the Gulf of Antalya are passages for northerly winds to arrive at the Northern Levantine.

Various features on the bottom topography of the Northern Levantine lead to a very complex structure of bathymetry. Continental shelf is very narrow excluding the Gulf of İskenderun. Along most of the coasts, continental slope is very steep where 200 *m* depth is generally reached within 10 - 20 *km*. *Ludwig et al., 2009* states, in other words, that mean slope is 10.5 degrees. Depth increases towards the western part of the basin where bottom topography reaches its maximum at the Rhodes Trough with 4500 *m*. Other remarkable bathymetric features are settled in the Latakia Basin (1000 - 1500 *m*), in the Cilician Basin (1000 *m*) and the Finike Depression in the Gulf of Antalya (2000 - 3000 *m*). In addition, between Cyprus and the Gulf of İskenderun, there is a narrow channel of depth 700 *m* with which the Latakia and Cilician Basins communicate with each other (*Özsoy et al., 1993*). Finally, Anaximander Seamount (1500 *m*) is another significant bathymetric feature to mention.

The Northern Levantine is interconnected with other basins by a variety of channels. The Rhodes Straits, one of which is between Rhodes Island and Anatolian coast and the other

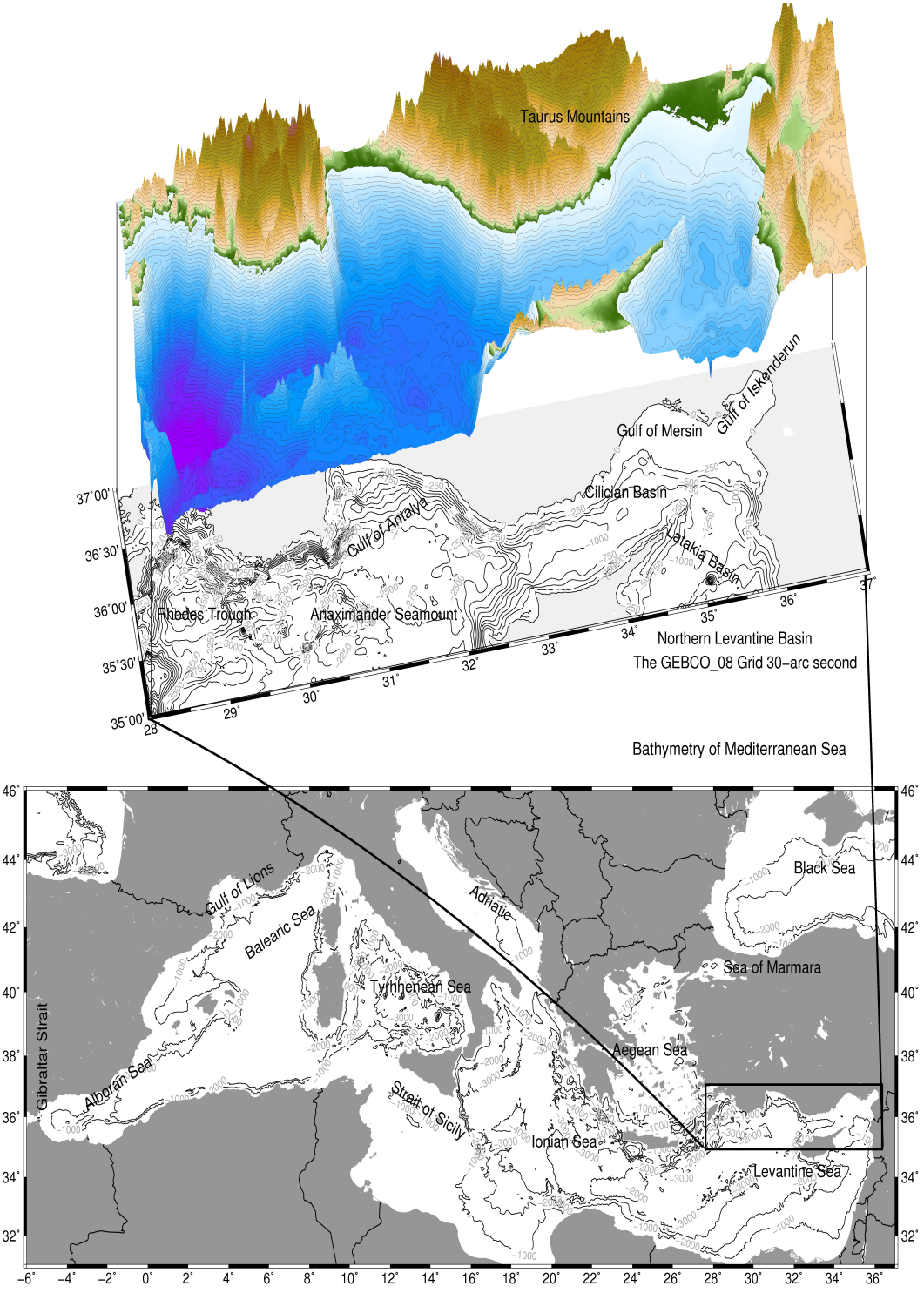

FIGURE 1.1: *Geometry and Topography of the Mediterranean Sea and the Northern Levantine Basin*

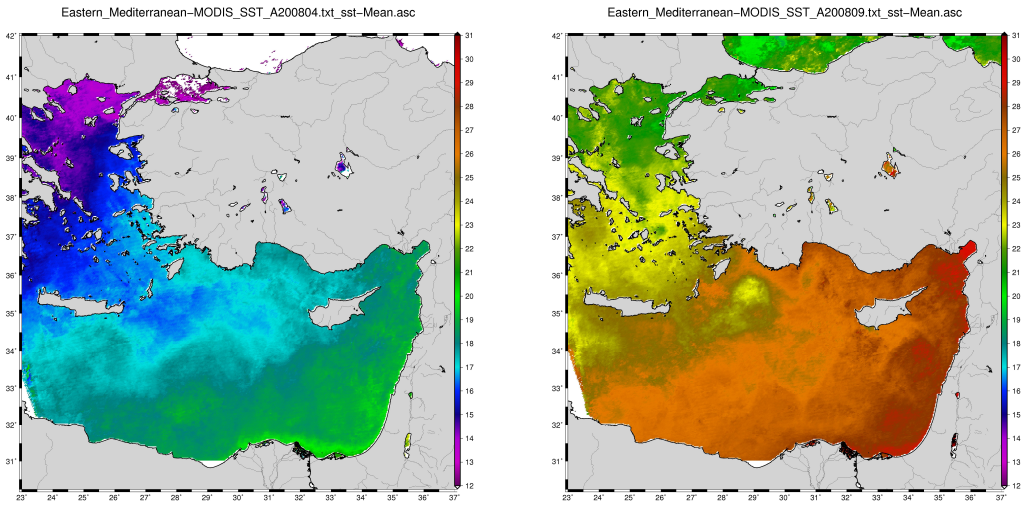

FIGURE 1.2: *MODIS-Aqua April2008 and September2008 SST distributions in the Eastern Mediterranean*

is between Karpathos and Rhodes Island, are main connections to the Aegean Sea. Cretan passages, which are not included in this study, are channels to the Adriatic and Ionian Seas.

Topography of the Northern Levantine is very important for the general circulation of the basin, since it directly influences the pathway of the Asia Minor Current. Moreover, occurence of the Rhodes Gyre and other mesoscale eddies along the basin, and formation of jet between the Latakia and Cilician Basins are particularly determined by bathymetry in addition to other leading factors (see section 1.2.2).

1.2.2 Meteorology and Hydrodynamic Structure

Climatic characteristics of the Mediterranean are determined by various different atmospheric systems and topographic features. The winter is mild, wet and windy whereas the summer is characterized by hot, dry and calm weather. Air temperature gradient between the winter and the summer is generally 15 °C (Fig. 1.2). Regionally, Mistral and Bora are known to be the main wind patterns ruling the Western Mediterranean. In the Eastern Mediterranean, especially in the Levantine Sea, in winter and spring, Poyraz and Sirocco winds are the main meteorological patterns while summer and autumn are dominated by the Westerlies, the Etesians and the northerly cold wind systems. In winter, strong cyclones originating frequently from the Ionian Sea and rarely from North Africa govern the dynamics of atmosphere over the the Levantine Sea. Approximately, 30 cyclones penetrate into the Northern Levantine

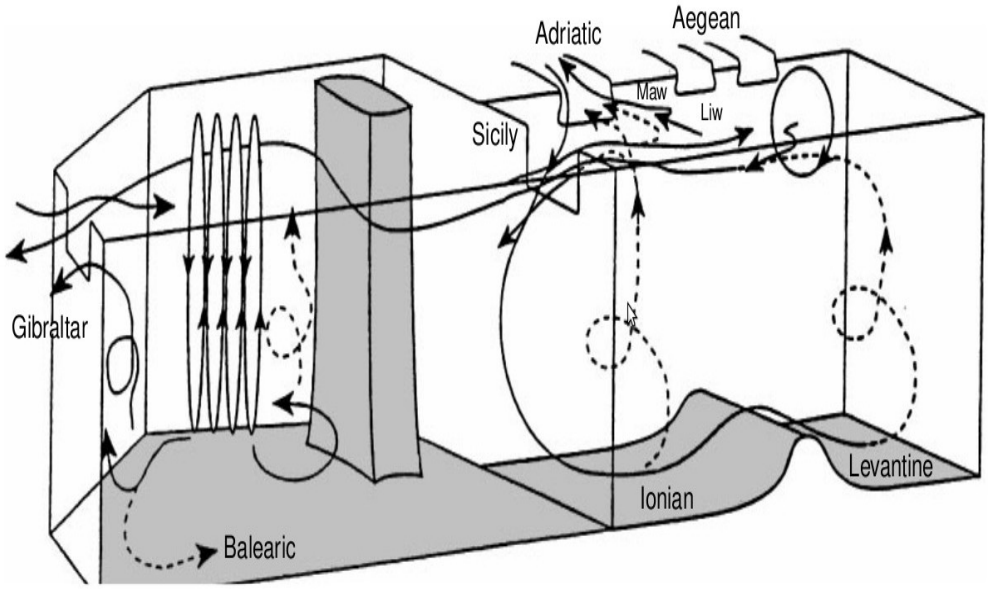

FIGURE 1.3: *General Circulation of the Mediterranean Sea (adapted from Robinson et al., 2001)*

during winters (*Özsoy et al., 1989*). In summer, a high pressure ridge is located near the Balkan Peninsula and there is a permanent low in the Persian Gulf which generates northerly The Etesians, whose magnitude and curl of wind stress is shown to be highest of the Eastern Mediterranean by *May (1982)*, over the Aegean Sea. As a result, mean wind stress over the basin is northwesterly with the combination of the Westerlies and the Etesians (*Özsoy, 1981; also see Fig. 3.7*). As cited in *Özsoy (1981)*, water budget lost by evaporation is calculated to be 1929 km^3 per year. Therefore, the Mediterranean is an arid sea where water loss by evaporation exceeds the water gain by river water discharge and precipitation. *Zavatarelli and Mellor (1995)* calculated that total heat flux in February shows a zonal pattern where largest negative values are around Rhodes for the Eastern Mediterranean. In August, positive heat flux occurs along the basin where lowest values are again in the Rhodes region.

Air-sea interactions and surface atmospheric forcings on the Mediterranean discussed briefly above, and in more detail by *Özsoy (1981)*, *Özsoy et al., (1989)*, *Reiter (1975)* and *Bethoux (1979)*, are crucial for circulation and hydrography of the sea. They play an important role in the formation of water masses with different characteristics as well as wind-driven large and mesoscale circulation components. These water formations lead to a thermohaline circulation which overturns whole Mediterranean (Fig. 1.3).

Different water masses present in the Northern Levantine are shown in Fig. 1.4. Probably, the most important of these four water masses is the Levantine Intermediate Water (LIW).

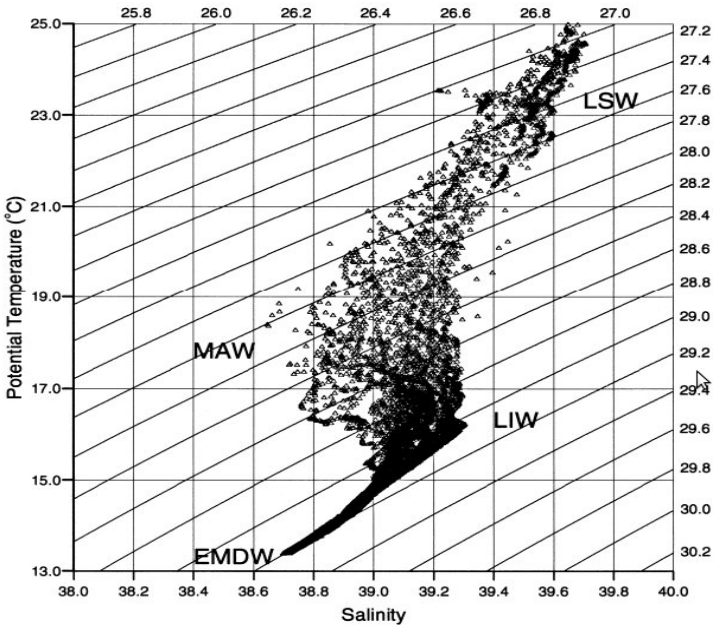

FIGURE 1.4: *Water formations in the Northern Levantine Basin (adapted from Malanotte-Rizzoli et al., 1999)*

Wüst (1961) states, because of positive net heat flux throughout year, which results in high sea surface temperature (>28 °C, see Fig. 1.2 in page 5) and evaporation rates, the Levantine Surface Water (LSW), which is a very important water mass in the formation of the LIW, becomes highly saline (> 39 psu). In winter, with the cooling due to the northerly Poyraz winds, these saline waters sink with a thermohaline convection upto 150 - 200 *m* depths. *Lascaratos et al. (1993)* claims signs of the LIW (15 - 16 °C in temperature and 38.95 - 39.05 psu in salinity) can be tracked down to 400 *m* depth in some areas. *Ovchinnikov (1966)* found that main region of formation for the LIW is between Rhodes and Cyprus. Later, Egyptian coast is also considered to be another source for the LIW (*Morcos, 1972*). These water masses thought to converge (*Özsoy et al., 1989*) and flow out of the Strait of Sicily with salinity ~38.7 psu. After circulating the Western Mediterranean at an intermediate depth of 300 - 700 *m*, the LIW leaves the basin through the Strait of Gibraltar from the bottom part of the sill and reaches the Northern Atlantic Ocean.

This thermohaline cell is closed by upper flow of the Strait of Gibraltar whih carries the Atlantic Water (AW) with low salinity (~36.25 psu) into the Mediterranean. Although salinity of the AW increases along its path to the Levantine Basin, the Modified Atlantic Water (MAW) can still be identified (see Fig. 1.4 and 1.5) in less saline ~38.5 psu) waters of 50 m depths (*Zavatarelli and Mellor, 1995*). 1 - 1.5 Sverdrup (10^6 m^3 s^{-1}) of total water change

of the LIW and the MAW is estimated through the Strait of Sicily (*The Poem Group, 1992*). Intrusion of the MAW into the Levantine Sea is still an open question. One hyphothesis, contructed on anaysis following POEM surveys and satellite data, says that the MAW, which then forms the Mid-Mediteranean Jet (MMJ) or the Central Levantine Basin Current (CLBC), crosses the Levantine by entring from the Strait of Sicily and flowing northeasterly where it breaks into two branches. One of these currents moves towards northwest and meets with the Asia Minor Current. The second branch is directed to the east where it splits into two again. One segment turns into the south of the basin (*Özsoy et al., 1989; The POEM Group, 1992; Robinson et al., 2001*). *Özsoy et al. (1993)* observed a penetration of the other branch into the Clician Basin from the east of Cyprus. *Zavatarelli and Mellor (1995)* were also able to simulate this behaviour in their modelling study. In more recent years, on the basis of some modelling studies, and analysis of SST and SSH satellite data, another route to the MAW is proposed. In 2005, Alhammoud claimed that the MAW moves southward after passing into the Levantine Sea and travels along North African coast before reaching the Northern Levantine. This hypothesis is later supported by *Hamad et al. (2006)*. *Amitai et al. (2010)* attributes the inconsistency between these two hypotheses to the change of flux of the current due to variability of eddy activities around the MMJ. One significant point about the AW flowing into the Mediterranean is that if there was no inflow from the Gibraltar Strait, sea level would decrease by 0.76 m per year due to high evaporation rate. This significant flow rate sets residence time of the Mediterranean as 97 years (citations in *Özsoy, 1981*).

Another important thermohaline circulation in the Eastern Mediterranean is utilized in formation of the Eastern Mediterranean Deep Waters (EMDW). The EMDW occupies a water column which is ~13.6 °C in temperature, ~38.7 psu in salinity and >29.05 $kg\ m^{-3}$ in density. During the POEM surveys, in 1987, (*The POEM Group, 1992*) it is revealed that the Adriatic Deep Water (ADW), which occurs as a result of deep convection in the Southern Adriatic, spreads into the bottom layer of the Eastern Mediterranean through the Otranto Straits and forms the EMDW. Upwelling events in the Eastern Mediterranean lead these waters to return into the Adriatic closing the thermohaline cell. However, in 1995, it is observed that main source of the EMDW is shifted to the Aegean Sea. Dense water masses of the Aegean Sea exit from the Cretan Arc Straits and spread throughout the Ionian and the Levantine Seas. Mentioned shift in region of the EMDW formation is studied under the topic Eastern Mediterranean Transient (*Malanotte-Rizzoli et al., 1999*).

In addition to these thermohaline cells, there are also important sub-basin scale and

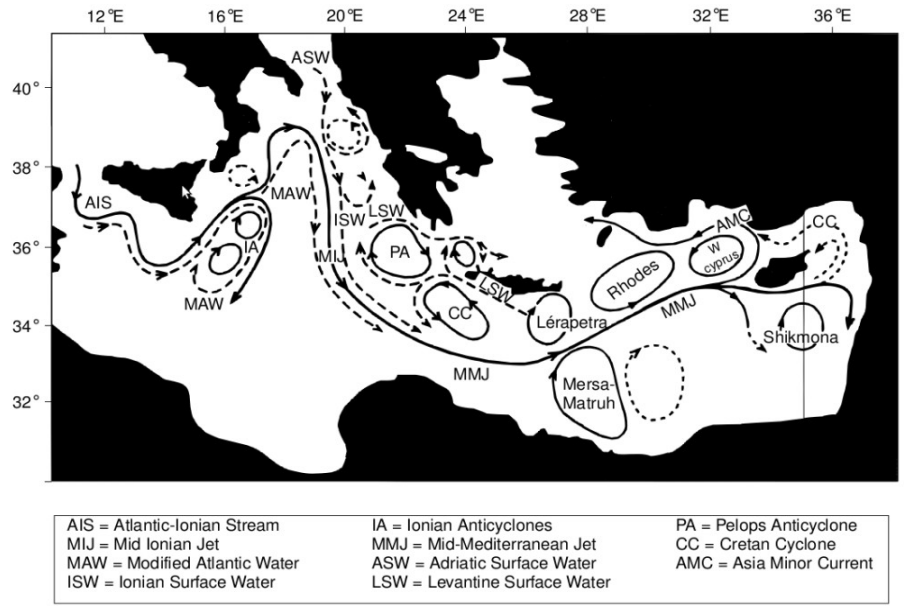

FIGURE 1.5: *General Surface Circulation of the Eastern Mediterranean Sea (adapted from Robinson et al., 2001)*

mesoscale components of general circulation in the Levantine Sea (Fig. 1.5). Remarkable circulation features in northern part of the Levantine Basin are westerly Asia Minor Current (AMC), cyclonic Rhodes Gyre, Anaximander and Antalya anti-cyclonic eddies, and West Cyprus cyclonic eddy. In the Southern Levantine, anti-cyclonic Mersa-Matruh Gyre and Shikmona anti-cyclonic eddy are spectacular patterns (*Özsoy et al., 1993; Malanotte-Rizzoli et al., 1999*).

The energetic Asia Minor Current (AMC) enters into the Cilician Basin from the Latakia and meanders along the whole Anatolian coast and exits to the Aegean and the Ionian Seas from channels around Rhodes and Crete Islands in the west. *Wu and Haines (1998)* claim total disapperence of flow in summer whereas the mean flow gets stronger during autumn, winter and spring. *Alhammoud et al. (2005)* modelling attempt shows a 35 $cm\ s^{-1}$ current speed of the AMC in winter. Their results also support the consideration of lower speed of velocity in summer.

One of the conclusions stated in *The POEM Group (1992)* emphasizes that sub-basin scale gyres are the "building blocks" of general circulation of the Mediterranean Sea. Among these cyclonic and anti-cyclonic features, the Rhodes Gyre is probably the most crucial one being resposible for the formation of the LIW. The Rhodes Gyre, a permanent cyclonic structure which has a diameter of 300 *km*, centered at 36°N and 28.5°E between Rhodes Island and

southern border of Turkey (*Milliff and Robinson, 1992*). Water column at the core of Rhodes Gyre is observed to have constant density, except the first 100 m which is exposed to strong atmospheric conditions (*Özsoy et al., 1993*). Intensity of the gyre changes seasonally, getting less in winter *(Özsoy et al., 1989)*.

The anti-cyclonic Anaximander and Antalya eddies are mainly governed by bathymetry of the region. *Özsoy et al. (1989)* relates occurence of an anti-cyclonic eddy over a seamount (Anaximander) near a cyclonic gyre (Rhodes Gyre) located over a trough to the bathymetric features under the formations. This argumentation is also relevant for Antalya anti-cyclonic eddy on Finike Trough.

1.2.3 Biochemistry and Northern Levantine Rivers

Major rivers of Mediterranean are situated in western part of the sea. The Rhone, the Po and the Ebro are the biggest fresh water sources for the Western Mediterranean. In the Eastern Mediterranean, the Nile river feeds the Southern Levantine and Seyhan, Ceyhan and Asi (Orontes) rivers run off into the northern part of the basin. Different average fresh water fluxes into the Mediterranean are estimated which range between 403 - 737 $km^3\ yr^{-1}$ in various sources in literature (see citations in *Ludwig et al., 2009*). *Ludwig et al. (2009)* calculated the range of annual fresh water discharge into the Northern Levantine between 20 - 49 $km^3\ yr^{-1}$. Nutrient load of the Northern Levantine rivers stay in moderate levels compared to other sub-basins of the Mediterranean. For 1998, budgets of the rivers for nitrogen, phosphorus and silica are given by Ludwing et al. (2009) as 78, 3.6 and 79 $kt\ yr^{-1}$, respectively. The same nutrient budgets for the whole Mediterranean are tabulated as 1077, 49.4 and 1028 $kt\ yr^{-1}$, respectively. As an anchor point, rivers of the Black Sea have a nitrogen budget of 1116 $kt\ yr^{-1}$, phosphorus budget of 55.1 $kt\ yr^{-1}$ and silica budget of 861 $kt\ yr^{-1}$.

The Mediterranean is known to be an oligotrophic sea due to low amount of nutrients supplied through straits, rivers and atmospheric fluxes. Moreover, vertical hydrodynamical mechanisms are insufficient to transport nutrients in intermediate and bottom layers to the surface of the sea. Primary production is generally low and is given as 80 $g\ C\ m^{-3}\ yr^{-1}$ for the Western Mediterranean whereas between 16 - 18 $g\ C\ m^{-3}\ yr^{-1}$ for the Eastern Mediterranean by *Yılmaz and Tuğrul (1998)* and citations therein. *Krom et al. (2010)* links low productivity with unusual anti-estuarine circulation in which the LIW carries dissolved nutrients out of the basin. *Yılmaz and Tuğrul (1998)* also emphasized the dominance of vertical mixing in winters

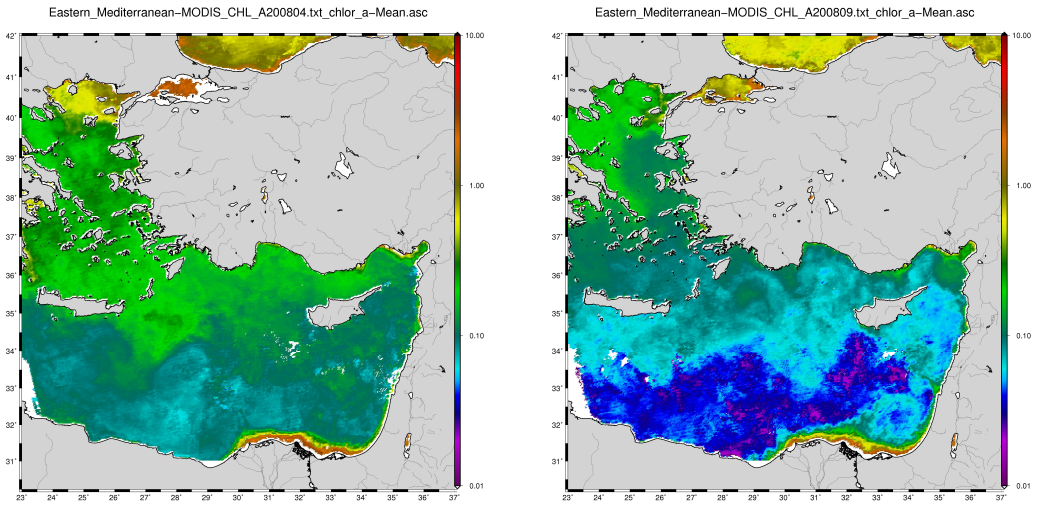

FIGURE 1.6: *MODIS-Aqua April2008 and September2008 surface chlorophyll distributions in the Eastern Mediterranean*

on primary producion, especially in cyclonic regions where nutrients situated in deeper layers can be transported into surface and sub-surface layers. In particular, their study shows that in the periphery of the cyclonic Rhodes region, the Levantine Deep Water (LDW) and nutricline move up to the sub-surface euphotic zone during severe winters. On the other hand, in seasons when stratification occurs, they estimated the depth integrated values for the euphotic zone as 0.2 μM for nitrate and less than 0.02 μM for phosphate. After calculating high N/P ratios for the LDW, they concluded phosphorus limitation of primary production of the Levantine Sea. One theory on P-limitation is suggested by *Krom et al. (1991)*. Their hypothesis is based on removal of phophate from deep waters rather than nitrate addition by Saharan dust. Another hypothesis is proposed by *Bethoux et al. (1992)* in which they relate phosphate limitation to extreme N-fixation in the system by sea grasses or N-fixing phytoplanktons. Later in 2004, *Krom et al.* responded to this hyphothesis by highlighting the undefined N-fixing capability of Synnechoccus presented as the only potential N-fixing organism in the Eastern Mediterranean in significant numbers.

Krom et al. (2010) indicate October to March as the major phytoplankton bloom period. They further claim that a temporary attenuation of mixing due to warmer and clear weather during winters is the main factor that allows blooms. Dominant phytoplankton communities in the region are quoted as nanoplanktons and picoplanktons. 80 - 100% of chlorophyll-a biomass are claimed to consist of these two species. Furthermore, *Petihakis et al. (2009)* relates this dominancy of picoplanktons to their advantage over large phytoplanktons, such as

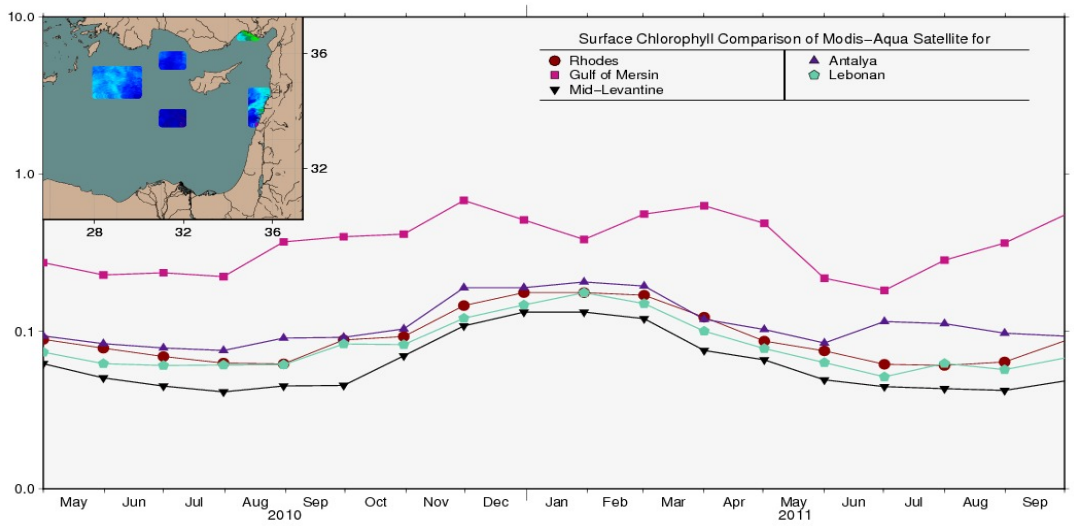

FIGURE 1.7: *Monthly averages of MODIS-Aqua surface chlorophyll in the five different regions of the Levantine Sea*

diatoms and flagellates, due to their small size which allows them to grow and compete over limiting nutrients easier. Their estimate on picoplankton biomass compared to total biomass is between 57% to 82%.

Around the Rhodes Gyre, *Ediger et al. (2005)* determined the depth of euphotic zone as 60 - 80 m where chlorophyll-a values range between 0.02 - 1.0 $\mu g\ l^{-1}$. Corresponding values are given as 0.19 - 0.45 $\mu g\ l^{-1}$ for anti-cyclonic Cilician region. During early spring blooms, an increase in chlorophyll-a values upto 1.0 - 3.1 $\mu g\ l^{-1}$ is observed by them (also see satellite derived Fig. 1.6 and 1.7 for distribution of surface chlorophyll regionally). They declared a deep chlorophyll maximum (DCM) between 40 - 60 m, slightly upper part of euphotic zone throughout year except strong mixing period before spring. *Manca et al. (2004)* gathered and analyzed available in situ data to understand the annual vertical behaviour of different regions of the Mediterranean. They assert a photic layer of 120 m depth. Fig. 1.8 implies a DCM around 100 m depth in the indicated area on map below the figure.

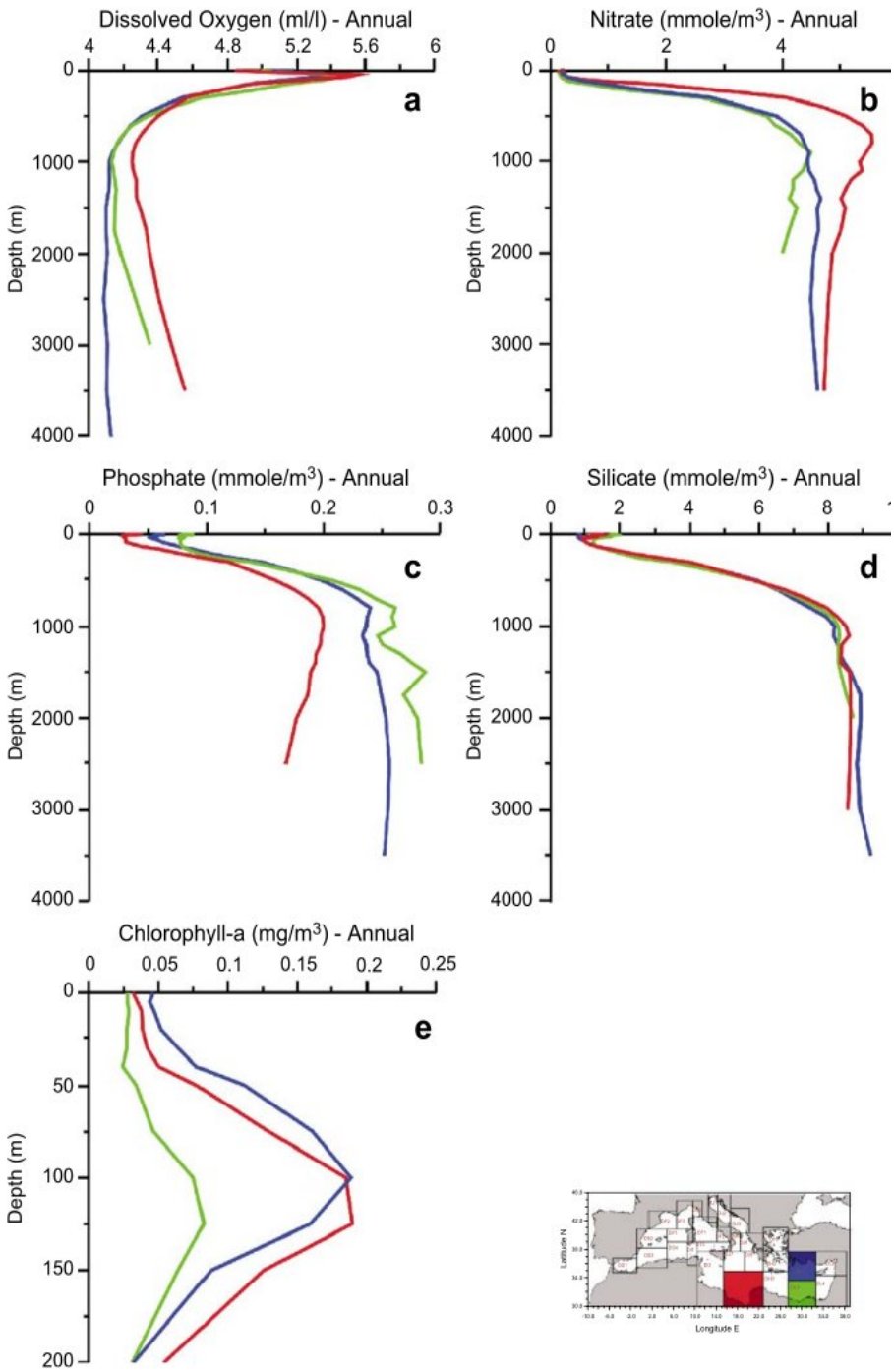

FIGURE 1.8: *Vertical profiles of (a) Dissolved Oxygen (b) Nitrate (c) Phosphate (d) Silicate (e) Chlorophyll-a annually in three different regions of Eastern Mediterranean (retrieved from Manca et al., 2004)*

CHAPTER 2

REGIONAL OCEAN MODELING SYSTEM

The Regional Ocean Modelling System (ROMS) is used in this study for the Levantine Basin of the Eastern Mediterranean. ROMS, an ocean model widely used by the oceanographic community, is based on three dimensional, free surface, primitive equations. It uses stretched, terrain-following vertical coordinates and orthogonal curvilinear horizontal coordinates on an Arakawa 'C' grid. Reynolds averaged Navier-Stokes equations are solved by using the hydrostatic and Boussinesq assumptions (*Haidvogel et al., 2000*). Various sub-models for biogeochemical (*Power et al., 2006; Fennel et al., 2006*), bio-optical (*Bissett et al., 1999*), sedimentary (*Warner et al., 2008*) and sea-ice (*Budgell, 2005*) components are optionally included. ROMS uses very accurate and efficient numerical algorithms. Numerical discretization of primitive equations in vertical over versatile topography is achieved by using stretched terrain following coordinates which allows to increase resolution in areas of interest. In the horizontal, the model equations are evaluated using boundary-fitted, orthogonal curvilinear coordinates on a staggered Arakawa C-grid. It offers no-slip or free-slip wall options for closed boundaries. There exists several choices for open boundary conditions. Time-stepping in ROMS is split into coupled barotropic and baroclinic components, with a finite number of barotropic time-steps carried out in each baroclinic time step, leading to savings from computational expenses. Several well-known turbulence closure schemes are also proposed for vertical mixing. To activate a wide variety of physical and numerical model options, ROMS uses C-preprocessing, enabled with the F90/F95 fortran code of the model. The code uses a coarse grained parallelization paradigm which allows partitioning of the 3D-grid into tiles. As a result, either serial or parallel computation using OpenMP and MPI protocols can be preferred. Network Common Data Form (NetCDF) is used for all input/output of data.

2.1 Model Description

2.1.1 Equations of Motion

The hydrostatic primitive equations resulting from Reynolds averaging of the Navier-Stokes equations are

$$\frac{\partial u}{\partial t} + \vec{v}.\nabla u - fv = -\frac{\partial \phi}{\partial x} - \frac{\partial}{\partial z}\Big(\overline{u'\omega'} - \nu\frac{\partial u}{\partial z}\Big) + \mathsf{F}_u + \mathsf{D}_u \tag{2.1}$$

$$\frac{\partial v}{\partial t} + \vec{v}.\nabla v - fu = -\frac{\partial \phi}{\partial y} - \frac{\partial}{\partial z}\Big(\overline{v'\omega'} - \nu\frac{\partial v}{\partial z}\Big) + \mathsf{F}_v + \mathsf{D}_v \tag{2.2}$$

$$\frac{\partial \phi}{\partial z} = \frac{-\rho g}{\rho_0} \tag{2.3}$$

with the continuity equation:

$$\frac{\partial u}{\partial x} + \frac{\partial v}{\partial y} + \frac{\partial \omega}{\partial z} = 0 \tag{2.4}$$

and scalar transport given by:

$$\frac{\partial C}{\partial t} + \vec{v}.\nabla C = -\frac{\partial}{\partial z}\Big(\overline{C'\omega'} - \kappa\frac{\partial C}{\partial z}\Big) + \mathsf{F}_C + \mathsf{D}_C. \tag{2.5}$$

An equation of state is also required:

$$\rho = \rho\,(T, S, P)\,. \tag{2.6}$$

The variables are shown in Table 2.1. An overbar represents a time average and a prime represents a fluctuation about the mean. These equations are closed by parameterizing the Reynolds stress and turbulent tracer fluxes as:

$$\overline{u'\omega'} = -K_M\frac{\partial u}{\partial z}; \qquad \overline{v'\omega'} = -K_M\frac{\partial v}{\partial z}; \qquad \overline{C'\omega'} = -K_C\frac{\partial C}{\partial z} \tag{2.7}$$

Equations (2.1) and (2.2) state the momentum equations in the x- and y-directions, respectively. Because of the Boussinesq assumption, density variations are neglected in the momentum equations (2.1) and (2.2) but they have contribution to the buoyancy force in the vertical momentum equation (2.3). Equation (2.4) is the continuity equation for an incompressible fluid. The time evolution of all scalar concentration fields, including those for $T(x, y, z, t)$ and $S\,(x, y, z, t)$, are governed by the advective-diffusive equation (2.5). Hydrostatic approximation ensures that the vertical pressure gradient balances the buoyancy force. Finally, Equation (2.6) is the equation of state. The terms F and D represent the effects of forcing and horizontal dissipation, respectively (*Hedström, 2009*).

Variable	*Description*
$C(x, y, z, t)$	scalar quantity, i.e. temperature, salinity, nutrient concentration
D_u,D_v,D_C	optional horizontal diffusive terms
F_u,F_v,F_C	forcing/source terms
$f(x, y)$	Coriolis parameter
g	acceleration of gravity
$h(x, y)$	depth of sea floor below mean sea level
$H_z(x, y, z)$	vertical grid spacing
ν, κ	molecular viscosity and diffusivity
K_M, K_C	vertical eddy viscosity and diffusivity
P	total pressure P $\approx$ -$\rho_0$gz
$\phi_(x, y, z, t)$	dynamic pressure ϕ = (P/ρ_0)
ρ_0+$\rho(x, y, z, t)$	total *in situ* density
$S(x, y, z, t)$	salinity
t	time
$T(x, y, z, t)$	potential temperature
u, v, ω	the (x, y, z) components of vector velocity $\vec{v}$
x,y	horizontal coordinates
z	vertical coordinates
ζ(x,y,t)	surface elevation

TABLE 2.1: *The variables used in the description of the ocean model*

2.1.2 Boundary Conditions

2.1.2.1 Vertical boundary conditions

The vertical boundary conditions can be prescribed as follows:

$$
\begin{aligned}
\text{top}(z = \zeta\,(x, y, z)) \qquad & K_m \tfrac{\partial u}{\partial z} = \tau_s^x(x, y, t) \\
& K_m \tfrac{\partial v}{\partial z} = \tau_s^y(x, y, t) \\
& K_C \tfrac{\partial C}{\partial z} = \tfrac{Q_C}{\rho_0 c_P} \\
& \omega = \tfrac{\partial \zeta}{\partial t} \\
\text{and bottom}(z = -h(x, y)) \qquad & K_m \tfrac{\partial u}{\partial z} = \tau_b^x(x, y, t) \\
& K_m \tfrac{\partial v}{\partial z} = \tau_b^y(x, y, t) \\
& K_C \tfrac{\partial C}{\partial z} = 0 \\
& -\omega + \vec{v} \cdot \nabla h = 0
\end{aligned}
$$

The variables of boundary condition at the surface are defined in Table 2.2. For temperature, since surface flux is a strong function of the surface temperature, Q_T is computed using the surface temperature and the atmospheric fields in an atmospheric bulk flux parametrization. The same bulk flux routine is also used to compute the wind stress from the winds.

Variable	*Description*
Q_C	surface concentration flux
τ_s^x, τ_s^y	surface wind stress
τ_b^x, τ_b^y	bottom stress

TABLE 2.2: *The variables used in the vertical boundary conditions for the ocean model*

At the bottom, $z = -h(x, y)$, bottom stress can be chosen among linear, quadratic, or logaritmic terms to prescribe the horizontal velocity. Although it is usually set to zero, the vertical flux may also be prescribed (*Hedström, 2009*).

2.1.2.2 Horizontal boundary conditions

There are several application areas such as a closed basin, a basin with open boundaries or a periodic channel that ROMS can be adapted. For this purpose, the model offers a large variety of boundary conditions for u, υ, T,S, and ζ.

The Simplest of these boundary conditions is gradient condition which sets zero at the edge and closest interior value outside.

The second and default boundary condition is wall condition, which assumes zero gradient for tracers, the surface elevation and the normal velocity for closed boundaries. Although model domain is rectangular, it is possible to mask out land areas on the boundary and in the interior. No-slip or free-slip wall options for tangential velocities can be applied as boundary conditions on these masked regions. If biharmonic friction is chosen, a higher order boundary condition must also be provided. The higher order boundary conditions used for u are $\frac{\partial}{\partial x}\left(u\frac{\partial^2 u}{\partial x^2}\right) = 0$ on the eastern and western boundaries, and $\frac{\partial}{\partial y}\left(v\frac{\partial^2 v}{\partial y^2}\right) = 0$ on the northern and southern boundaries. In a similar way, the boundary conditions for u, v and C can be stated. Preserving the property of no gain or loss of volume-integrated momentum or scalar concentration is the reason why these boundary conditions were chosen (*Hedström, 2009*).

Another condition, namely, clamped condition sets the boundary value to an exterior value such that $\Phi = \Phi^{ext}$.

For 2-D momentum equations, *Flather (1976)* and *Chapman (1985)* conditions are choices for a more realistic simulation. For normal and tangential velocities, these options can be used, respectively. To figure out the barotropic normal velocity, *Flather (1976)* uses external

data and solves the equation:

$$\bar{u} = \bar{u}^{ext} - \sqrt{gD}(\zeta - \zeta^{ext}) \tag{2.8}$$

In coordinance with Flather condition, surface elevation can be calculated according to *Chapman (1985)* by

$$\frac{\partial \zeta}{\partial t} = \pm \sqrt{\frac{g}{h}} \frac{\partial \zeta}{\partial \xi} \tag{2.9}$$

where h is local water depth.

Radiation boundary condition, proposed by *Orlanski (1976)*, is a solution for open boundaries in which inflow and outflow occurs together. The model also promises a mixed radiation-nudging condition *(Marchesiello, 2001)*. Radiation condition controls outflow and an exterior value is nudged for inflow. The model solves following equation for radiation condition of *Marchesiello (2001)*:

$$\frac{\partial \phi}{\partial t} + c_x \frac{\partial \phi}{\partial x} + c_y \frac{\partial \phi}{\partial y} = 0 \tag{2.10}$$

where ϕ is model variable, (x, y) are the normal and tangential directions to the boundary in the local cartesian coordinates and (c_x,c_y) are phase speeds. Here (c_x,c_y) are derived from ϕ field surrounding the boundary points as follows:

$$c_x = -\frac{\partial \phi}{\partial t} \frac{\partial \phi / \partial x}{(\partial \phi^2 / \partial x^2) + (\partial \phi^2 / \partial y^2)} \tag{2.11}$$

and

$$c_y = -\frac{\partial \phi}{\partial t} \frac{\partial \phi / \partial y}{(\partial \phi^2 / \partial x^2) + (\partial \phi^2 / \partial y^2)} \tag{2.12}$$

2.1.3 Coordinate Systems

2.1.3.1 Terrain-following coordinate system

In a modelling study of the geophysical systems, such as in meteorology and oceanography, to introduce a coordinate system that follows the topography is usually very useful. In practice, ROMS uses a stretched vertical coordinate system, σ-coordinate system, that needs following transformations:

$$\hat{x} = x$$

$$\hat{y} = y$$

$$\sigma = \sigma(x, y, z)$$

$$z = z(x, y, \sigma)$$

and

$$\hat{t} = t$$

In the stretched system, ($\sigma = 0$) and ($\sigma = -1$) represents top and bottom boundaries, respectively. That is to say, the vertical coordinate σ changes in the range $-1 < \sigma < 0$. For this transformation, following chain rules are applied:

$$\left(\frac{\partial}{\partial x}\right)_z = \left(\frac{\partial}{\partial x}\right)_\sigma - \left(\frac{1}{H_z}\right)\left(\frac{\partial z}{\partial x}\right)_\sigma \frac{\partial}{\partial \sigma}$$

$$\left(\frac{\partial}{\partial y}\right)_z = \left(\frac{\partial}{\partial y}\right)_\sigma - \left(\frac{1}{H_z}\right)\left(\frac{\partial z}{\partial y}\right)_\sigma \frac{\partial}{\partial \sigma}$$

$$\frac{\partial}{\partial z} = \left(\frac{\partial s}{\partial z}\right)\frac{\partial}{\partial \sigma} = \left(\frac{1}{H_z}\right)\frac{\partial}{\partial \sigma}$$

where

$$H_z = \frac{\partial z}{\partial \sigma}$$

Modifications which are done in dynamical equations and vertical boundary conditions as a result of this transformation are well-documented in *Hedström (2009)*.

2.1.3.2 Horizontal curvilinear coordinates

As in the case of vertical coordinates, it is mostly advantageous to fit a coordinate system that follows lateral boundaries. For this aim, assuming the new coordinates as $\xi(x, y)$ and $\eta(x, y)$, horizontal arc length and the differential distance are related by:

$$(ds)_\xi = \left(\frac{1}{m}\right)d\xi$$

$$(ds)_\eta = \left(\frac{1}{n}\right)d\eta$$

where $m(\xi, \eta)$ and $n(\xi, \eta)$ are relating scale factors. Horizontal boundary conditions do not change as a consequence of this transformation. Hence, after coordinate transformations Eqn. 2.1-2.6 can be rewriten as:

$$\frac{\partial}{\partial t}\left(\frac{H_z u}{mn}\right) + \frac{\partial}{\partial \xi}\left(\frac{H_z u^2}{n}\right) + \frac{\partial}{\partial \eta}\left(\frac{H_z u v}{m}\right) + \frac{\partial}{\partial \sigma}\left(\frac{H_z u \Omega}{mn}\right) - \left\{\left(\frac{f}{mn}\right) + v\frac{\partial}{\partial \xi}\left(\frac{1}{n}\right) - u\frac{\partial}{\partial \eta}\left(\frac{1}{m}\right)\right\}H_z v =$$
$$-\left(\frac{H_z}{n}\right)\left(\frac{\partial \phi}{\partial \xi} + \frac{g\rho}{\rho_0}\frac{\partial z}{\partial \xi} + g\frac{\partial \zeta}{\partial \xi}\right) + \frac{1}{mn}\frac{\partial}{\partial \sigma}\left[\frac{K_m}{H_z}\frac{\partial u}{\partial \sigma}\right] + \frac{H_z}{mn}(\mathsf{F}_u + \mathsf{D}_u) \quad (2.13)$$

$$\frac{\partial}{\partial t}\left(\frac{H_z v}{mn}\right)+\frac{\partial}{\partial \xi}\left(\frac{H_z u v}{n}\right)+\frac{\partial}{\partial \eta}\left(\frac{H_z v^2}{m}\right)+\frac{\partial}{\partial \sigma}\left(\frac{H_z v \Omega}{mn}\right)+\left\{\left(\frac{f}{mn}\right)+v\frac{\partial}{\partial \xi}\left(\frac{1}{n}\right)-u\frac{\partial}{\partial \eta}\left(\frac{1}{m}\right)\right\}H_z u = -\left(\frac{H_z}{m}\right)\left(\frac{\partial \phi}{\partial \eta}+\frac{g\rho}{\rho_0}\frac{\partial z}{\partial \eta}+g\frac{\partial \zeta}{\partial \eta}\right)+\frac{1}{mn}\frac{\partial}{\partial \sigma}\left[\frac{K_m}{H_z}\frac{\partial v}{\partial \sigma}\right]+\frac{H_z}{mn}(\mathsf{F}_v+\mathsf{D}_v) \quad (2.14)$$

$$\frac{\partial \phi}{\partial \sigma}=-\left(\frac{gH_z\rho}{\rho_0}\right) \quad (2.15)$$

$$\frac{\partial}{\partial t}\left(\frac{H_z}{mn}\right)+\frac{\partial}{\partial \xi}\left(\frac{H_z u}{n}\right)+\frac{\partial}{\partial \eta}\left(\frac{H_z v}{m}\right)+\frac{\partial}{\partial \sigma}\left(\frac{H_z \Omega}{mn}\right)=0 \quad (2.16)$$

$$\frac{\partial}{\partial t}\left(\frac{H_z C}{mn}\right)+\frac{\partial}{\partial \xi}\left(\frac{H_z u C}{n}\right)+\frac{\partial}{\partial \eta}\left(\frac{H_z v C}{m}\right)+\frac{\partial}{\partial \sigma}\left(\frac{H_z \Omega C}{mn}\right)=\frac{1}{mn}\frac{\partial}{\partial s}\left[\frac{K_C}{H_z}\frac{\partial C}{\partial \sigma}\right]+\frac{H_z}{mn}(\mathsf{F}_C+\mathsf{D}_C) \quad (2.17)$$

$$\rho=\rho(T,S,P) \quad (2.18)$$

2.2 Numerical Solution Technique

2.2.1 Vertical and horizontal discretization

2.2.1.1 Vertical grid

A second-order finite-difference approximation and a staggered vertical grid, shown in Fig. 2.1 (a), are used for the vertical discretization. The model is shown to be well-behaved with a staggered vertical grid.

2.2.1.2 Horizontal grid

In the horizontal discretization (ξ, η), the Arakawa C grid, a well known traditional, centered, second-order finite-difference approximation is used. For problems with horizontal resolution that is fine compared to the first baroclinic Rossby radius of deformation, Arakawa C grid is well suited. The horizontal arrangement of variables is as shown in Fig. 2.1 (b) (*Arakawa and Lamb, 1977*).

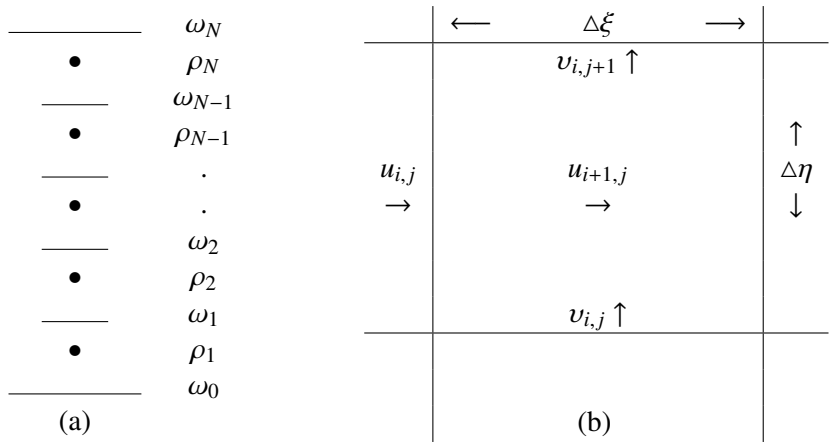

FIGURE 2.1: *Placement of variables on (a) staggered vertical grid (b) Arakawa C-grid*

2.2.2 Timestepping

Timestepping algorithms with forward-backward (FB) feedback are used between the pairs of variables responsible for gravity wave propagation (surface and internal). Algorithms are combined to increase the accuracy (*Shchepetkin, 2005*). There are various timestepping schemes that can be implemented into different models (Rutgers University ROMS, UCLA ROMS, ROMS AGRIF) of ROMS family. Also different timestepping schemes can be chosen for different terms in the equations. Euler, Leapfrog (LF), second order Runge-Kutta (RK2), second order Adams-Bashforth (AB2) are among time stepping schemes to be combined.

The model first solves the momentum equations (2.13) and (2.14) to find new values for u and v. Also new values for $\langle\bar{u}\rangle$ and $\langle\bar{v}\rangle$ are computed from depth integrated equations. At this stage, Adams-Bashforth (AB3) timestepping is prefered. Then, a predictor-corrector leapfrog-trapezoidal timestepping algorithm is used to solve equation 2.17 for tracers (*Hedström, 2009*).

2.2.3 Advection schemes

Although model provides a centered second-order scheme, the default algorithm for advection is centered fourth-order based on MPDATA (Multidimensional Positive Definite Advection Transport Algorithm). Moreover, fourth-order Akima scheme can also be used. Another advection scheme, namely UTOPIA (Uniformly Third-Order Polynomial Interpolation Algorithm), that belongs to third order upwind advection schemes is also an option. UTOPIA can

be used on variables that can have both negative and positive values such as velocity, although MPDATA can only be used on positive scalars.

Non-linear equation of state $\rho = \rho(T, S, z)$ is chosen to be the UNESCO equation of state as derived by *Jackett and MyDougall (1995)*. *In situ* density is derived from potential temperature, salinity and pressure. Besides ROMS also offers a linear equation of state $\rho = \rho(T)$, although it is claimed not to be appropriate dynamically (*IHedström, 2009*).

2.2.4 Vertical and horizontal mixing

Vertical mixing in ROMS is governed by turbulence closure schemes which may have important influences on both mixing and circulation (*Warner, 2005*). Alternatives among these schemes are Mellor-Yamada Level 2.5 scheme modified by *Galperin (1988)*, K profile parametrization (KPP) or LMD scheme introduced by *Large, McWilliams and Doney (1994)* and Generic Length Scale (GLS) turbulence closure as defined in *Umlauf and Burchard (2003)* and *Warner (2005)*. By determining vertical viscous and diffusive coefficients, these methods play important role in parameterizing primitive equations.

For horizontal mixing, harmonic and biharmonic schemes and the Smagorinsky scheme are offered.

2.3 Ecosystem Modules

ROMS can be coupled with a range of ecosystem submodels. Ecological simplicity of these sub-models can be ordered as; three NPZD-type models, a Fasham-type (Fennel) model, a two-phytoplankton-class (NEMURO) model, and a multiple-phytoplankton-class (ECOSIM) model.

The *NPZD-type* models has four state variables representing a limiting nutrient (generally inorganic nitrogen), phytoplankton, zooplankton and detritus, all of which are measured in units of the limiting nutrient (*Powell et al., 2005*). There is also an iron limiting NPZD submodel (*Feichter et al., 2009*).

The *Fennel* model is an improved Fasham's model (*Fasham et al., 1990*). Nitrate and ammonium are treated as two different state variables in the ROMS implementation of Fennel model, chlorophyll is included as a prognostic variable in addition to phytoplankton biomass;

moreover, small and large detritus are also separated (*Fennel et al., 2006*).

The *NEMURO* model differs from the Fennel model by the presence of two phytoplankton groups, larger diatomaceous phytoplankton and small phytoplankton. NEMURO also includes silicic acid as an additional nutrient. A further difference lies in the explicit characterization of the internal nitrogen, carbon and, in the case of diatoms and large detritus, silica concentrations within the plankton and detrital pools allowing time-evolving variability in the elemental composition of different functional groups (*Lima and Doney, 2004*).

The most complex of the ecosystem models is the multiple-phytoplankton-class *ECOSIM* model. It explicity represents four groups of phytoplankton including their internal carbon and nitrogen concentrations and dissolved organic matter; on the other hand, zooplankton is not represented explicitly (*Bissett et al., 1999*).

All of these models focus on the lower trophic levels of the ecosystem which are assumed to be described reasonably well by the Eulerian concentrations (*Haidvogel et al., 2008*).

2.3.1 Fennel ecosystem submodel

Fennel model is a representation of the pelagic nitrogen cycle and includes seven state variables: phytoplankton (*Phy*), zooplankton (*Zoo*), nitrate (*NO3*), ammonium (*NH4*), small and large detritus (*SDet* and *LDet*), and phytoplankton chlorophyll (*Chl*). The equations stated in this section for the ecological model are all described in *Fennel (2006)*.

In Fennel model, the rate of change of phytoplankton in time due to biological sources and sinks is given by

$$\frac{\partial Phy}{\partial t} = \mu Phy - gZoo - m_P Phy - \tau(S\,Det + Phy)Phy - w_P \frac{\partial Phy}{\partial z} \tag{2.19}$$

The growth rate of phytoplankton, μ, depends on the temperature T through the maximum growth rate $\mu_{max} = \mu_{max}\,(\mathrm{T}) = \mu_0 \cdot 1.066^T$ (*Eppley, 1972*), on the photosynthetically available radiation I, and on the nutrient concentrations *NO3* and *NH4*,

$$\mu = \mu_m ax \cdot f(I) \cdot (L_{NO3} + L_{NH4}), \tag{2.20}$$

where

$$L_{NO3} = \frac{NO3}{k_{NO3} + NO3} \cdot \frac{1}{1 + NH4/k_{NH4}} \tag{2.21}$$

$$L_{NH4} = \frac{NH4}{k_{NH4} + NH4} \tag{2.22}$$

I is exponentially decreasing with water depth z according to

$$I = I(z) = I_0 \cdot par \cdot exp\left[-z\left(K_w + K_{chl}\int_z^0 Ch(\zeta)\,d\zeta\right)\right] \tag{2.23}$$

Here I_0 is the incoming light just below the sea surface, and *par* is the fraction of light that is available for photosynthesis. K_w and K_{chl} are the light attenuation coefficients for water and chlorophyll, resperctively. The function f(I) represents photosythesis-light (P-I) relationship (*Evans and Parslow, 1985*)

$$f(I) = \frac{\alpha I}{\sqrt{\mu_{max}^2 + \alpha^2 I^2}} \tag{2.24}$$

where α is the initial slope. Nutrient limitation is represented by the sum of Michealis-Menten functions for nitrate and ammonium, L_{NO3} and L_{NH4}, and nitrate uptake is assumed to be inhibited in the presence of ammonium through the factor $1/(1+NH4/k_{NH4})$ following *Parker (1993)*. Here k_{NO3} and k_{NH4} are the half-saturation concentrations for uptake of nitrate and ammonium, respectively.

Zooplankton's grazing rate is characterized by a Holling-type s-shaped curve as

$$g = g_{max}\frac{Phy^2}{k_P + Phy^2} \tag{2.25}$$

where g_{max} is maximum grazing rate and k_P as half-saturation concentration for phytoplankton ingestion.

The dynamics of chlorophyll is a result of phytoplankton equation by convertion into chlorophyll units. This conversion is achieved by multiplying with the ratio of chlorophyll to phytoplankton biomass and assuming chlorophyll is synthesized only in a fraction of phytoplankton growth. This fraction is

$$\rho_{chl} = \frac{\Theta_{max}\mu Phy}{\alpha I Chl} \tag{2.26}$$

where Θ_{max} is the maximum ratio of chlorophyll to phytoplankton biomass. As a result of this conversion, the time rate of change of chlorophyll can be stated as

$$\frac{\partial Chl}{\partial t} = \rho_{Chl}\mu Chl - gZoo\frac{Chl}{Phy} - m_p Chl - \tau(S\,Det + Phy)Chl \tag{2.27}$$

In a similar manner, zooplankton and small and large detritus equations follow as

$$\frac{\partial Zoo}{\partial t} = g\beta Zoo - l_{BM}Zoo - l_E\frac{Phy^2}{k_P + Phy^2}\beta Zoo - m_Z Zoo^2 \tag{2.28}$$

$$\frac{\partial S\,Det}{\partial t} = g(1-\beta)Zoo + m_Z Zoo^2 + m_P Phy - \tau(S\,Det + Phy)S\,Det - r_{SD}S\,Det - w_S\frac{\partial S\,Det}{\partial z} \tag{2.29}$$

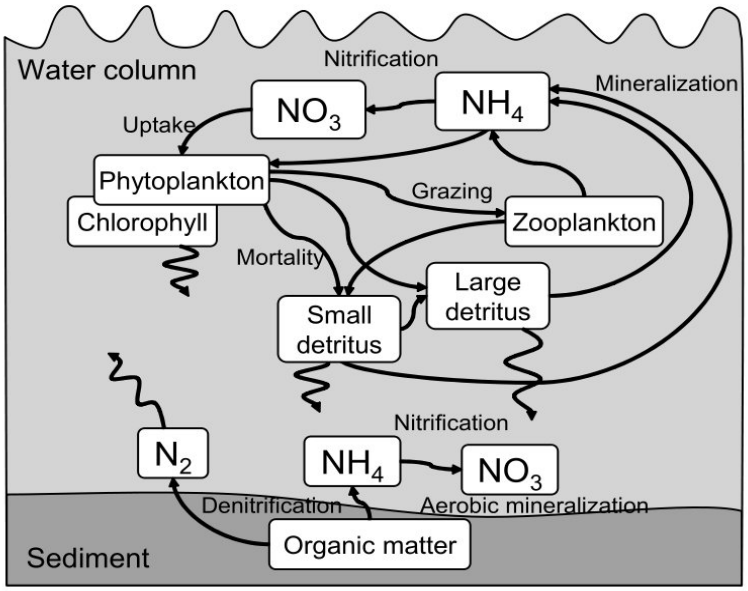

FIGURE 2.2: *Fennel model scheme (Adapted from Fennel et al., 2006)*

$$\frac{\partial LDet}{\partial t} = \tau(S\,Det + Phy)^2 - r_{LD}LDet - \ w_L\frac{\partial LDet}{\partial z} \tag{2.30}$$

Finally, below is the model equations for time rate of change of nitrate and ammonium

$$\frac{\partial NO3}{\partial t} = -\mu_{max}f(I)L_{NO3}Phy + nNH4 \tag{2.31}$$

$$\frac{\partial NH4}{\partial t} = -\mu_{max}f(I)L_{NH4}Phy - nNH4 + l_{BM}Zoo\ l_E\frac{Phy^2}{k_P + Phy^2}\beta\cdot Zoo + r_{SD}S\,Det + r_{LD}LDet \tag{2.32}$$

Nitrification rate $n = n_{max}\left(1 - max\left[0, \frac{I-I_0}{k_I+I-I_0}\right]\right)$ is assumed to drop off to zero at high light intensities with k_I as the light intensity at which inhibition is half-saturated and an inhibition threshold of I_0.

Sketch of Fennel module in terms of relations between biological variables is displayed in Figure 2.2. Parameters used in formulations, symbols representing them, their units and values used in the model runs are listed in Table 3.1 .

CHAPTER 3

NORTHERN LEVANTINE BASIN MODEL (NLEV) SETUP AND RUN DATA

In this chapter, the ROMS model configuration for the Northern Levantine region and the data used for simulations will be introduced. The model requires initial condition data representing model initial fields and model boundary conditions consisting of data specified at lateral boundaries and atmospheric forcing applied at the surface, respectively, are gathered from different sources and cited in the following sections.

Computational tools utilized in this study are FORTRAN90 programming language and the FERRET graphical data access tool of NOAA. For visualizations, mainly Generic Mapping Tools (GMT) is used. However, some figures are generated with FERRET. SEAWIFS and MODIS satellite data are processed by SEADAS software provided by NASA. Finally, this document is compiled by LaTeX.

Two sets of runs were performed with the given NLEV model geometric configuration, described in the following. The first case is part of coupled hydrodynamics - ecosystem simulations performed under the project SESAME (www.sesame-ip.eu), to study the combined specific response of the region with respect to two 5-year slices of present and future Mediterranean climate conditions. For this part of the study, the model for the semi-enclosed NLEV domain were nested in Mediterranean scale coupled ecosystem simulations and ocean surface data for the corresponding periods were generated by a global atmospheric model. The same model configuration, without any changes in geometry, is also used for the Northern Levantine Basin forecasts, displayed at the Institute of Marine Sciences physical oceanography web site (http://ocean.ims.metu.edu.tr). For the second part of the present study, we use this forecast model version with only the hydrodynamic part, to make a sensitivity study of the various parameter and option settings of the model.

3.1 Bathymetry

For the bathymetry of the study area, the gridded data of the General Bathymetric Chart of the Oceans, GEBCO_08 database, with a global 30 arc-second grid resolution are used. A 3D-visualization and a contour plot of the bathymetry for the study area are provided in Fig. 1.1.

3.2 1996-2000 and 2030-2034 Coupled Simulations

As it has been stated previously, two 5-year sliced coupled hydrodynamics-ecosystem simulations are backbones of this study. A hindcast for years 1996-2000 is performed to model and validate the Northern Levantine basin dynamics. Then the model is run using the same model configuration, a climate change scenario based on different atmospheric and river fluxes is simulated for 2030-2034. Comparison of these two runs will be presented in Section 4.6, however, in this section the details of model configuration and datasets will be provided.

3.2.1 Model Setup

The model is set up with a horizontal grid resolution of 1.35 *km* x 1.35 *km*. For the rectangular model domain, the north-south distance is approximately 260 *km* whereas the east-west distance is about 740 *km*. Therefore, the model has total grid point dimensions of 540 x 150. Horizontal cross-sections at $i = 55$ and $j = 75$, emphasized in Fig. 3.1, are chosen to present vertical profiles displayed in the following chapter.

In the vertical, there are 30 σ-levels. The vertical terrain-following coordinates, with appropriate transformation and stretching functions are chosen after *Shchepetkin (2005)*. Surface and bottom stretching parameters are defined as θ_s=1.5 and θ_b=0.85, respectively, with a critical depth of h_s=100 *m*. The corresponding 30 σ levels in the range $-1 < \sigma < 0$ are devised as σ = (-0.983 , -0.95 , -0.917 , -0.883 , -0.85 , -0.817 , -0.783 , -0.75 , -0.717 , -0.683 , -0.65 , -0.617 , -0.583 , -0.55 -0.517 , -0.483 , -0.45 , -0.417 , -0.383 , -0.35 , -0.317 , -0.283 , -0.25 , -0.217 , -0.183 , -0.15 , -0.117 , -0.083, -0.05 , -0.017) and represented in Fig. 3.2.

The model was stably integrated with a baroclinic (internal) mode time step of $\Delta t_i = 150\ s$ and barotropic (external) mode time step of $\Delta t_e = 50\ s$.

No-slip wall boundary conditions are specified at the closed northern and eastern coastal

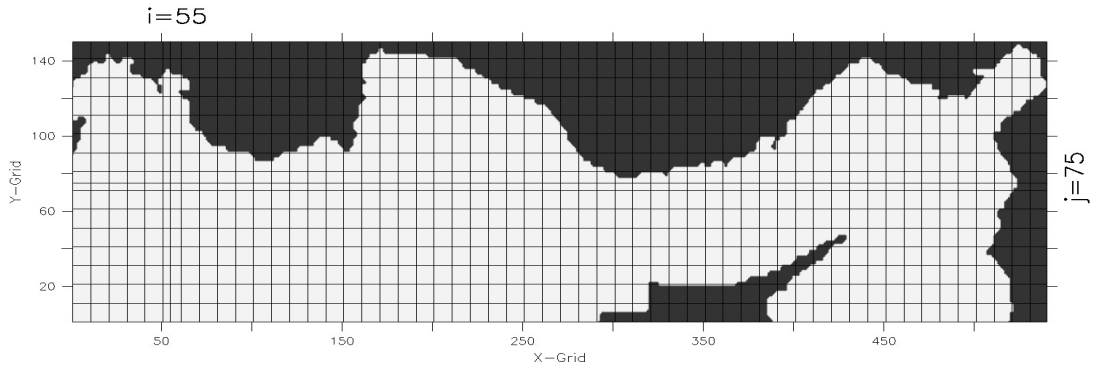

FIGURE 3.1: *Horizontal Curvilinear Grid*

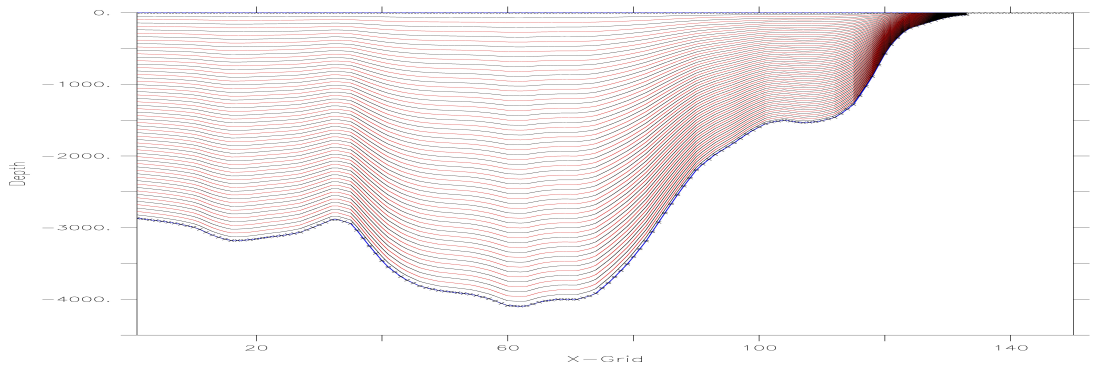

FIGURE 3.2: *Vertical Staggered Grid*

boundaries. Open boundary conditions are used for the west and south boundaries. Flather and Chapman open boundary conditions are applied for 2-D momentum and free-surface fields, respectively. Moreover, radiation conditions are implemented at the open boundaries. On 3-D fields, namely 3-D momentum, temperature, salinity and ecosystem (scalar) variables, boundary data are nudged with the nudging ratio set to 2, to ensure stronger control on the inflow, while leaving the outflow relatively more free to adjust. The Newtonian relaxation period for nudging of tracers and 3-D momentum at the boundaries is taken as 1 day. Finally, the sponge and volcons switches are activated in order to absorb any spurious oscillations at sponge layers and to ensure volume conservation at the open boundaries.

Bottom friction is chosen to be quadratic. For both tracers and momentum, Smagorinsky-like diffusivity and viscosity are implemented. The principal axes of momentum mixing is assumed to be aligned with geopotential surfaces and the conservative MPDATA 3-D advection scheme is activated for tracers. In the vertical, the LMD turbulence closure scheme is used with diffusivity and convective mixing is related to shear instability, surface and bottom boundary layer formulated according to KPP mixing. Values of the background vertical mixing coefficient for both turbulent kinetic energy and turbulent generic statistical field are taken

as $5x10^{-6}\ m^2 s^{-1}$.

The Fennel module of ecosystem dynamics (Section 2.3.1) is chosen for the ecosystem

Symbol	*Parameter*	*Value*	*Unit*
μ_0	phytoplankton growth rate at 0^oC	1.0	d^{-1}
g_{max}	maximum grazing rate	1.6	$(mmol\ N\ m^{-3})^{-1} d^{-1}$
m_P	phytoplankton mortality	0.045	d^{-1}
Θ_{max}	maximum chlorophyll to phytoplankton ratio	0.535	$mgChl\ mgC^{-1}$
α	initial slope of the P-I curve	0.017	$molC\ gChl^{-1}\ (Wm^{-2})^{-1}\ d^{-1}$
m_Z	zooplankton mortality	0.025	d^{-1}
k_P	half-saturation concentration of phytoplankton ingestion	1.0	$(mmol\ N\ m^{-3})^2$
k_{NO3}	half-saturation concentration for uptake of NO_3	2.0	$mmol\ N\ m^{-3}$
k_{NH4}	half-saturation concentration for uptake of NH_4	2.0	$mmol\ N\ m^{-3}$
τ	aggregation parameter	0.005	$(mmol\ N\ m^{-3})^{-1} d^{-1}$
β	assimilation efficiency	0.75	dimensionless
l_{BM}	excretion rate due to basal metabolism	0.1	d^{-1}
l_E	maximum rate of assimilation related excretion	0.1	d^{-1}
r_{SD}	remineralization rate of suspended detritus	0.03	d^{-1}
r_{LD}	remineralization rate of large detritus	0.1	d^{-1}
n_{max}	maximum nitrification rate	0.05	d^{-1}
k_I	light intensity at which the inhibition of nitrification is half-saturated	0.0095	$W\ m^{-2}$
I_0	threshold for light-inhibition of nitrification	0.1	$W\ m^{-2}$
w_{Phy}	sinking velocity of phytoplankton	0.1	$m\ d^{-1}$
w_{SDet}	sinking velocity of suspended detritus	0.1	$m\ d^{-1}$
w_{LDet}	sinking velocity of larger particles	0.1	$m\ d^{-1}$

TABLE 3.1: *Parameters used in the Fennel ecosystem model*

simulations. The units and values of the various parameters as required by equations 2.19 - 2.32, and representative of the model processes are listed in Table 3.1.

3.2.2 Initialization

The model was initialized on 1 January 1996 for physical and biological variables which, with the exception of sea surface height, were provided by Istituto Nazionale di Oceanografia e di Geofisica Sperimentale (OGS) OPA model. SSH is provided by Centro Euro-Mediterraneo per i Cambiamenti Climatici (CMCC) and extracted from IPSL model output with 871x253 horizontal grid size and 72 vertical levels and interpolated to model grid. Surface distributions of initial data for variables used can be seen from Fig. 3.3 to Fig. 3.6.

3.2.3 Boundary Fluxes

Boundary data is used to nudge flow and nutrient loads into the basin. Inflow-outflow balance is taken into consideration. Data for fluxes from western and southern boundaries is also provided by OGS-OPA model and sea level data is extracted from CMCC model.

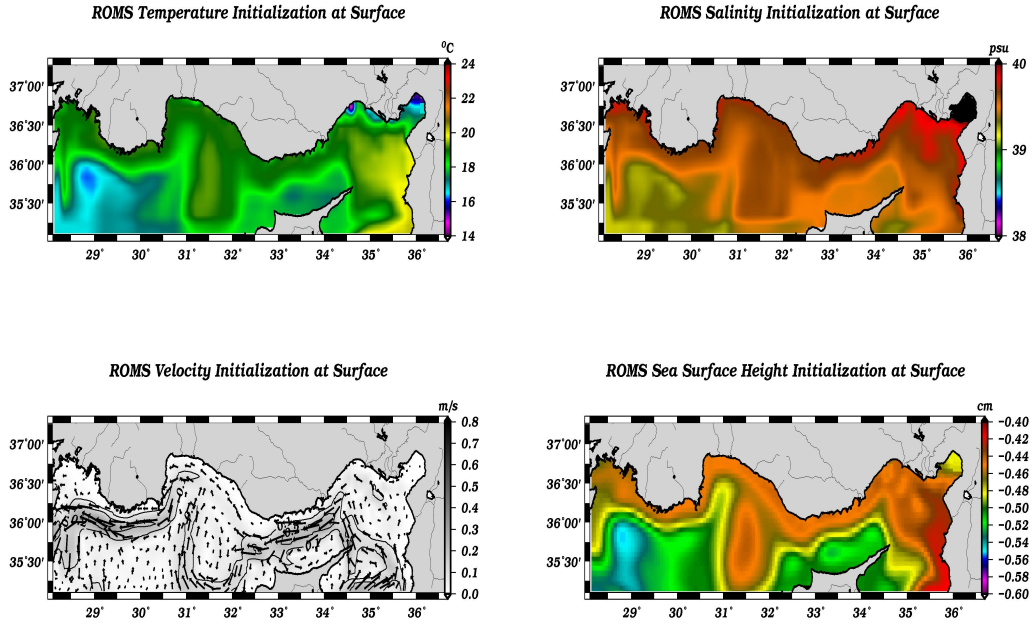

FIGURE 3.3: *Initial surface data for hydrodynamic variables temperature, salinity, velocity, sea surface height (from top-left to bottom-right, respectively)*

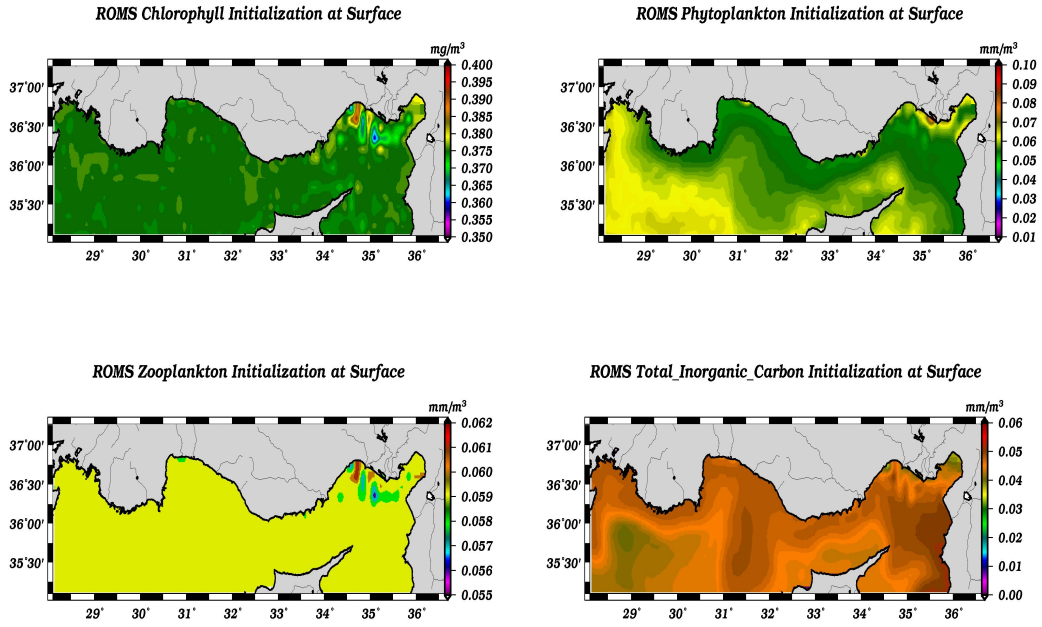

FIGURE 3.4: *Initial surface data for ecosystem variables chlorophyll, phytoplankton, zooplankton, total inorganic carbon (from top-left to bottom-right, respectively)*

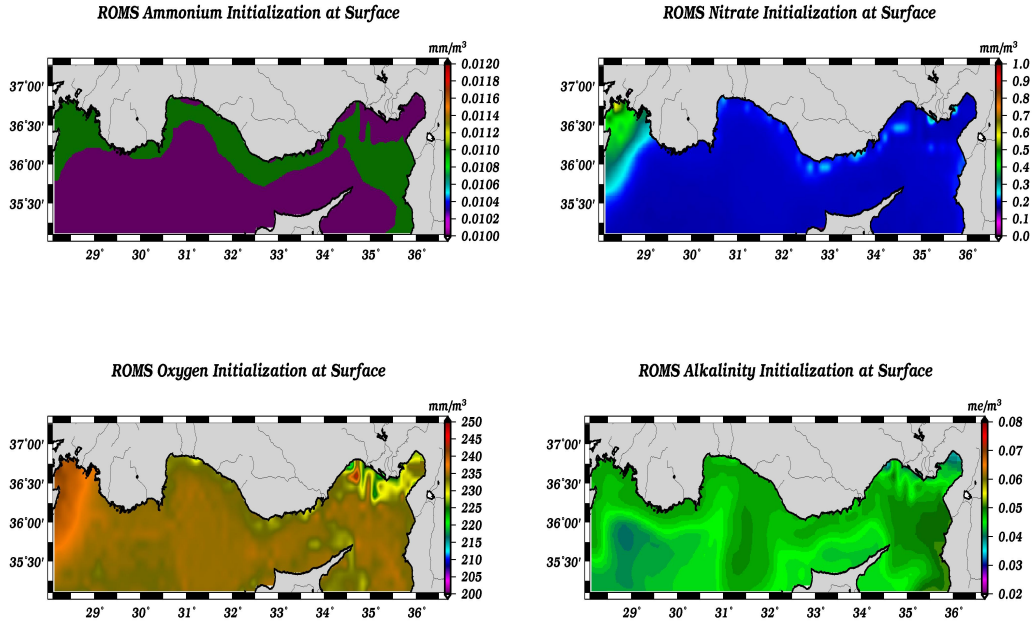

FIGURE 3.5: *Initial surface data for ecosystem variables NH4, NO3, oxygen, alkalinity (from top-left to bottom-right, respectively)*

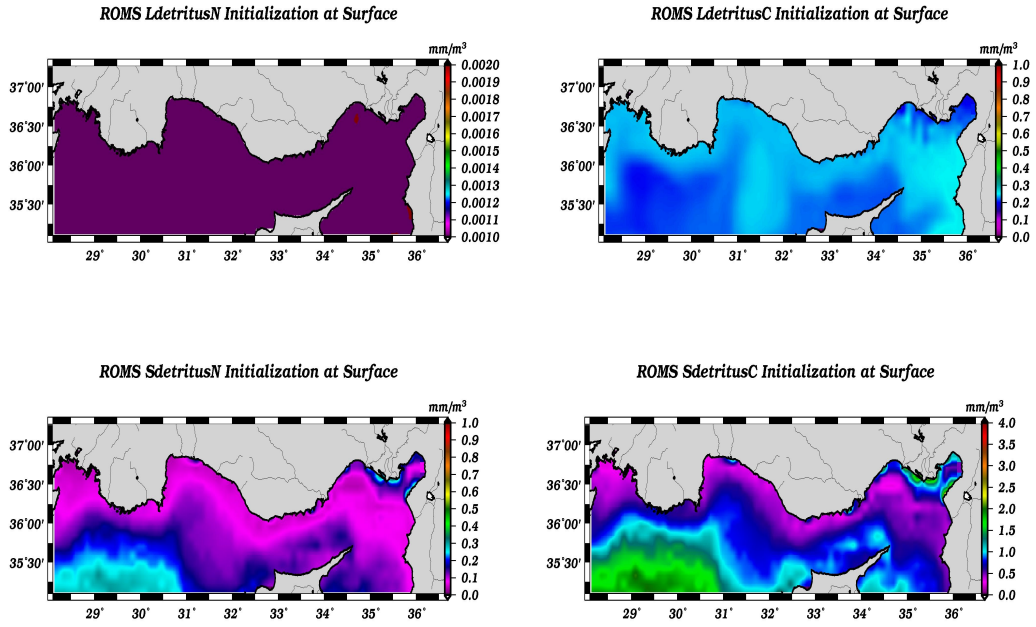

FIGURE 3.6: *Initial surface data for ecosystem variables large nitrogen detritus, large carbon detritus, small nitrogen detritus, small carbon detritus (from top-left to bottom-right, respectively)*

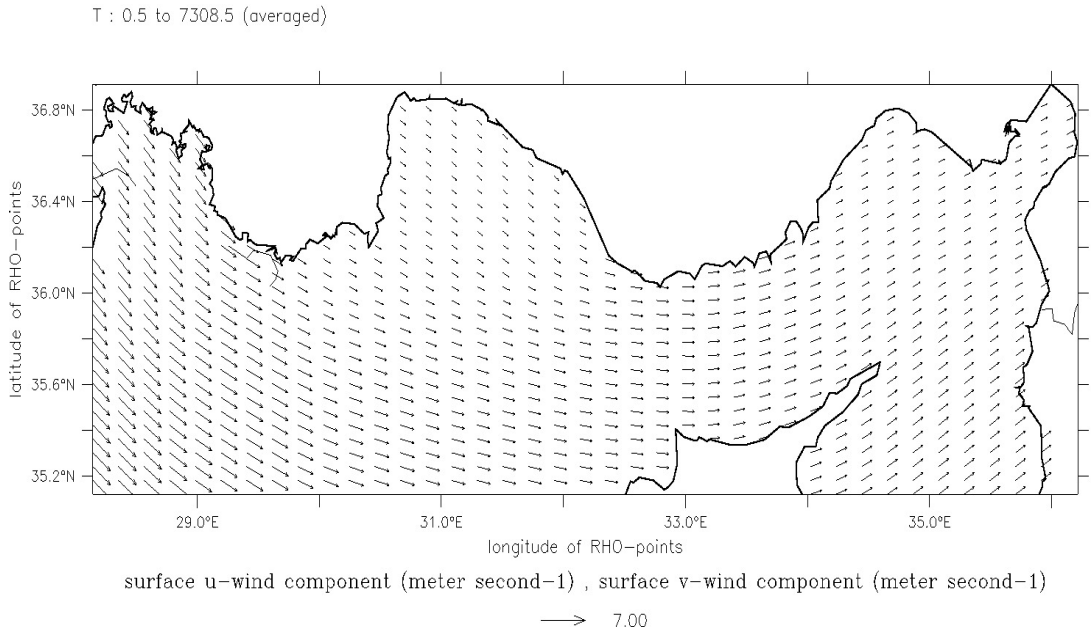

FIGURE 3.7: *Temporal average of wind stress for years 1996-2000*

3.2.4 Surface Atmospheric Forcing

Atmospheric forcing data comprises nine variables including u-wind (latitudinal), v-wind (longitudinal), surface air pressure, surface air temperature, surface air relative humidity, cloud fraction, rain fall rate, solar shortwave radiation and net longwave radiation are used to force model at the surface. Two different and relatively coarse datasets are used to simulate 5-year runs 1996-2000 and 2030-2034.

Surface forcing data for 5-year model runs are adapted from Istituto Nazionale di Geofisica e Vulcanologia (INGV) - SXG 20c3m simulations. The atmospheric climate change for 2030-2034 is realized by adopting the IPCC SRES A1B scenario which considers very rapid economic growth, low population growth, moderate resource use with a balanced use of technologies (Nakicenovic and Swart, 2000). Coarse resolution data (1.125°x1.125°) is interpolated to model grid (*Scoccimarro et al., 2007*). General averaged wind-stress pattern indicates the influence of northwesterly Etesian winds on averages (Fig. 3.7). Daily time-series for each variable are overlayed to easily compare the two datasets. In addition, overall averages for 5-year are indicated on the figures (see Fig. 3.8- 3.15 left viewport). Averages calculated for net longwave radiation, shortwave radiation, surface air temperature and surface air pressure are higher for 2030-2034 than 1996-2000. On the otherhand, decrease of wind speed, surface air relative humidity, cloud fraction and rainfall rate is recorded (Table 3.2).

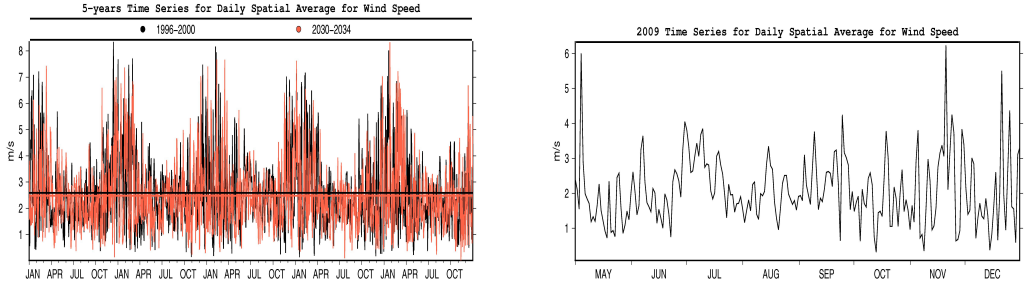

FIGURE 3.8: *Temporal wind speed variation for 5-year time sliced hydrodynamics-ecosystem coupled simulations and 2009 hydrodynamical simulations*

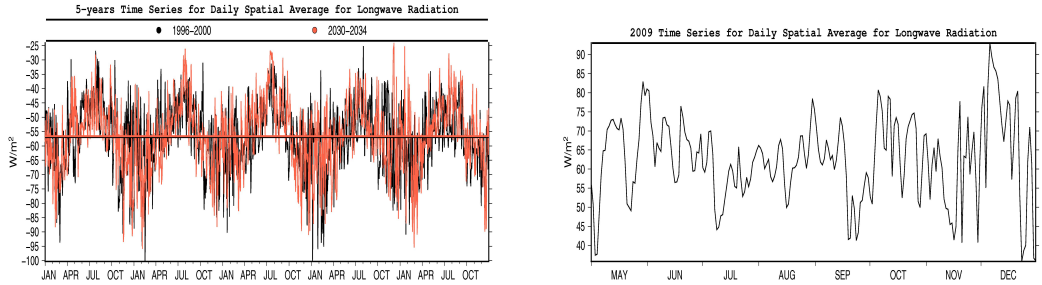

FIGURE 3.9: *Temporal long wave radiation variation for 5-year time sliced hydrodynamics-ecosystem coupled simulations and 2009 hydrodynamical simulations*

	Wind (m/2)	Longwave Radiation (W/m^2)	Shortwave Radiation (W/m^2)	Temperature (°C)
S1996-2000	2.58645	-56.9572	123.721	18.2402
S2030-2034	2.47933	-56.5763	125.324	18.6343
Difference	-0.1071	0.3809	1.6030	0.3940
	Pressure (mb)	Relative Humidity (%)	Cloud Fraction	Rain Fall (kg/m^2sec)
S1996-2000	1009.55	47.4222	0.155003	1.31082e-05
S2030-2034	1009.65	45.6012	0.130471	6.70301e-06
Difference	0.100	-1.8209	-0.0245	-6.405e-6

TABLE 3.2: *Comparison of spatio-temporal averages of atmospheric parameters for simulations 1996-2000 and 2030-2034*

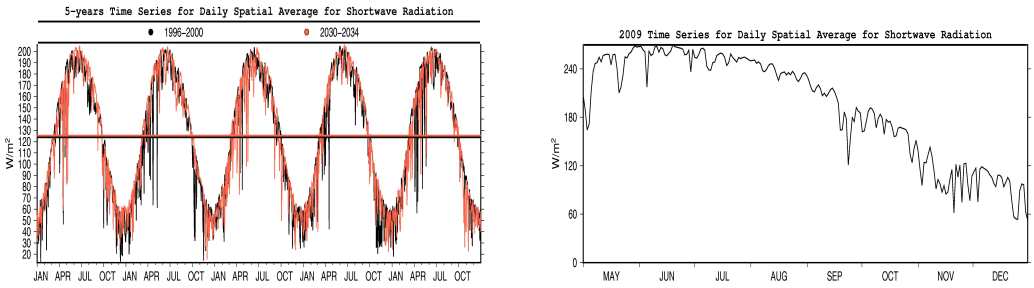

FIGURE 3.10: *Temporal short wave radiation variation for 5-year time sliced hydrodynamics-ecosystem coupled simulations and 2009 hydrodynamical simulations*

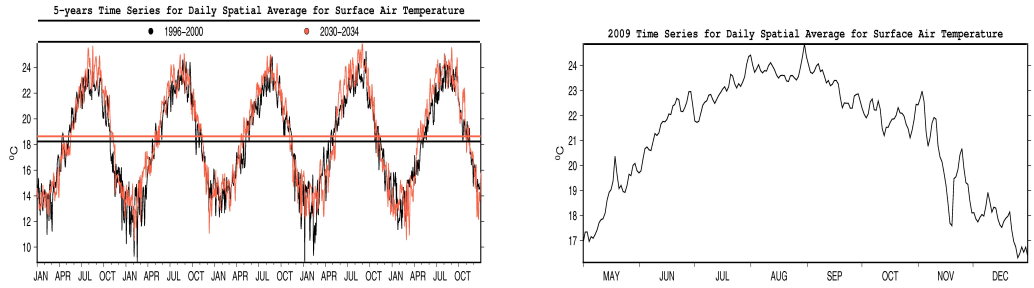

FIGURE 3.11: *Temporal surface air temperature variation for 5-year time sliced hydrodynamics-ecosystem coupled simulations and 2009 hydrodynamical simulations*

3.3 2009 Hydrodynamical Simulations

The coupled hydrodynamics-ecosystem simulations were carried out for two 5-year time slices in order to see the response of system to the climate change scenario described in sections above. Having done these two 5-year simulations with the coupled hydrodynamic-ecosystem model, sensitivity tests were applied to improve the hydrodynamical part of the model. In this section, the details of model configuration and datasets used in hydrodynamical runs will be provided.

3.3.1 Model Setup

Among the various alternatives, sensitivity tests were carried out for alternative sets of ROMS configuration switches listed in Table 3.3. The simulation run2009-110714 is an exception

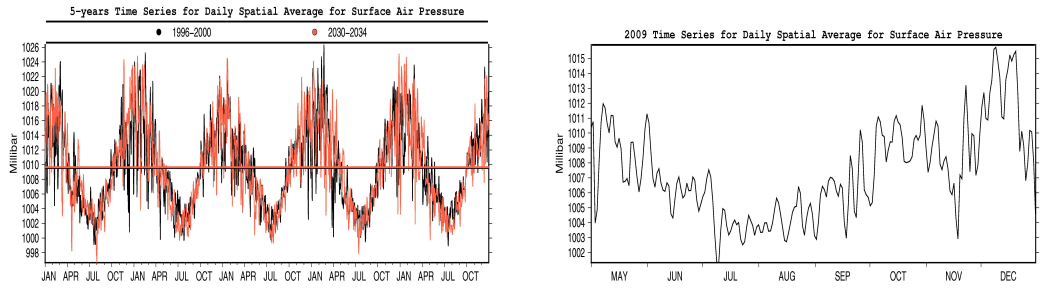

FIGURE 3.12: *Temporal surface air pressure variation for 5-year time sliced hydrodynamics-ecosystem coupled simulations and 2009 hydrodynamical simulations*

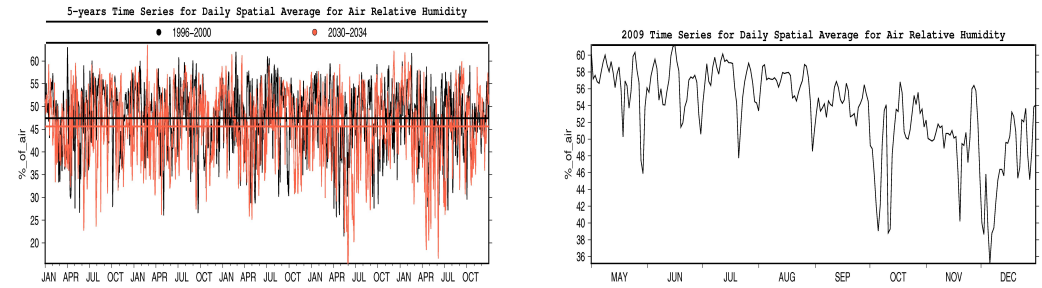

FIGURE 3.13: *Temporal surface air relative humidity variation for 5-year time sliced hydrodynamics-ecosystem coupled simulations and 2009 hydrodynamical simulations*

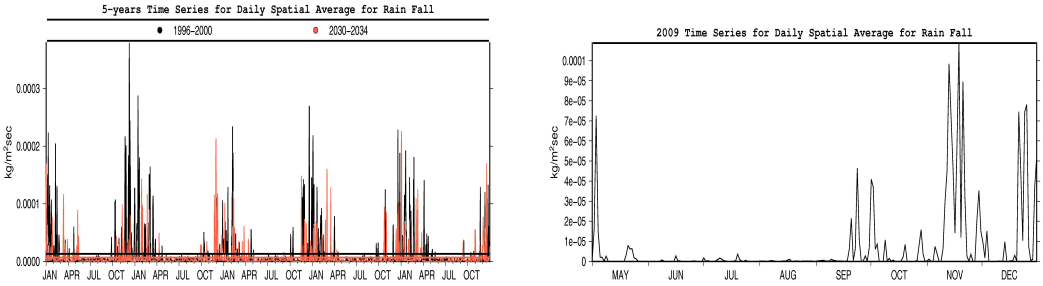

FIGURE 3.14: *Temporal rain fall variation for 5-year time sliced hydrodynamics-ecosystem coupled simulations and 2009 hydrodynamical simulations*

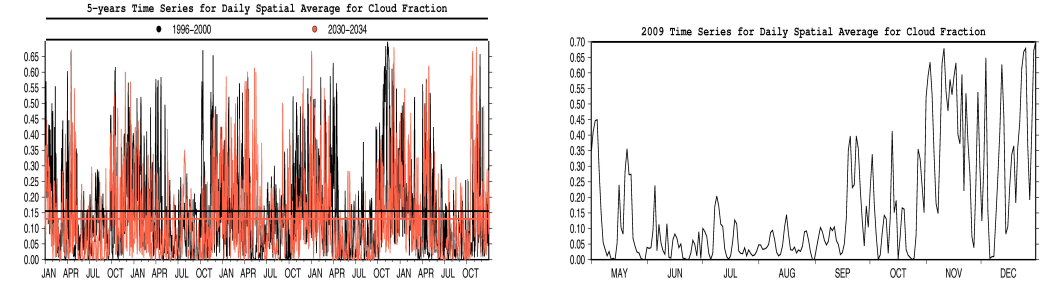

FIGURE 3.15: *Temporal cloud fraction variation for 5-year time sliced hydrodynamics-ecosystem coupled simulations and 2009 hydrodynamical simulations*

carried out with the physical configuration of the earlier simulations (section 3.2.1) in order to provide an opportunity to compare the 5-year simulations with the sensitivity tests. The reader can see *Warner et al. (2005)*, *Umlauf and Burchard (2003)*, and *Durski et al. (2004)* for full detailed theoretical information, experimental analysis and comparison of different vertical mixing schemes used in the sensitivity test runs. Results of these runs will be exhibited in section 4.7.

Switch / run2009-	110714	110729	110815	110818	110823	110907
Viscosity	UV_VIS4	UV_VIS2	UV_VIS2	UV_VIS2	UV_VIS2	UV_VIS2
Diffusivity	TS_DIF4	TS_DIF2	TS_DIF2	TS_DIF2	TS_DIF2	TS_DIF2
Longwave	closed	opened	opened	opened	opened	opened
Mixing	LMD	LMD	MY25	GLS (K-ϵ)	GLS (K-ω)	GLS (K-kl)

TABLE 3.3: *Switches used sensitivity test runs of hydrodynamical model*

3.3.2 Initialization

Sensitivity test runs are initialized at 1 May 2009 with the initial data provided by the University of Athens (UOA) Aegean-Levantine Regional Model (ALERMO). ALERMO has 471x321 horizontal grids with 1/30°resolution and 59 vertical levels. The data are interpolated from the ALERMO POM grid to the NLEV ROMS grid.

3.3.3 Boundary Fluxes

Boundary fluxes to nudge model from western and southern open boundaries are extracted from the ALERMO model and interpolated to the ROMS grid as described in section 3.3.2.

3.3.4 Atmospheric Surface Forcings

Atmospheric input data is interpolated from Non-hydrostatic SKIRON/Eta Modelling System of UOA. Using Arakawa E-grid, SKIRON has 1/20x1/20 degrees of horizontal resolution. The model is forced every hour by nine atmospheric variables defined above. The atmospheric data signifies the basic characteristics of the Levantine such as strong wind speed in autumn and winter (Fig. 3.8), increased radiation in spring and summer (Fig. 3.9- 3.10), increasing

surface temperature and reduced pressure levels during summer (Fig. 3.11- 3.12), elevated humidity in summer (Fig. 3.13) and intense rainfall occuring in autumn and winter (Fig. 3.14).

3.4 River input

River fluxes, used as fresh water input and nutrient source in the model, is gathered from "SESAME river runoff and nutrient load data sets" (Ludwig et al., 2009) and "A Study of the Ionic Composition and Inorganic Nutrient Fluxes from Rivers Discharging into the Cilician Basin, Eastern Mediterranean" (*T. Özsoy et al., 2008*). Furthermore, various UNEP reports and data archive of the State Water Supply Administration (http://www.dsi.gov.tr) were deeply checked to get a complete set of data.

14 Northern Levantine rivers are included in model simulations. Among these rivers Seyhan, Ceyhan, Göksu, Lamas, Berdan and Anamur are run into the Cilician Basin, and Asi (Orontes) flows into the Latakia Basin. Moreover, Düden, Karpuz, Kargı, Köprüçay, Manavgat reach to the Antalya Basin and Dalaman, Eşen rivers empty into the Rhodes Basin.

Ceyhan, Seyhan, Asi and Göksu are the major rivers that supply fresh water and nutrients to the basin. The total river discharge to the basin is approximately 22 km^3/year. The fresh water flux through the Ceyhan river can exceed 700 $m^3 s^{-1}$ during spring months (Table 3.4).

Asi and Seyhan rivers are main nutrient sources. Concentrations of NO_3 and NH_4 were found to be highest in Asi (203 μM and 55.7 μM) and in Seyhan (62 μM and 38.2 μM) rivers, respectively. Nutrient fluxes from some small-scale rivers are adjusted according to the measurements in the Berdan river due to lack of data (Tables 3.5 - 3.6).

Nutrient and water fluxes stated above were changed in forecast simulation (2030-2034) according to the projections of Ludwig et al. (2009). Water fluxes were decreased by 10% whereas nutrient fluxes were incresed by a factor of 2.5.

Due to the lack of individual data temperature values for all rivers were taken to be the same as the Asi river where temperature data were available. Temperature values adjusted from *Bozkurt et al. (2002)* were set as T=(15, 16, 17, 19, 22, 28, 27, 27, 25, 24, 19, 17) from January to December, respectively. All of the rivers are assumed to have a 20 psu salinity. Nutrient and water fluxes from rivers are inserted into the model calculations in the middle of every month as point sources.

River / Month	Jan	Feb	Mar	Apr	May	Jun	Jul	Aug	Sep	Oct	Nov	Dec
Seyhan	266.0	387.0	359.0	466.0	403.0	174.0	112.0	86.0	82.0	88.0	82.0	90.0
Ceyhan	377.0	661.0	509.0	727.0	385.0	195.0	70.0	46.0	59.0	94.0	91.0	127.0
Asi	246.0	379.0	174.0	103.0	64.0	48.0	6.0	5.0	27.0	53.0	50.0	32.0
Göksu	187.0	284.0	265.0	341.0	201.0	87.0	52.0	42.0	42.0	45.0	46.0	65.0
Lamas	4.0	5.0	11.0	18.0	12.0	7.0	6.0	5.0	5.0	4.0	3.0	3.0
Berdan	37.0	50.0	54.0	84.0	111.0	66.0	32.0	21.0	15.0	11.0	11.0	14.0
Anamur	45.0	71.0	42.0	54.0	75.0	42.0	14.0	8.0	6.0	5.0	6.0	18.0
Düden	27.0	34.0	27.0	22.0	28.0	23.0	21.0	19.0	17.0	13.0	14.0	15.0
Karpuz	12.0	23.0	10.0	6.0	4.0	1.0	0.0	0.0	0.0	0.0	0.0	15.0
Kargı	33.0	25.0	15.0	9.0	6.0	3.0	1.0	1.0	1.0	1.0	2.0	26.0
Köprüçay	188.0	175.0	117.0	137.0	117.0	77.0	53.0	43.0	43.0	48.0	84.0	244.0
Dalaman	115.0	105.0	98.0	83.0	52.0	25.0	15.0	9.0	13.0	18.0	24.0	80.0
Eşen	65.0	60.0	63.0	56.0	43.0	32.0	25.0	22.0	23.0	29.0	35.0	53.0
Manavgat	55.0	80.0	120.0	140.0	140.0	150.0	150.0	120.0	90.0	80.0	60.0	30.0

TABLE 3.4: *Monthly water discharges ($m^3 s^{-1}$) of the Northern Levantine rivers included in simulation 1996-2000*

River / Month	Jan	Feb	Mar	Apr	May	Jun	Jul	Aug	Sep	Oct	Nov	Dec
Seyhan	63.0	47.0	40.0	56.0	73.0	50.0	25.0	94.0	99.0	104.0	95.0	79.0
Ceyhan	100.0	92.0	78.0	90.0	87.0	82.0	77.0	78.0	100.0	123.0	145.0	123.0
Asi	225.0	248.0	323.0	240.0	204.0	167.0	165.0	171.0	180.0	150.0	144.0	220.0
Göksu	76.0	70.0	57.0	63.0	53.0	53.0	54.0	68.0	77.0	86.0	95.0	93.0
Lamas	86.0	93.0	85.0	83.0	79.0	73.0	67.0	101.0	98.0	95.0	92.0	89.0
Berdan	66.0	55.0	59.0	68.0	36.0	29.0	23.0	28.0	58.0	89.0	90.0	78.0
Anamur	66.0	55.0	59.0	68.0	36.0	29.0	23.0	28.0	58.0	89.0	90.0	78.0
Düden	66.0	55.0	59.0	68.0	36.0	29.0	23.0	28.0	58.0	89.0	90.0	78.0
Karpuz	66.0	55.0	59.0	68.0	36.0	29.0	23.0	28.0	58.0	89.0	90.0	78.0
Kargı	66.0	55.0	59.0	68.0	36.0	29.0	23.0	28.0	58.0	89.0	90.0	78.0
Köprüçay	66.0	55.0	59.0	68.0	36.0	29.0	23.0	28.0	58.0	89.0	90.0	78.0
Dalaman	66.0	55.0	59.0	68.0	36.0	29.0	23.0	28.0	58.0	89.0	90.0	78.0
Eşen	66.0	55.0	59.0	68.0	36.0	29.0	23.0	28.0	58.0	89.0	90.0	78.0
Manavgat	66.0	55.0	59.0	68.0	36.0	29.0	23.0	28.0	58.0	89.0	90.0	78.0

TABLE 3.5: *Monthly NO_3 discharges (μM) of the Northern Levantine rivers included in simulation 1996-2000*

River / Month	Jan	Feb	Mar	Apr	May	Jun	Jul	Aug	Sep	Oct	Nov	Dec
Seyhan	22	23.9	16.1	10.4	1.1	1.8	2.5	60	127	113.6	80.2	20.3
Ceyhan	8.5	7.5	6.8	6.5	6.2	7.2	7.8	7.6	7.4	9.0	10.5	9.5
Asi	104.8	92.9	95.2	82.1	21.4	21.4	27.4	14.3	8.81	65.5	70.2	65.5
Göksu	85	55.22	3.05	0.5	1.9	8	15.1	16	17.5	50	70.1	115.8
Lamas	65	90.8	1	1	0.7	0.4	0.2	1	2	1	.5	42.5
Berdan	29.9	29.5	7.4	7	6.1	3	1	14	28.3	32.1	14.9	30.8
Anamur	29.9	29.5	7.4	7	6.1	3	1	14	28.3	32.1	14.9	30.8
Düden	29.9	29.5	7.4	7	6.1	3	1	14	28.3	32.1	14.9	30.8
Karpuz	29.9	29.5	7.4	7	6.1	3	1	14	28.3	32.1	14.9	30.8
Kargı	29.9	29.5	7.4	7	6.1	3	1	14	28.3	32.1	14.9	30.8
Köprüçay	29.9	29.5	7.4	7	6.1	3	1	14	28.3	32.1	14.9	30.8
Dalaman	29.9	29.5	7.4	7	6.1	3	1	14	28.3	32.1	14.9	30.8
Eşen	29.9	29.5	7.4	7	6.1	3	1	14	28.3	32.1	14.9	30.8
Manavgat	29.9	29.5	7.4	7	6.1	3	1	14	28.3	32.1	14.9	30.8

TABLE 3.6: *Monthly NH_4 discharges (μM) of the Northern Levantine rivers included in simulation 1996-2000*

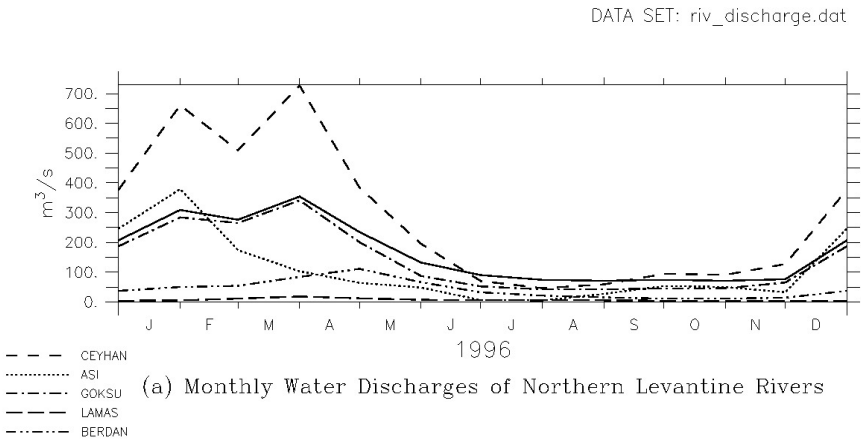

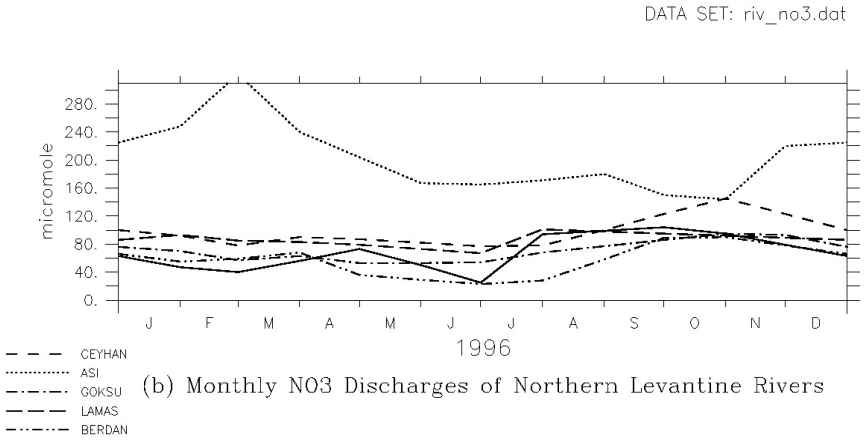

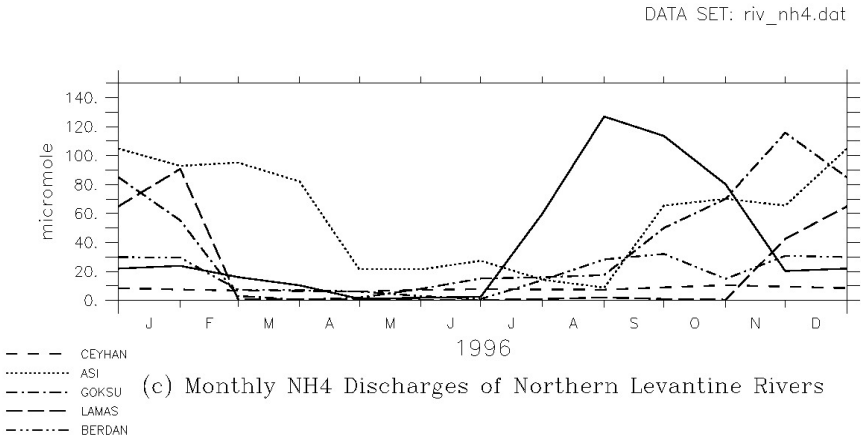

FIGURE 3.16: *Monthly fluxes of (a) water discharge, (b) NO_3, (c) NH_4 for the Northern Levantine rivers*

CHAPTER 4

RESULTS

In this chapter results of two 5-year (1996-2000 and 2030-2034) hydrodynamic-ecosystem online coupled models will be presented. The main focus for discussion will be on the 1996-2000 simulation since it gives an opportunity to be compared and validated with available satellite data at the surface. The 2030-2034 simulation is performed to see the effects of different atmospheric conditions (Section 3.2.4) on the physical dynamics and biogeochemistry of Northern Levantine Sea.

In addition to these climatic simulations, results of six hydrodynamical runs for the period May-December of 2009 will be compared to make improvements on problematic aspects of the 5-year time sliced coupled model runs. One of these test simulations is configured the same way as the 1996-2000 simulation and output is compared with different model setups considered to be more suitable for study area.

In the first section of this chapter, general circulation properties of the basin that the model resolved will be shown. Horizontal and vertical behaviours of the Asia Minor Current and the Rhodes Gyre will be given special interest. In *Section 4.2*, vertical mixing results will be demonstrated. Two different longitudinal and latitudinal cross-sections are taken into account for analysis. The thermohaline structure of the study area will be the main focus of *Section 4.3*. In *Section 4.4*, sea surface temperature and sea level anomaly will be validated with AVHRR satellite data and AVISO satellite data, respectively. Moreover, surface chlorophyll distributions are compared with SEAWIFS chlorophyll data matching with model run period. *Section 4.5* will be on discussion of ecosystem variables. Temporal variation and vertical profiles will be considered. Comparison of 2030-2034 forecast with 1996-2000 hindcast will be included in *Section 4.6*. Finally, in *Section 4.7*, sensitivity tests that are fulfilled to improve existing discrepancies will be submitted.

4.1 General Circulation

The Rossby radius of deformation is the measure of length in which rotational motions become important for fluids. NLEV model resolution is determined to be 1.35 *km* and it is far less than Rossby radius of deformation proposed by *The POEM Group (1992)* for Levantine Sea (10 - 15 *km*). As a result of being high resolution, model is expected to resolve sub-basin scale and mesoscale circulation structures as long as the horizontal viscosity and diffusivity parametrizations are appropriate.

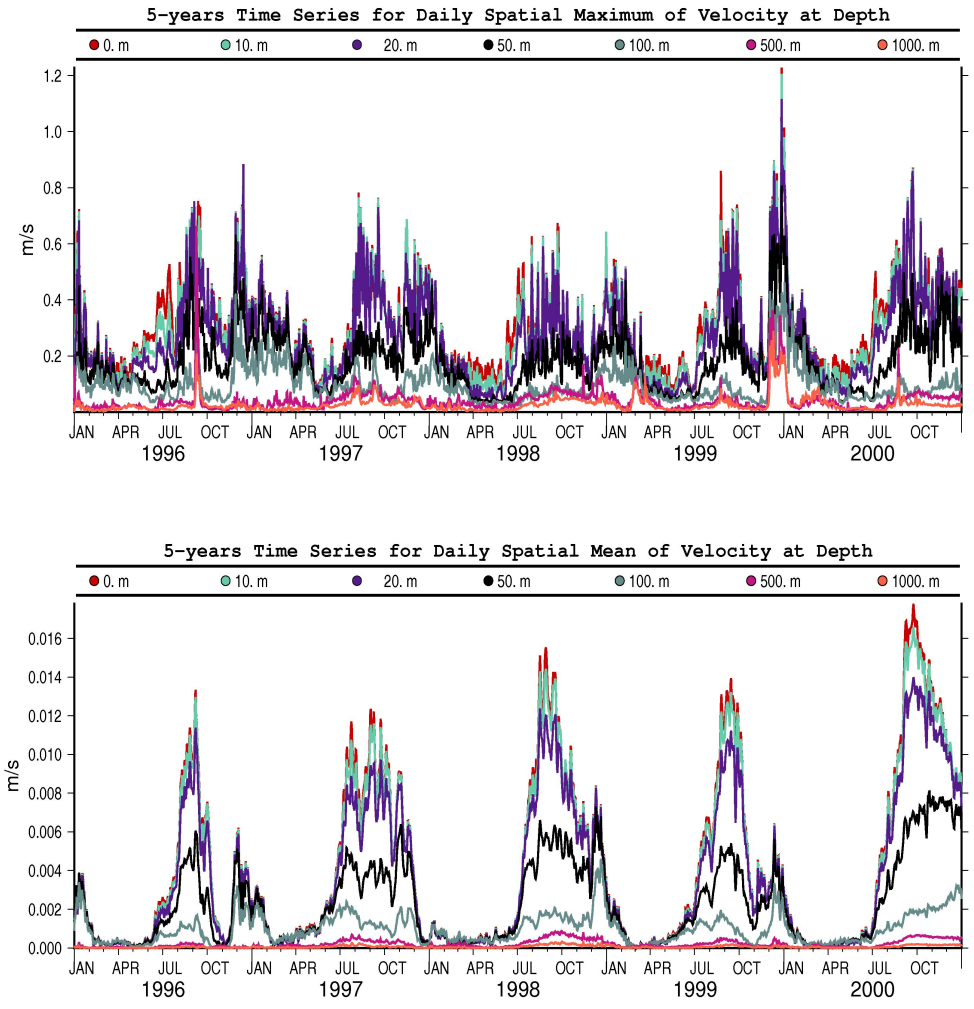

FIGURE 4.1: *Daily spatial maximum and average of current speed between years 1996 and 2000 at depths 0m, 10m, 20m, 50m, 100m, 500m, 1000m*

Main circulation features of Northern Levantine to be discussed in this chapter are Asia Minor Current (AMC) and Rhodes Gyre. Structure of AMC is important since it crosses

the region of formation for Levantine Intermediate Water (LIW) and therefore is responsible for its transport. On the other hand, Rhodes Gyre is a significant hydrodynamic structure of Mediterranean. Since it is a permanent feature, it permits validation of the models.

Fig. 4.1 shows daily spatial maximum and average of current speed along AMC at different depths. In general, the maximum velocity of the AMC tends to be around 0.8 $m\ s^{-1}$. According to the model results, the average current speed for the whole basin surface over five years is calculated to be 0.412 $cm\ s^{-1}$ (see Table 4.1).

Monthly averaged circulation patterns of the basin between years 1996 and 2000 are presented between Fig. 4.2 and 4.7.

Surface circulation for each month is displayed in Fig. 4.2 and 4.3. Horizontal velocity of the AMC is low in February and spring months, and it is rarely distinguised from mean circulation. Distinguishing horizontal characteristics of AMC reveal themselves after June. The current gets stronger towards the middle of the stratification season and degrading in autumn in its kinetic energy is again followed by an increase in strong mixing season. The pathway of the AMC seems to fit to the lateral boundaries of study area. After gaining speed just after St. Andreas (Karpas) Cape, current moves along Anatolian coast reaching Rhodes where it splits into two one of which heads towards Aegean Sea and other to the Crete.

Rhodes Gyre appears between 28E - 30E and 35N - 36N at all monthly averages with different formations. It is getting narrower in summer by stretching itself in north-south direction. A zonal flow detached from gyre moves towards east in autumn and winter. Just before reaching to Cyprus, brances of flow move north and south to encircle the island.

Longitudinal 28.95E (Rhodes Gyre) and latitudinal 36.02N (AMC) horizontal sections are visualized in Fig. 4.4 -4.7 until 300 m to see vertical structure of circulation. 28.95E (Rhodes Gyre) section is chosen to display vertical behaviour of Rhodes Gyre. On the other hand, 36.02N section crosses Asia Minor Current from various parts and ends at its region of convergence to Rhodes Gyre (Fig. 3.1).

Asia Minor Current along its path penetrates more than 300 m depth. Between February and June, average current speed is almost the same until 1000 m depth (Fig. 4.1). Then it starts to differentiate and strong stratification occurs in August and September. Current speed exceeds 0.3 $m\ s^{-1}$ even in depths between 75 m and 100 m (Fig. 4.6). In these months, characteristics of surface velocity fields reaches at most 50 m depths.

The cyclonic structure of Rhodes Gyre is well-captured by the model (Fig. 4.4 - 4.7 left panel). Inflow enters from south turns to west around 35.75N in a tangential position with

AMC. Angular velocity of the Gyre rarely exceeds 0.1 $m\ s^{-1}$ except in December.

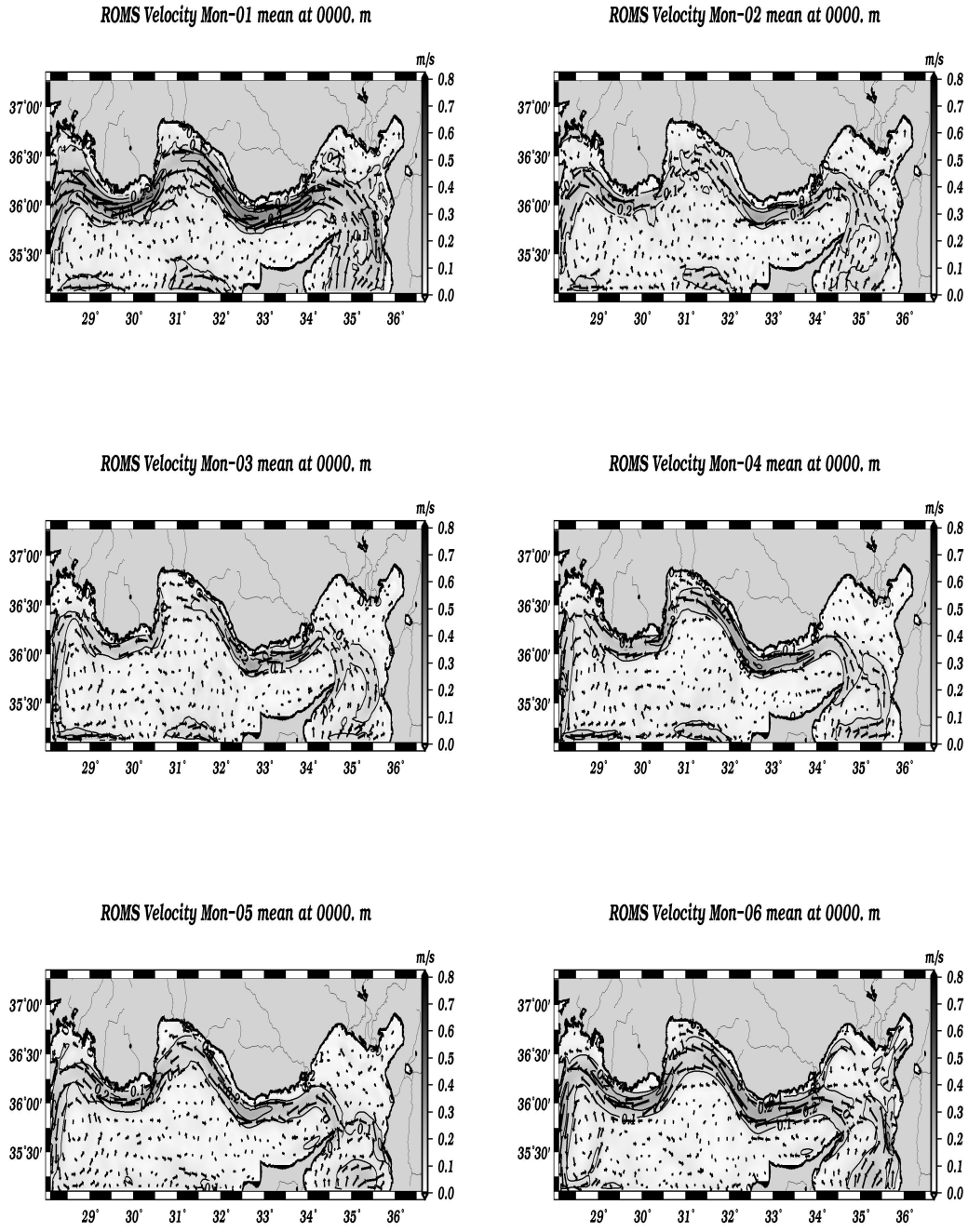

FIGURE 4.2: *Monthly averaged sea surface circulation between 1996-2000 in January, February, March, April, May and June*

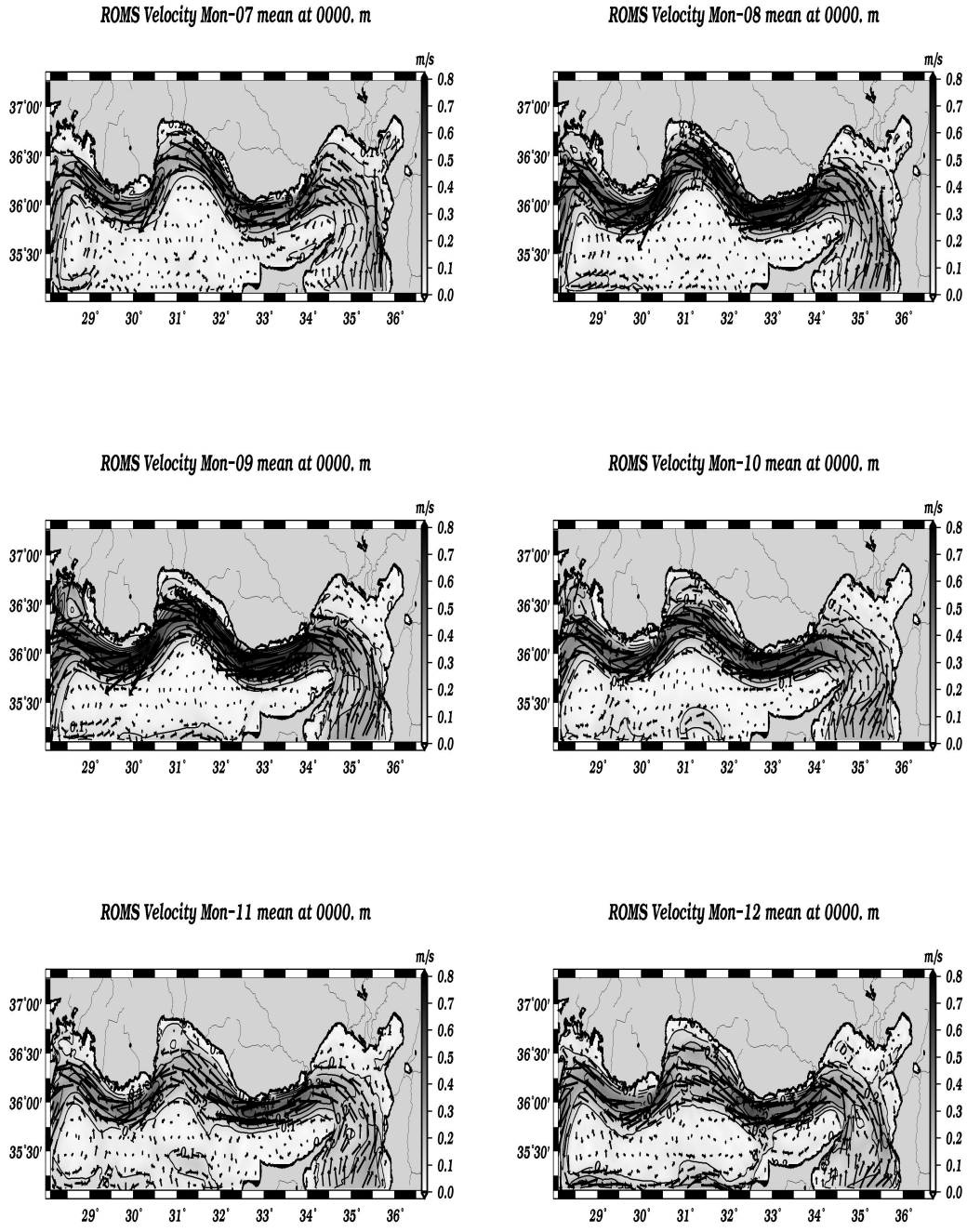

FIGURE 4.3: *Monthly averaged sea surface circulation between 1996-2000 in July, August, September, October, November and December*

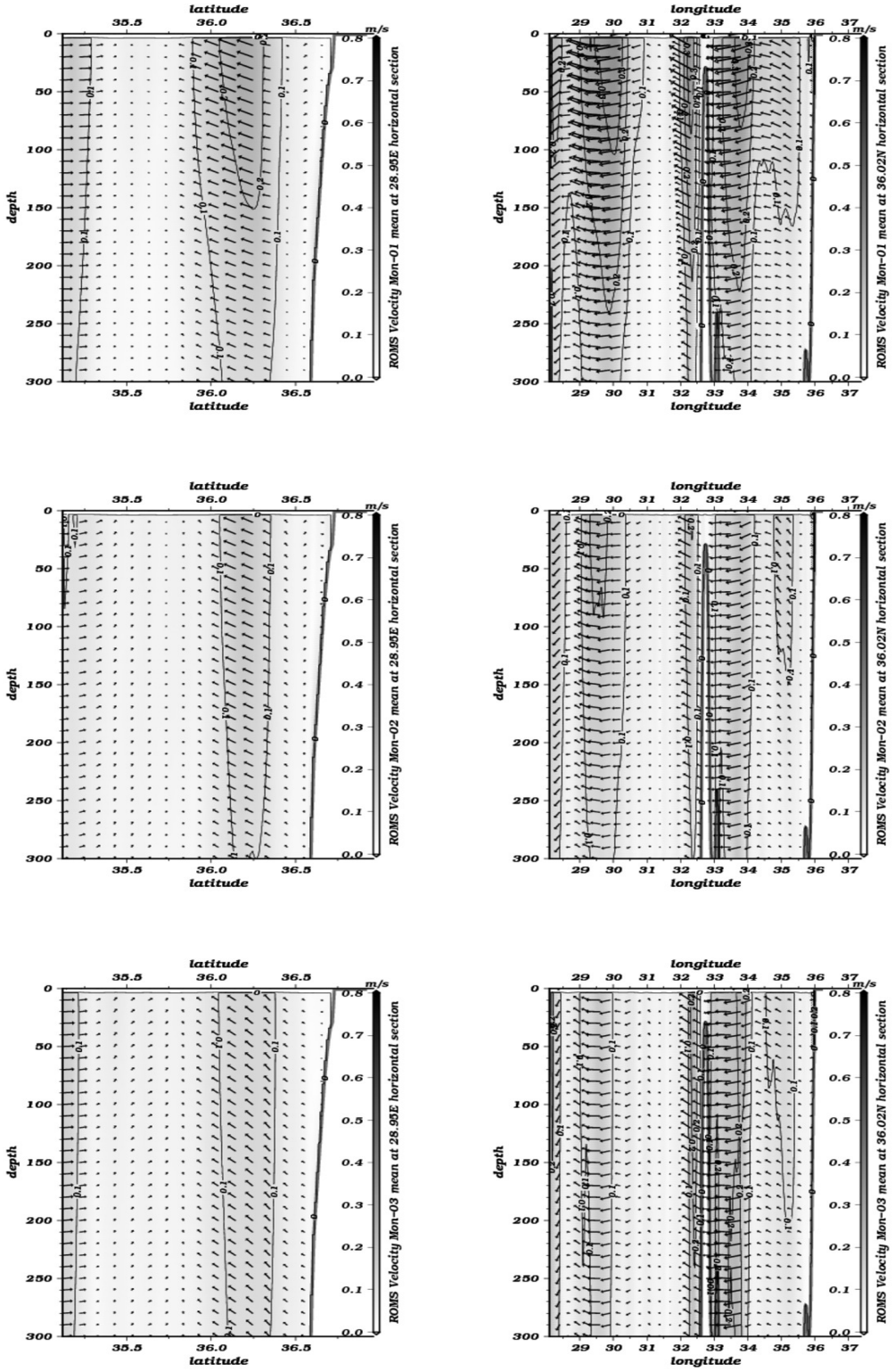

FIGURE 4.4: *Monthly averaged circulation for 28.95E (Rhodes Gyre) and 36.02N (AMC) horizontal section between 1996-2000 in January, February, March*

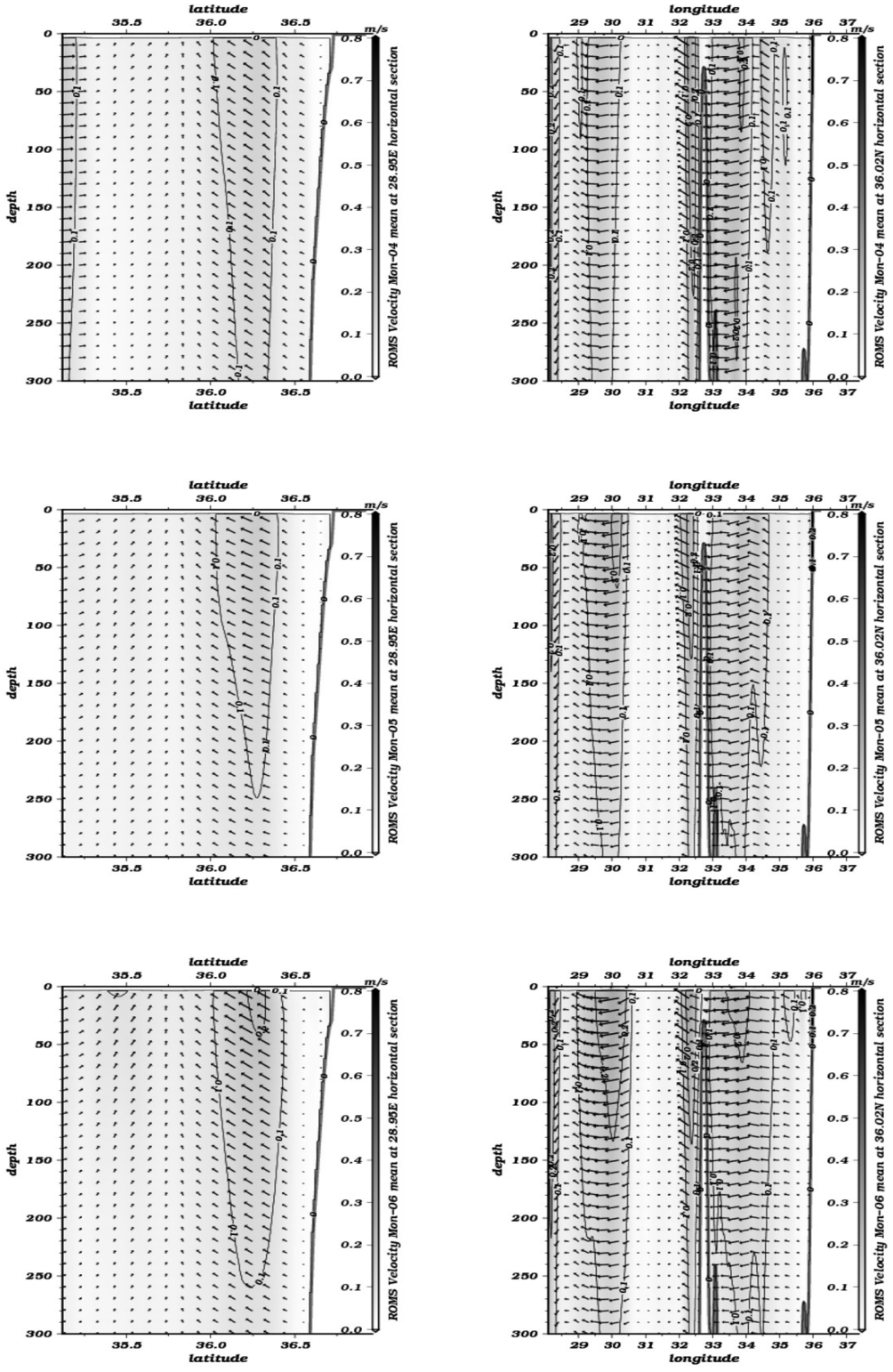

FIGURE 4.5: *Monthly averaged circulation for 28.95E (Rhodes Gyre) and 36.02N (AMC) horizontal section between 1996-2000 in April, May and June*

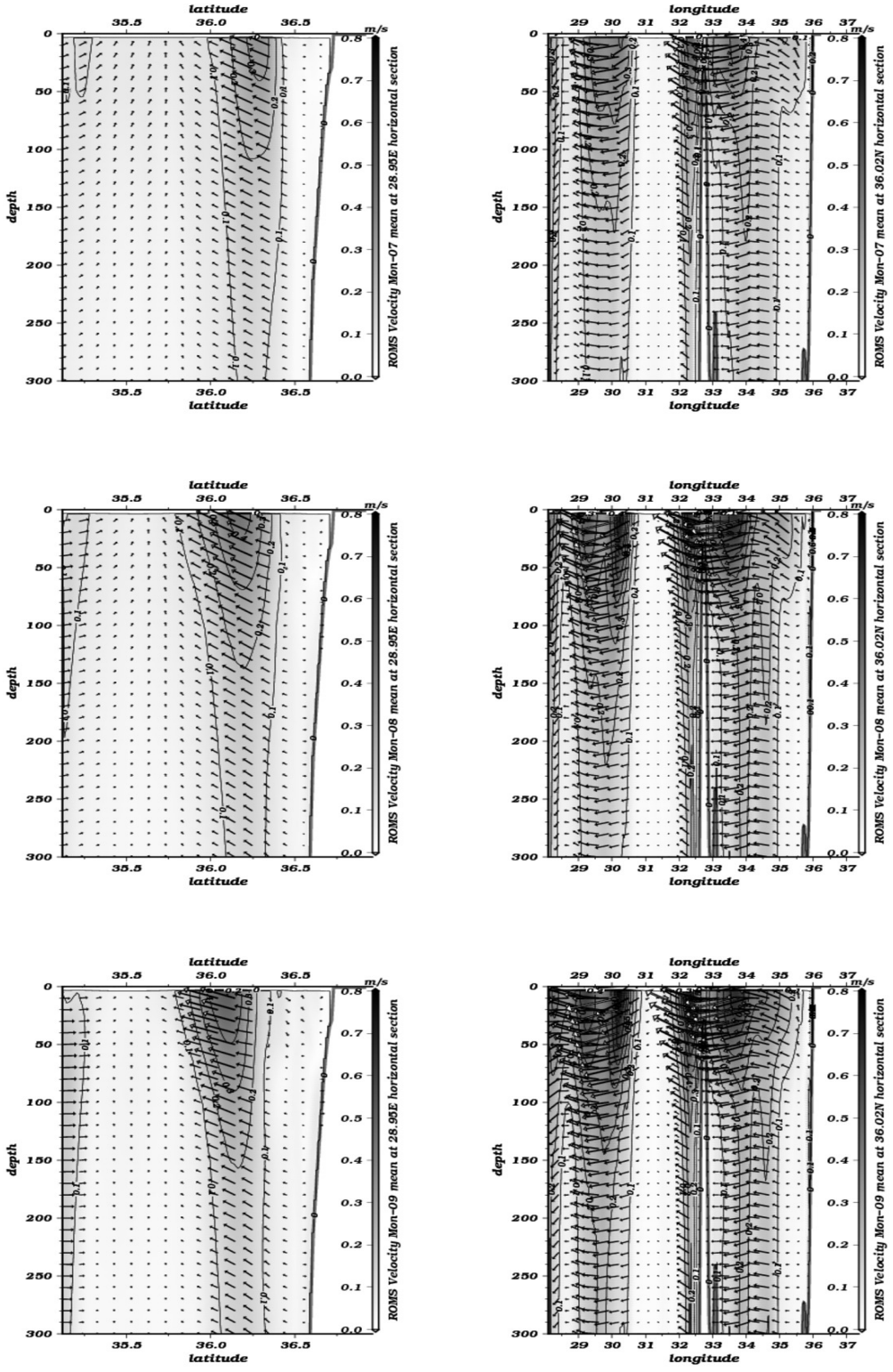

FIGURE 4.6: *Monthly averaged circulation for 28.95E (Rhodes Gyre) and 36.02N (AMC) horizontal section between 1996-2000 in July, August, September*

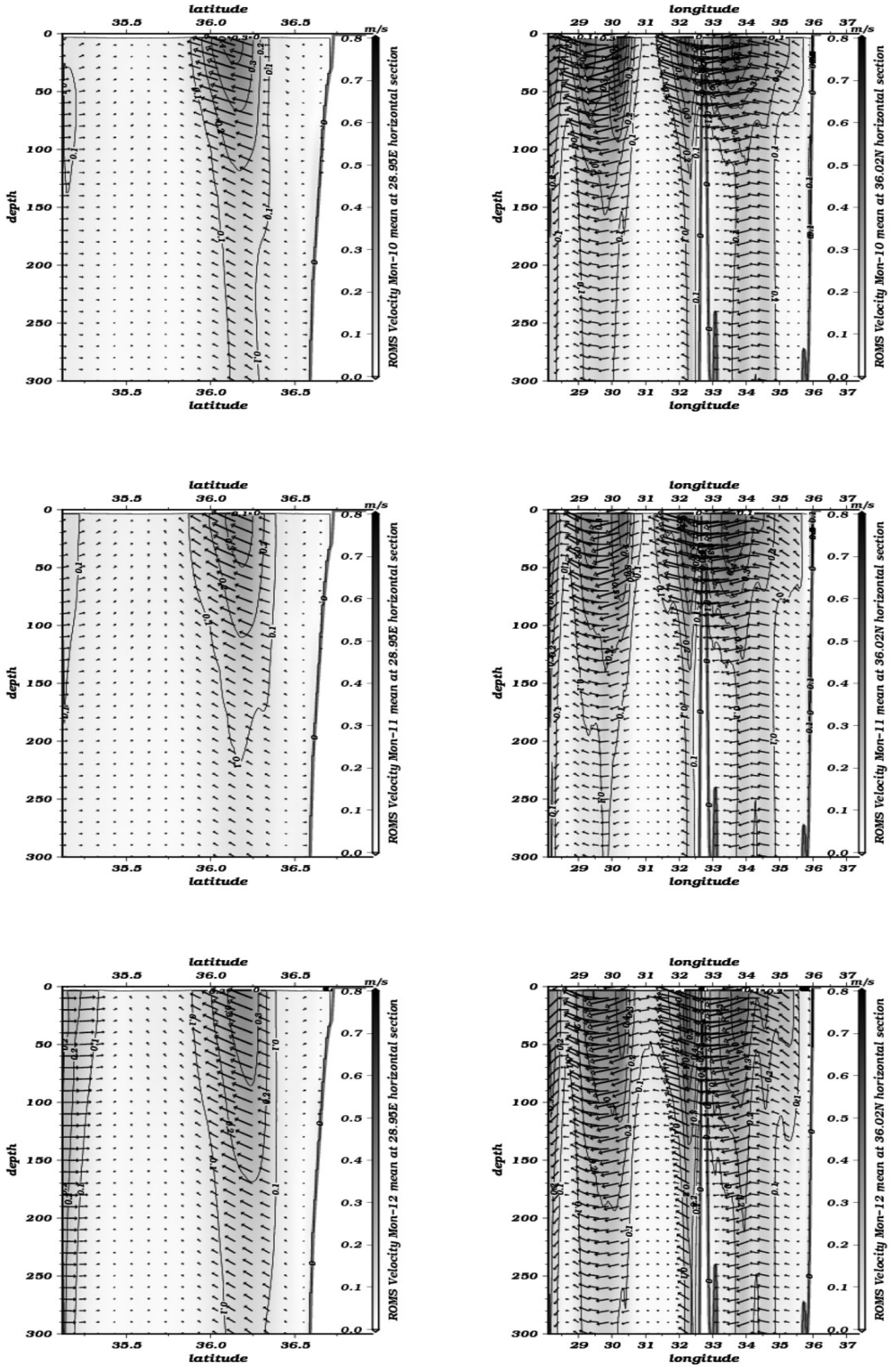

FIGURE 4.7: *Monthly averaged circulation for 28.95E (Rhodes Gyre) and 36.02N (AMC) horizontal section between 1996-2000 in October, November, December*

4.2 Vertical Mixing

In this section, physical tracers, temperature and salinity, will be used to discuss the vertical mixing of Northern Levantine Sea. Results will again be presented on 36.02N and 28.95E horizontal sections crossing AMC and Rhodes Gyre, respectively.

Monthly averages imply that section of basin along Rhodes Gyre is totally mixed vertically at the beginning of spring, namely in March (Fig. 4.8). Stratification starts to occur after April due to increasing incoming heat flux and surface mixed layer depth getting narrower (Fig. 4.9). During June and July, the surface mixed layer almost disappers offshore (Fig. 4.9 and 4.10). After August, the effect of strong heat flux from the atmosphere causes the surface mixed layer to deepen 50 *m* inshore (Fig. 4.10). The domination of northerly cold winds and a decrease in atmospheric radiation and heat flux after September gradually results in a totally mixed surface layer inshore and offshore in March (Fig. 4.11).

The temporal change of surface mixed layer structure is similar for AMC and Rhodes Gyre sections. However, the heat content in eastern Cyprus is greater than the western section which leads to different mixed layer depths in different parts of basin. Furthermore, the influences of topographic features can be monitored from AMC cross-sections. Inshore, heat content is greater than offshore and depths of thermocline and mixed layer are greater, especially between Turkey and St. Andreas (Karpas) Cape.

Vertical profiles of each month at the periphery of the Rhodes Gyre (36.02N (AMC) - 28.95E) where two analysed sections intersect reveal that surface water temperature starts to increase and gains a significant difference compared to intermediate water after May (Fig. 4.12). This process ends up with the formation of the thermocline in September, which reaches 30 *m* depth and gradually disappears until March. In the first 100 *m* temperature is maximum in September, whereas between 100 - 300 *m* most probably because of high heat content and strong mixing due to northerly winds, temperature maximum is seen in January. Maximum water temperature is 26 °C along the water column. Gradient due to seasonality of temperature almost disappears after 500 *m*. Temperature drops down under 15 °C.

Salinity profiles (Fig. 4.12 bottom panel) support the vertical mixing properties exerted by temperature results. Halocline explicitly occurs in the first 20 *m* and intermediate water at most reaches 60 *m* in October. Maximum of salinity in January along intermediate water column resembles temperature profiles of the same region.

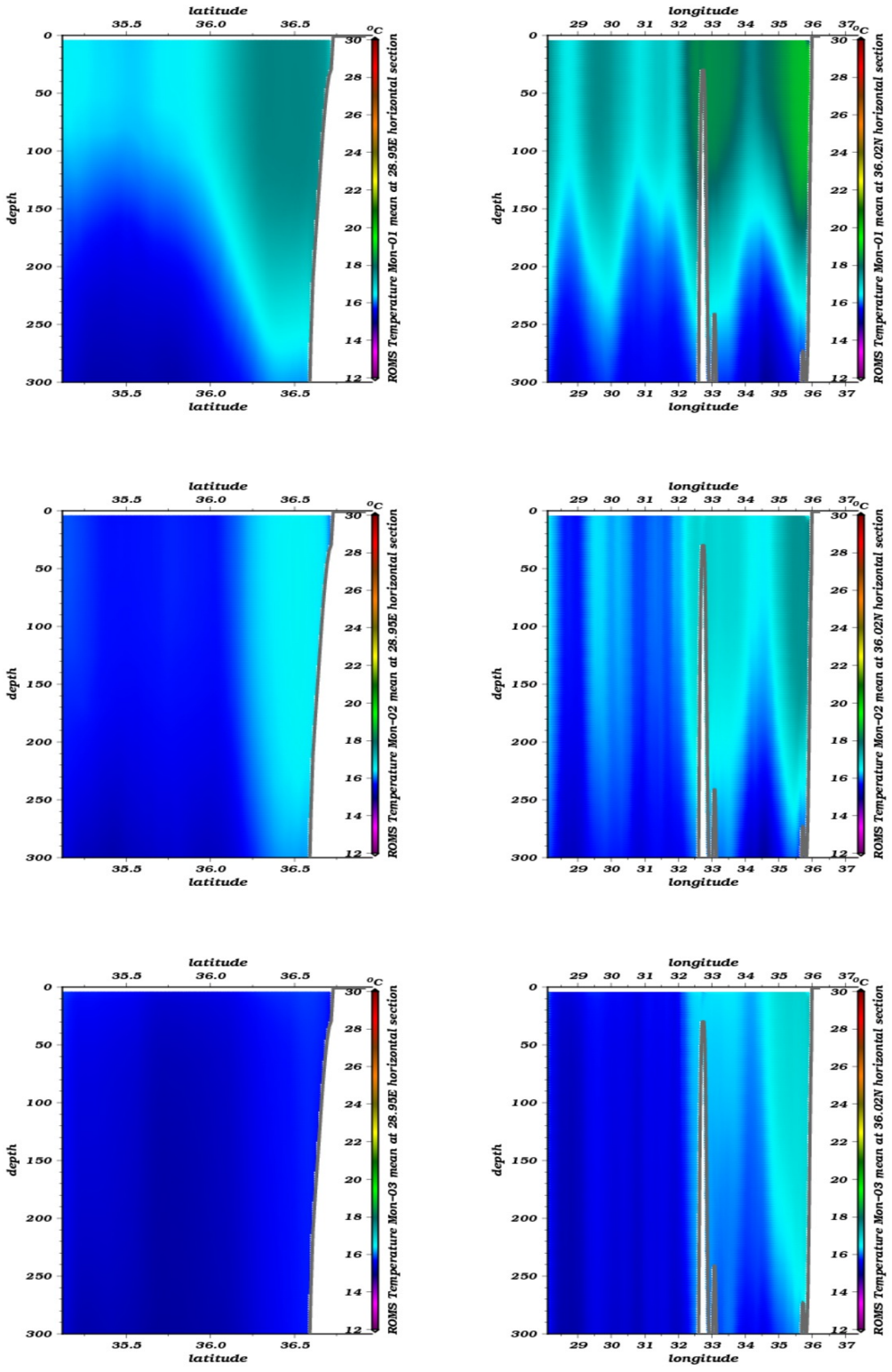

FIGURE 4.8: *Monthly averaged temperature for 28.95E (Rhodes Gyre) and 36.02N (AMC) horizontal sections over years 1996 - 2000 in January, February and March*

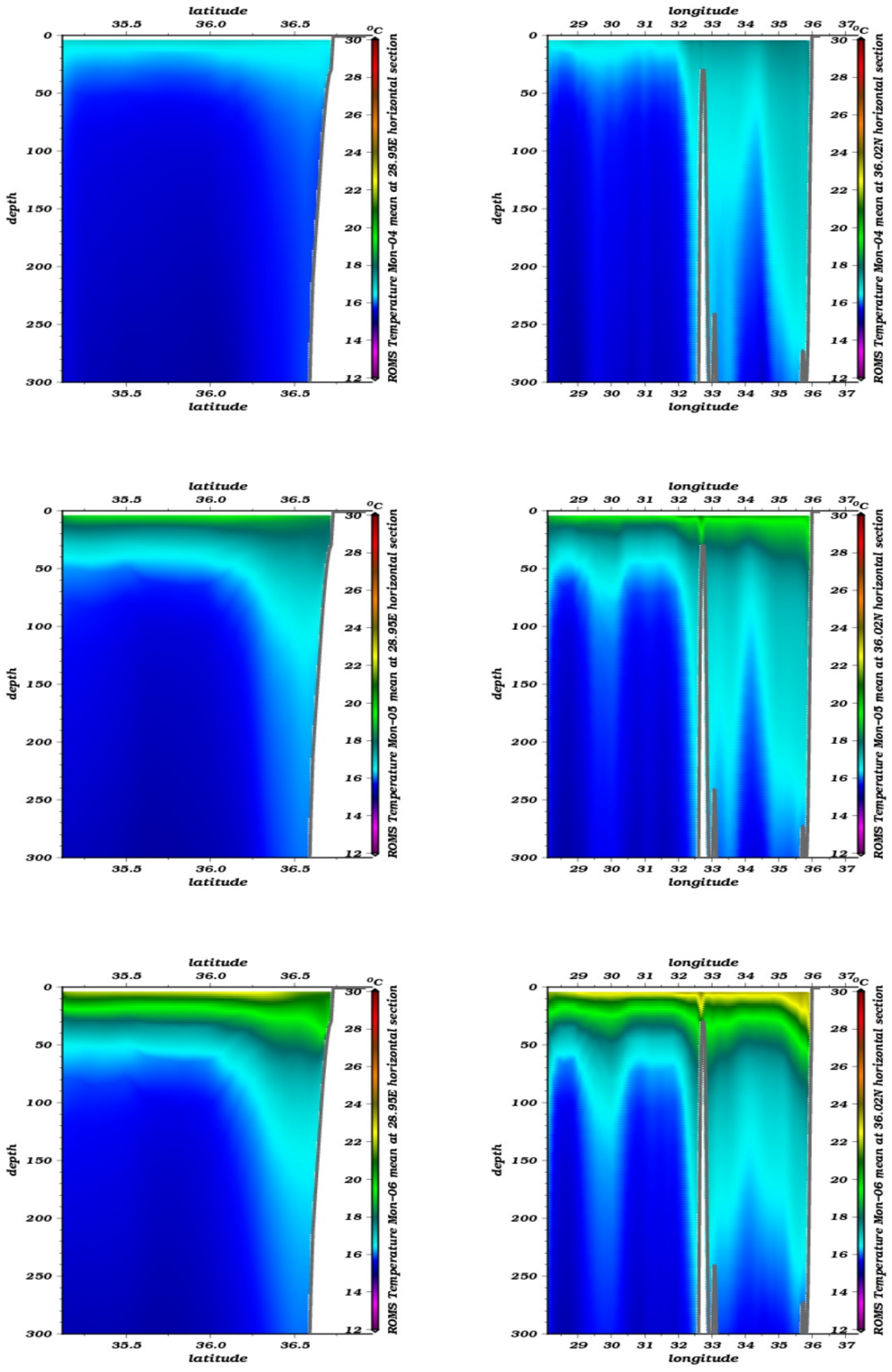

FIGURE 4.9: *Monthly averaged temperature for 28.95E (Rhodes Gyre) and 36.02N (AMC) horizontal sections over years 1996 - 2000 in April, May and June*

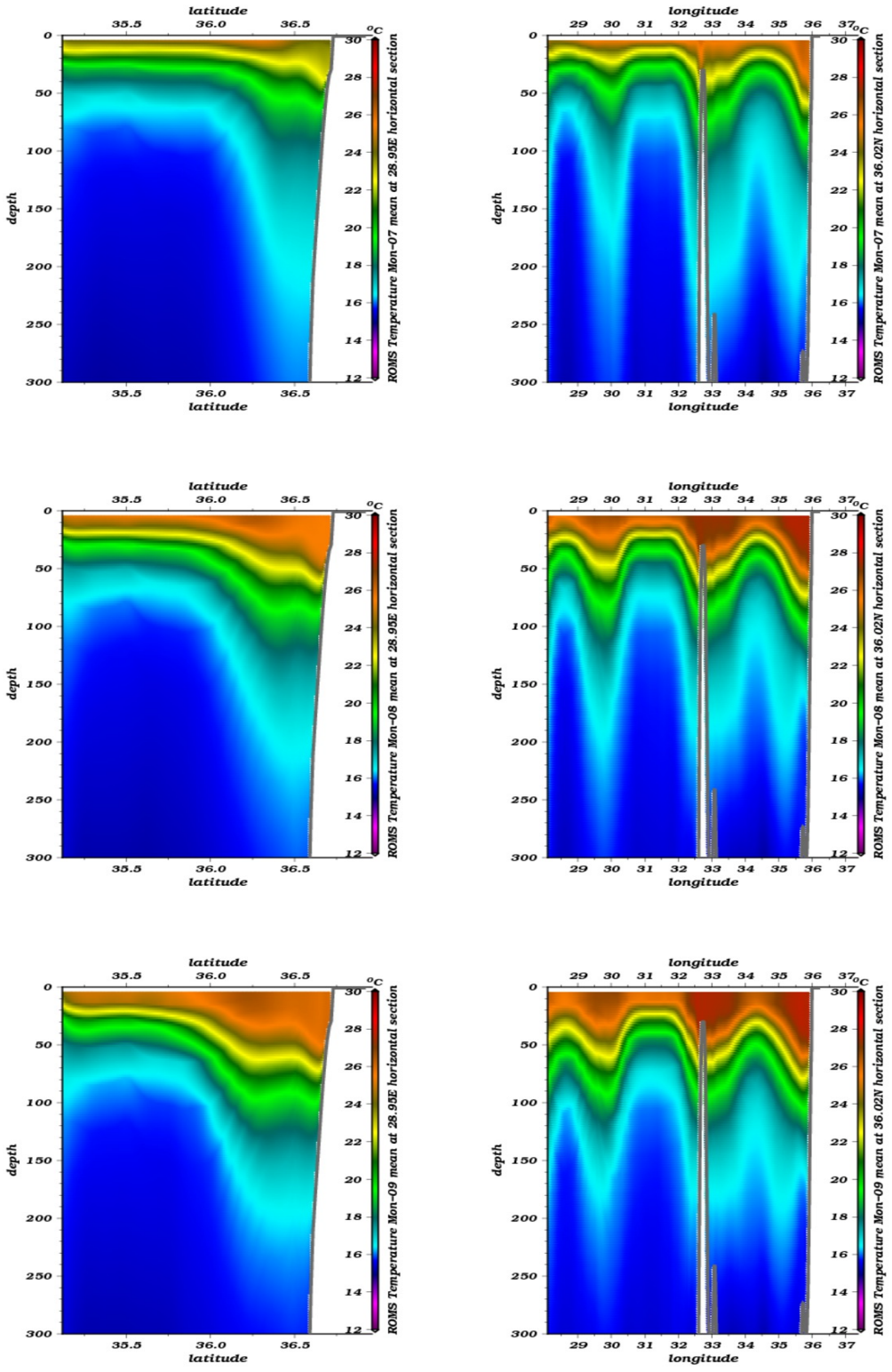

FIGURE 4.10: *Monthly averaged temperature for 28.95E (Rhodes Gyre) and 36.02N (AMC) horizontal sections over years 1996 - 2000 in July, August and September*

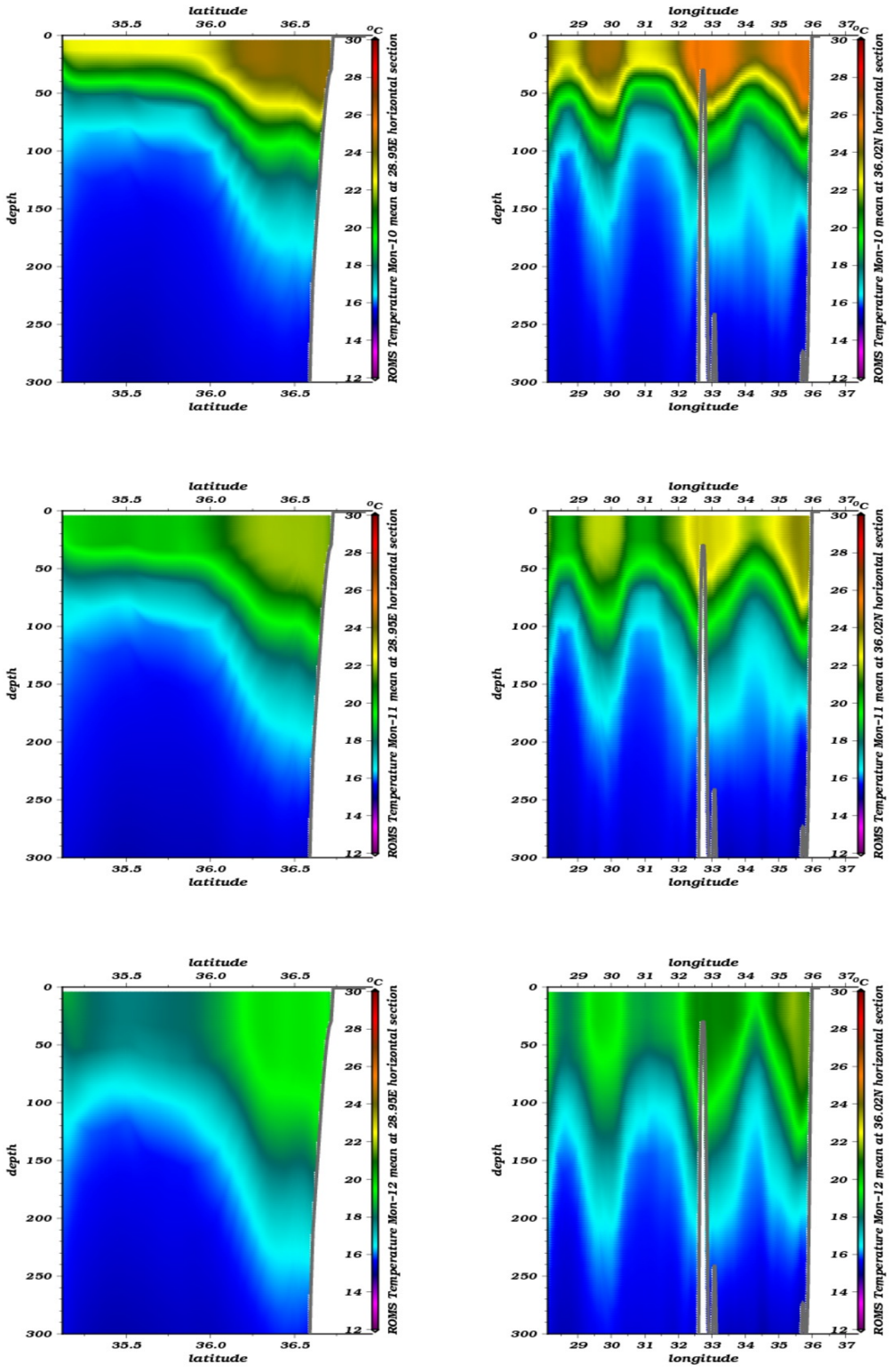

FIGURE 4.11: *Monthly averaged temperature for 28.95E (Rhodes Gyre) and 36.02N (AMC) horizontal sections over years 1996 - 2000 in October, November and December*

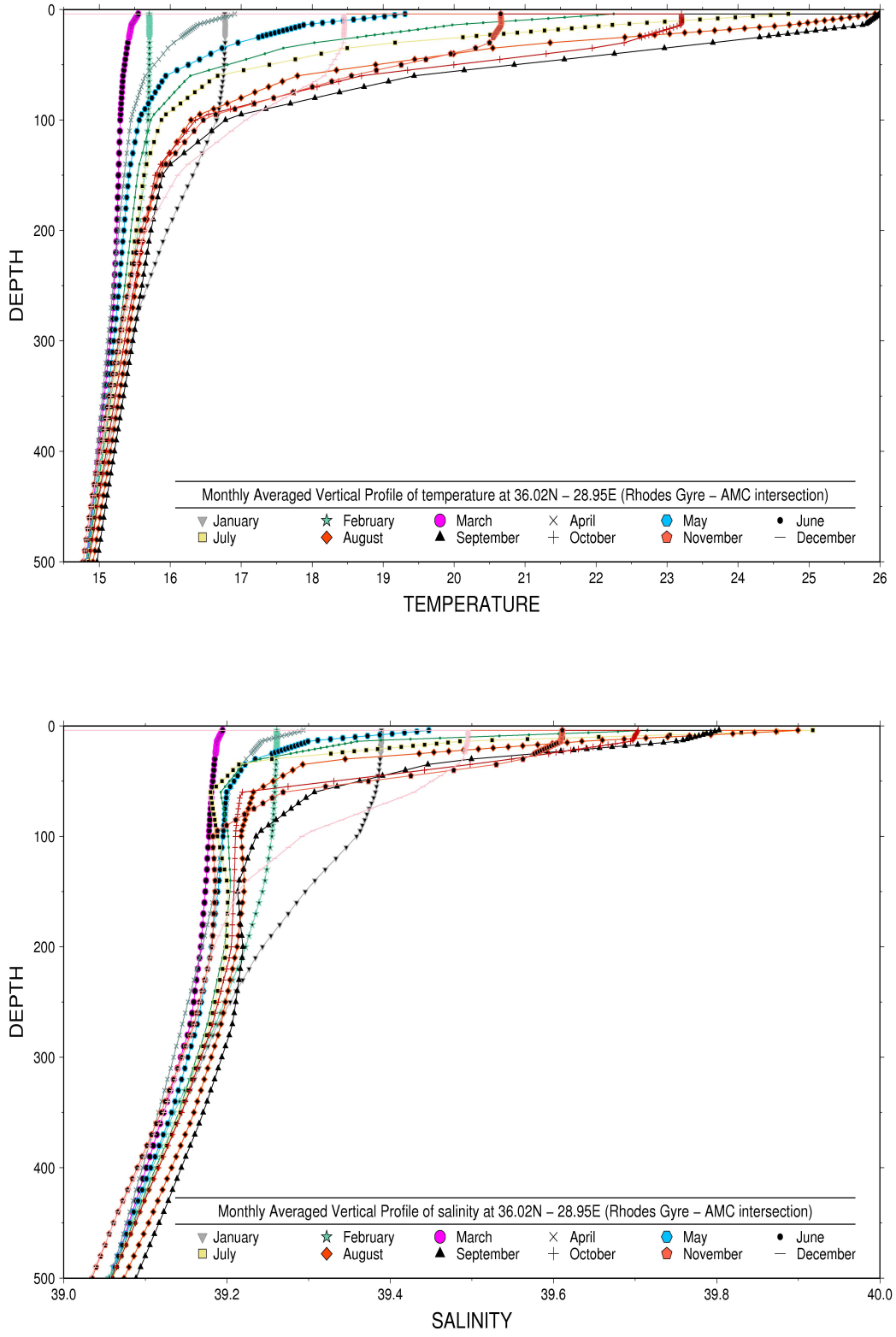

FIGURE 4.12: *Monthly averaged vertical profile of temperature and salinity for 36.02N - 28.95E in Rhodes Gyre over years 1996 - 2000*

4.3 Thermohaline Structure

Some features related to thermohaline structure of the Northern Levantine have already been shown while demonstrating vertical mixing in Section 4.2. However, quantitative information on physical traces and their temporal and spatial distributions are rarely discussed so far. In this section, temperature and salinity distributions of model outputs will be introduced. Discussions of surface temperature will be continued while validating model results (Section 4.4.1).

Monthly vertical distributions of temperature can be reviewed from Fig. 4.8 - 4.11.

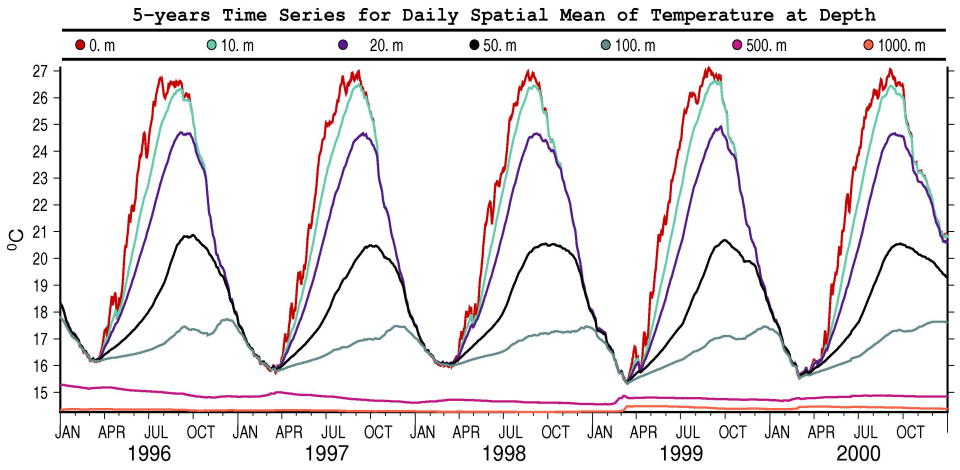

FIGURE 4.13: *Daily spatial MAXIMUM MINIMUM and MEAN of temperature between 1996 and 2000 at depths 0m, 10m, 20m, 50m, 100m, 500m, 1000m*

Temperature of the study area ranges between 6 °C to 30 °C at the surface where minimum occurs in estuarines (also see Fig. 4.17). Until 100 *m* depth, there are variations in daily temperature and thereafter it is stabilized. Surface temperature sinks down to 100 *m* depth in January when vertical mixing occurs. However, a highly stratified water column is generated in summer months with strong heat influx. Range of temperature at 100 *m* is from 15.4 °C to 23 °C. Mean of temperature ranges between 16 °C and 27 °C in the first 100 *m* (Figure 4.13).

Vertical temperature profile of the selected 36.02N - 28.95E grid point at the periphery of the Rhodes Gyre (Figure 4.12) also indicates a unified water column in February and March with a 15 °C - 15.5 °C temperature and a stratified structure after April reaching temperature of range 15 °C - 26 °C in September. Temperature obviously stays under average values since the selected point is an upwelling region under the influence of intermediate and deep waters.

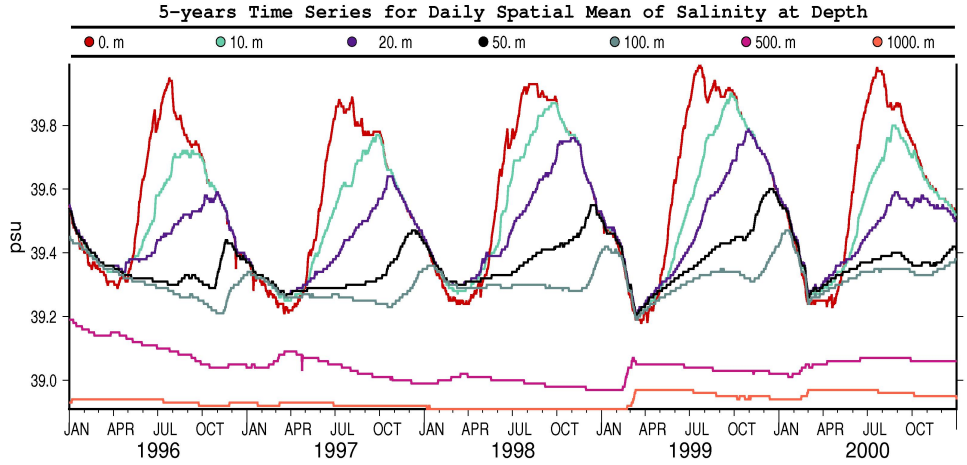

FIGURE 4.14: *Daily spatial MEAN MAXIMUM and MINIMUM of salinity between 1996 and 2000 at depths 0m, 10m, 20m, 50m, 100m, 500m, 1000m*

Modeled salinity of the basin changes between 32 psu at minimum and 42 psu at maximum. However, maximum of spatial average of salinity does not exceed 40 psu and minimum does not drop under 39.3 psu until 100 *m* depth. Salinity distribution is more complex than it is for temperature but short term variations in salinity is lower. Less saline water structures stay at depths which are closer to bottom. Although small daily variability can be observed at 500 *m*, salinity is almost stable at 1000 *m* (Figure 4.14).

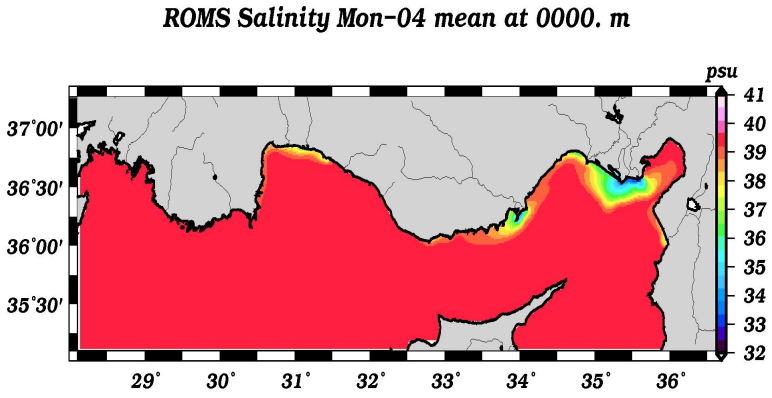

FIGURE 4.15: *Monthly averaged salinity at the surface between 1996-2000 in April*

Vertical salinity profile of the selected 36.02N - 28.95E grid point (Figure 4.12) offers that all water column in March has salinity of 39.15 psu. With increasing evaporation, surface waters become more saline in summer months and exceeds 39.8 psu in July and August. A halocline is formed in September with a salinity of 39.65 psu at 15 *m* and disappers in December.

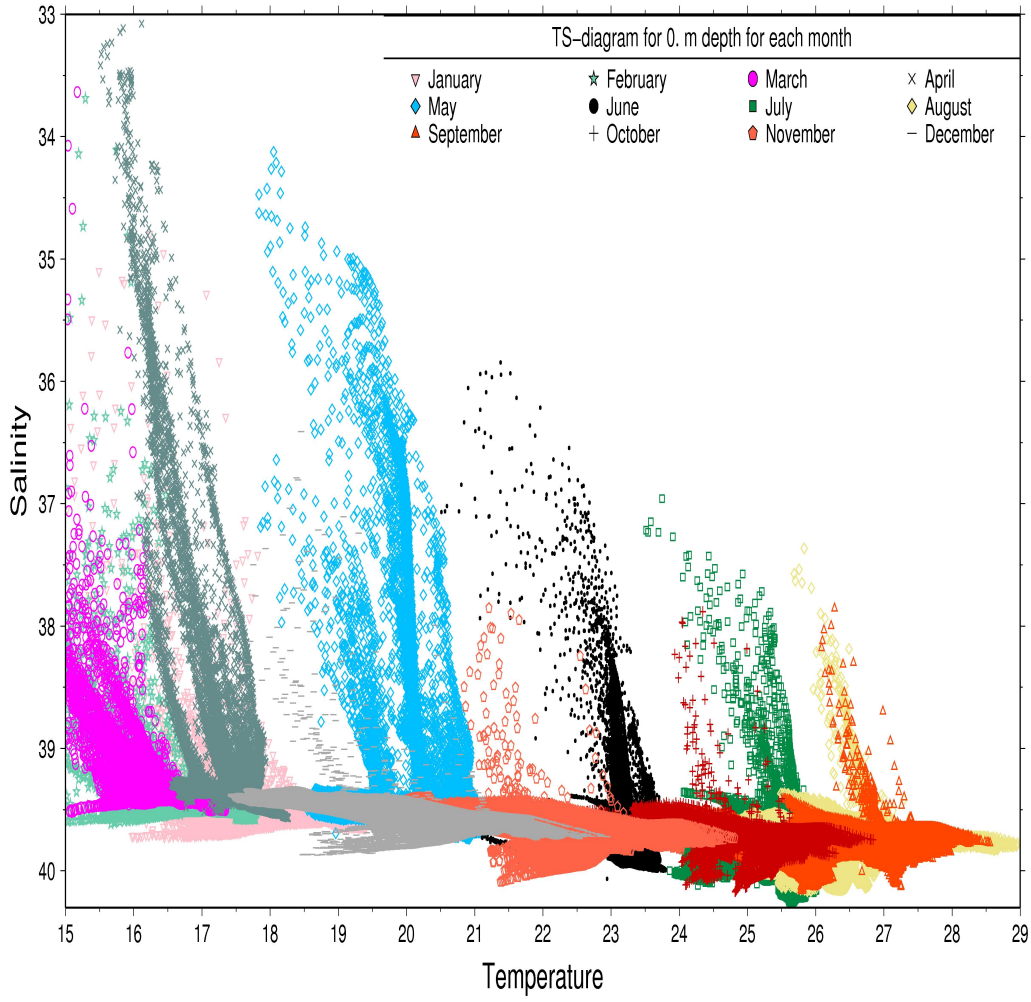

FIGURE 4.16: *TS-diagram of monthly averaged temperature and salinity at the surface for each month*

Figure 4.16 shows TS-diagram of surface distribution for each month. Besides changes in salinity and temperature due to seasonality, water structures stay at regions of river inputs and

periods of increasing evaporation can be distinguised easily. Salinity accumulation between 39 psu and 40 psu is violated in spring months with an increase in less saline river discharges from different sources. April and May are two months that rivers impact on sea water is highest. Temperature in river mouths does not seem to be changed in mentioned periods so much since gradient between SST and river water temperature is low. With increasing temperature, effect of evaporation in summer months leads to highly saline surface water and river domination in coastal sea is almost annihilated, especially in August and September. Radius of rivers can be best traced by surface salinity distibutions as shown in Fig. 4.15. The coastal arc between Bay of Mersin and Gulf of Iskenderun is the most effected area of Northern Levantine by rivers.

One last remark on the thermohaline structure is about the signal in LDW around 500 *m* and 1000 *m* appears in both temperature and salinity timeseries. Strong signal of water structure change is detected just before the beginning of spring in 1999. Although averages do not tell much about the source, harsh vertical mixing may result in such water transportations due to downwelling along the basin. Another explanation can be a flooding of more saline and warmer water from the boundary. The same signal will also be tracked in ecosystem variables (Section 4.5).

4.4 Validation

In this section, model result will be validated with available satellite data. Monthly averages of sea surface temperature (SST), sea level anomaly (SLA) and surface chlorophyll distributions are prepared for comparison.

SST is validated by regionally matching AVHRR-Pathfinder data of PO.DAAC (Physical Oceanography Distributed Active Archive Center of NASA). Data used has 4 *km* resolution. Monthly averaged version of Pathfinder dataset is downloaded for whole Mediterranean. Study area is extracted using NetCDF operators. Therefore, methods to average satellite SST and model SST may differ which may effect the reliability of comparison. Eventually, results will be presented and discussed in section 4.4.1.

For SLA validation, monthly averaged AVISO climatologies are selected. Data is relatively coarse since it is prepared for Mediterranean Sea and Northern Levantine Basin occupies a small number of grid points. Section 4.4.2 is devoted to presentation of SLA results.

The only available satellite data for surface chlorophyll for model runtime is SEAWIFS between September of 1997 and December of 2000. Daily Level 2 SEAWIFS data is averaged monthly along model domain (Section 4.4.3). SEADAS software is used to prepare SEAWIFS dataset. Obviously, interested data is poor quality and will not be sufficient for validate the model surface chlorophyll. However, it is good enough to give an idea about model outcomes.

4.4.1 Sea Surface Temperature (SST)

Comparison of model SST results with AVHRR data shows that there is good compatibility between them in some months whereas significant differences can also be observed in some others.

In January, despite some quantitative differences, main characteristics of surface temperature are reflected. Similarities for SST along eastern boundary and Anatolian coast are promising in January. Furthermore, patterns around Rhodes Gyre are satisfactory. In February and March, there observed a difference of nearly 1 °C in the whole basin except Rhodes Gyre and east of Cyprus. Effects of river along Bay of Mersin are distinguishes model results in these two months from satellite data which is not able to resolve them. In April, again except for regions under the impact of rivers, good coordinance is observed between two data sets (Figure 4.17).

In May, with the increasing heat flux, significant differences occur in the eastern part of the basin, especially in Gulf of Iskenderun (Figure 4.18). These differences spread basin-wide except Rhodes Gyre and its periphery in following stratification season. However, model SST tends to recover again and resembles satellite image especially in coastal regions and Rhodes Gyre after August. The challenge in September and thereafter seems to be the spreading of coastal waters off the shore. Rhodes Gyre compensate this discrepancy with its own dynamics but other parts of the basin are dominated by Asia Minor Current which prevents inshore warm water to flow offshore (Figure 4.19).

Difficulty in heating of the sea surface during summer is tested and found to be a consequence of the inadequate setup of longwave radiation which will be discussed in section 4.7.

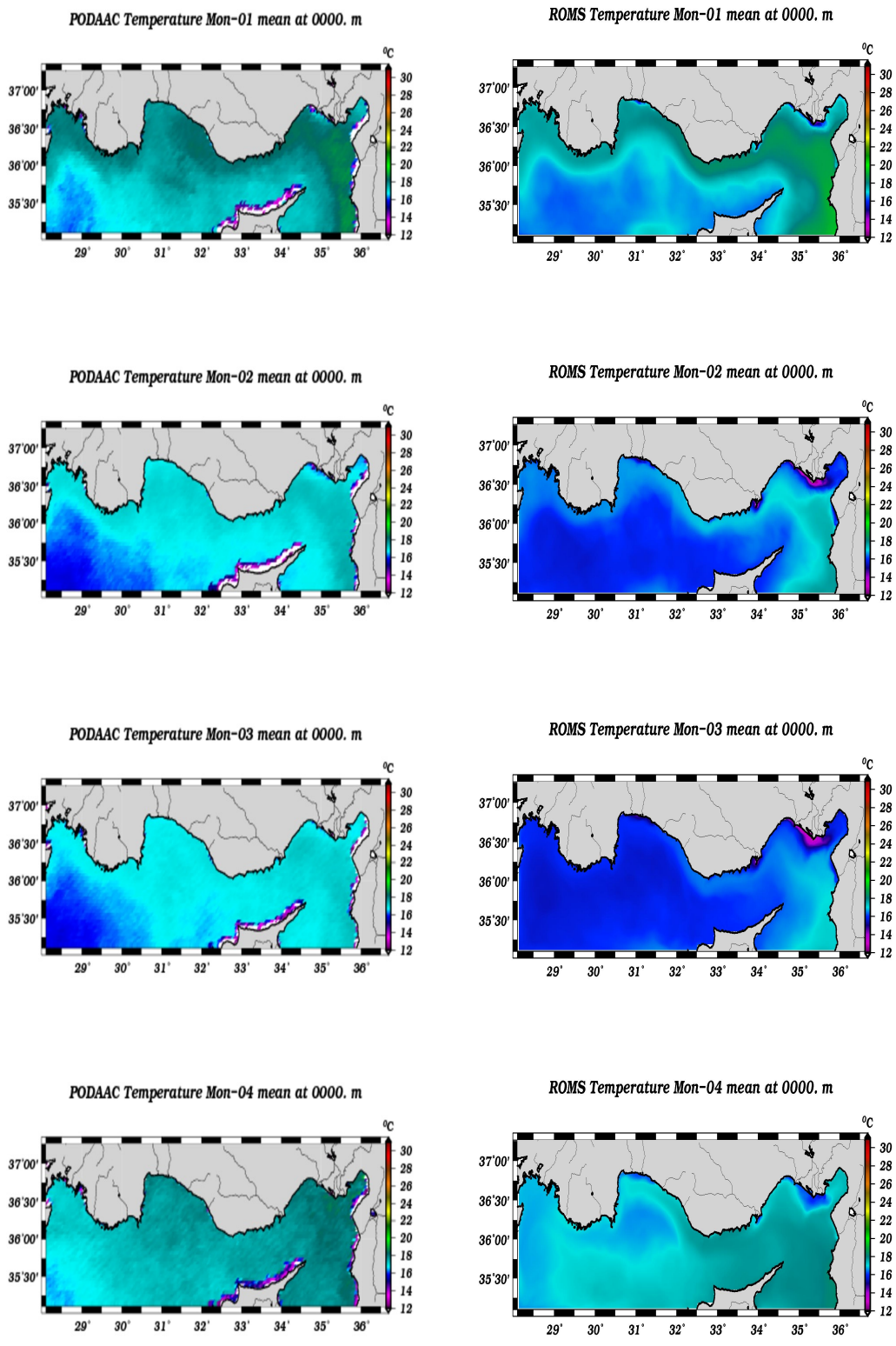

FIGURE 4.17: *Comparison of monthly averaged SST of PODAAC satellite and ROMS between 1996-2000 in January, February, March and April*

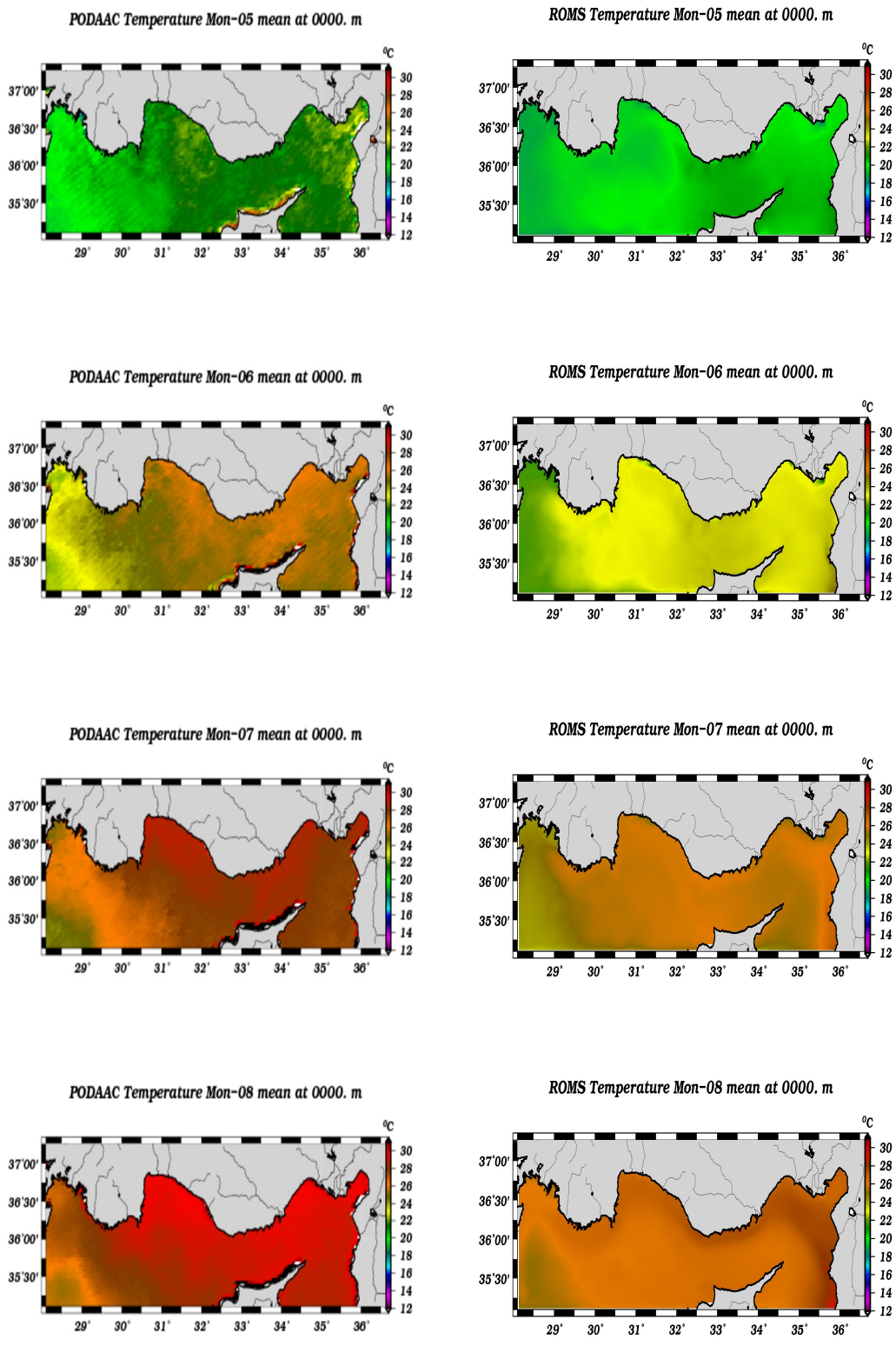

FIGURE 4.18: *Comparison of monthly averaged SST of PODAAC satellite and ROMS between 1996-2000 in May, June, July, August*

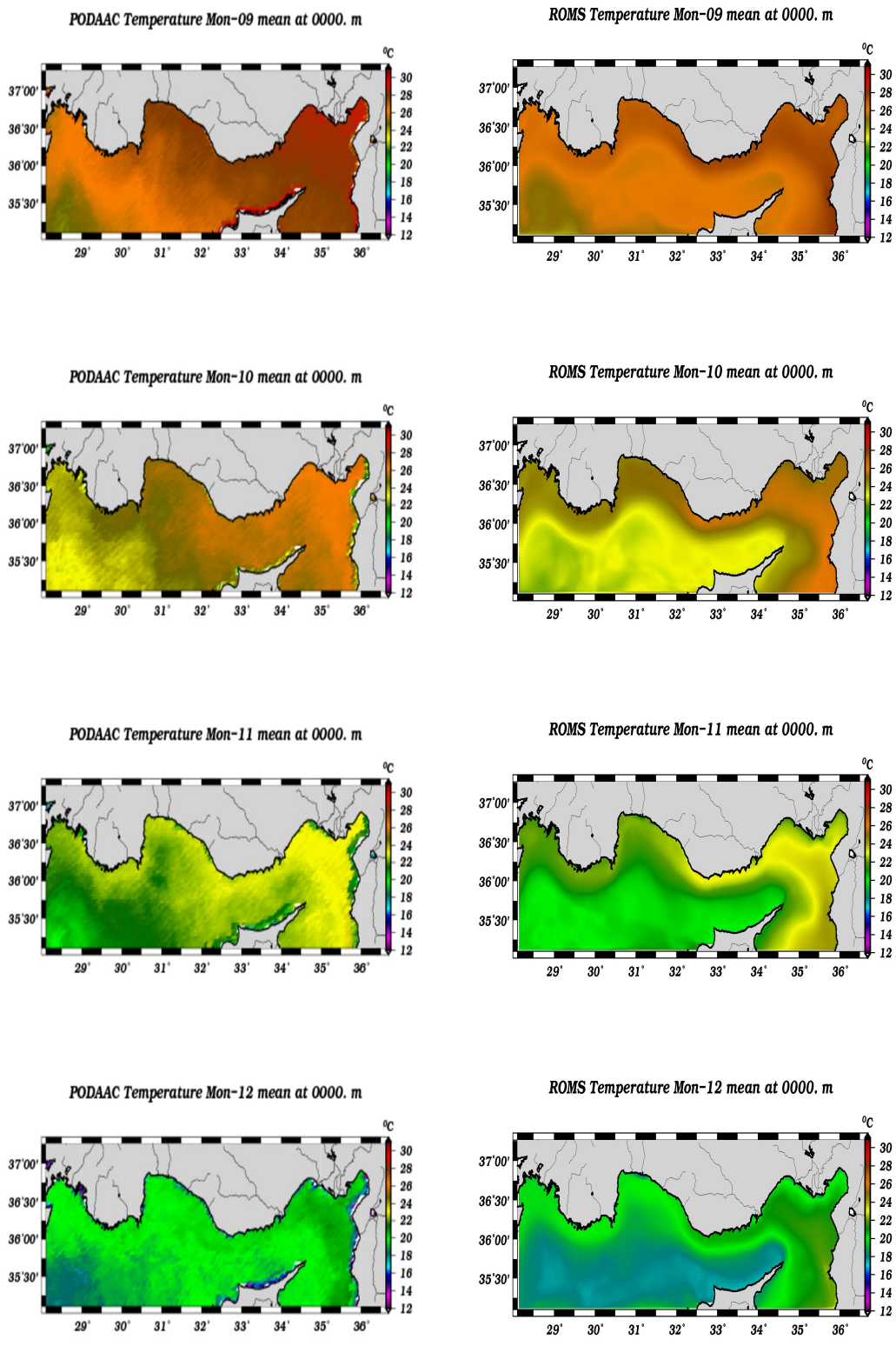

FIGURE 4.19: *Comparison of monthly averaged SST of PODAAC satellite and ROMS between 1996-2000 in September, October, November, December*

4.4.2 Sea Level Anomaly (SLA)

According to the timeseries plots in Fig. 4.20, sea surface height (SSH) in the model domain changes between -0.85 *m* of minimum and -0.15 *m* of maximum. Average height oscillates between -0.8 *m* and -0.3 *m* where minima and maxima occur at the end of 1999 and at the beginning of 2000, respectively. Besides timeseries do not indicate any periodicity, deviations which occur around the minima and maxima are also remarkable. Quantitatively, sea level anomaly (SLA) is computed between -9 *cm* and 15 *cm*. These limits are consistent with literature findings cited in *Alhammoud et al. (2005)*. They quoted different ranges for SLA where maximum difference is calculated as 27 *cm* between -12 *cm* and 15 *cm* for Levantine (*Larnicol et al., 2002*).

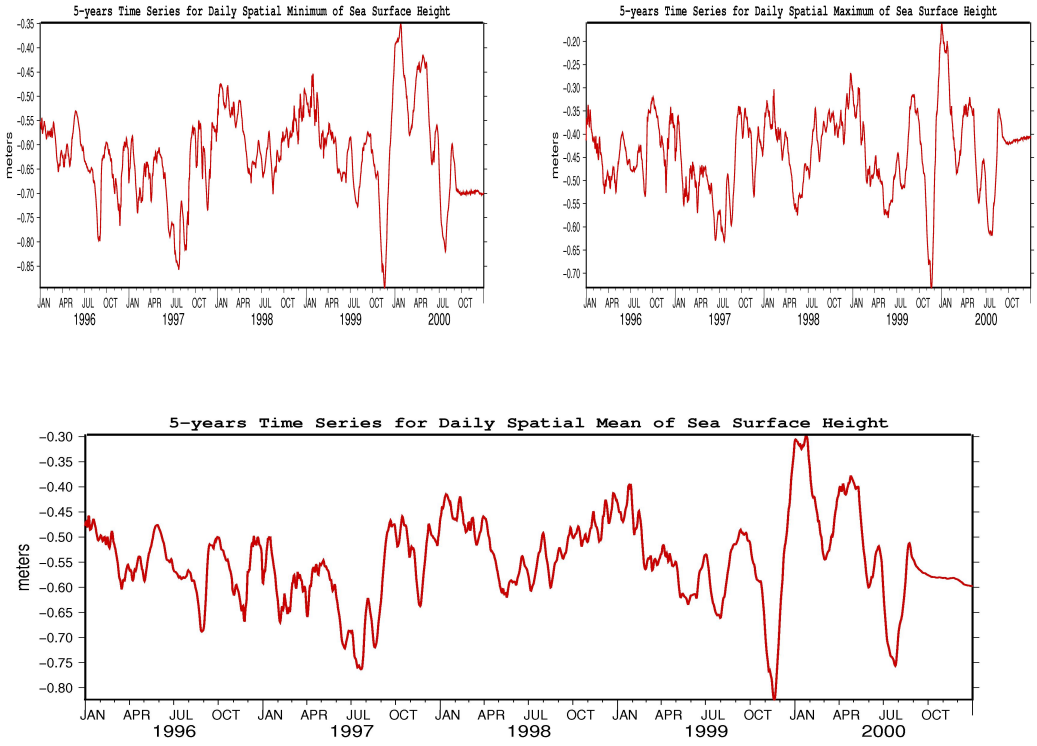

FIGURE 4.20: *Daily spatial MAXIMUM MINIMUM and MEAN of sea surface height between 1996 and 2000*

AVISO SLA data, as mentioned at the beginning of section, extracted from Mediterranean dataset and interpolated from a small number of grid points. This may be a reason why comparison may not be helpful to get a correct view about behaviour of sea level. On the other hand, model results strictly tied to bathymetric properties of basin and hydrodynamical

features such as AMC and Rhodes Gyre. Being an upwelling region, Rhodes Gyre and its periphery satisfies lower sea level due to geostrophic balance compared to circumscribing area in model outputs. AMC apperantly dissociate coastal regions from offshore strictly (see Fig. 4.21- 4.23).

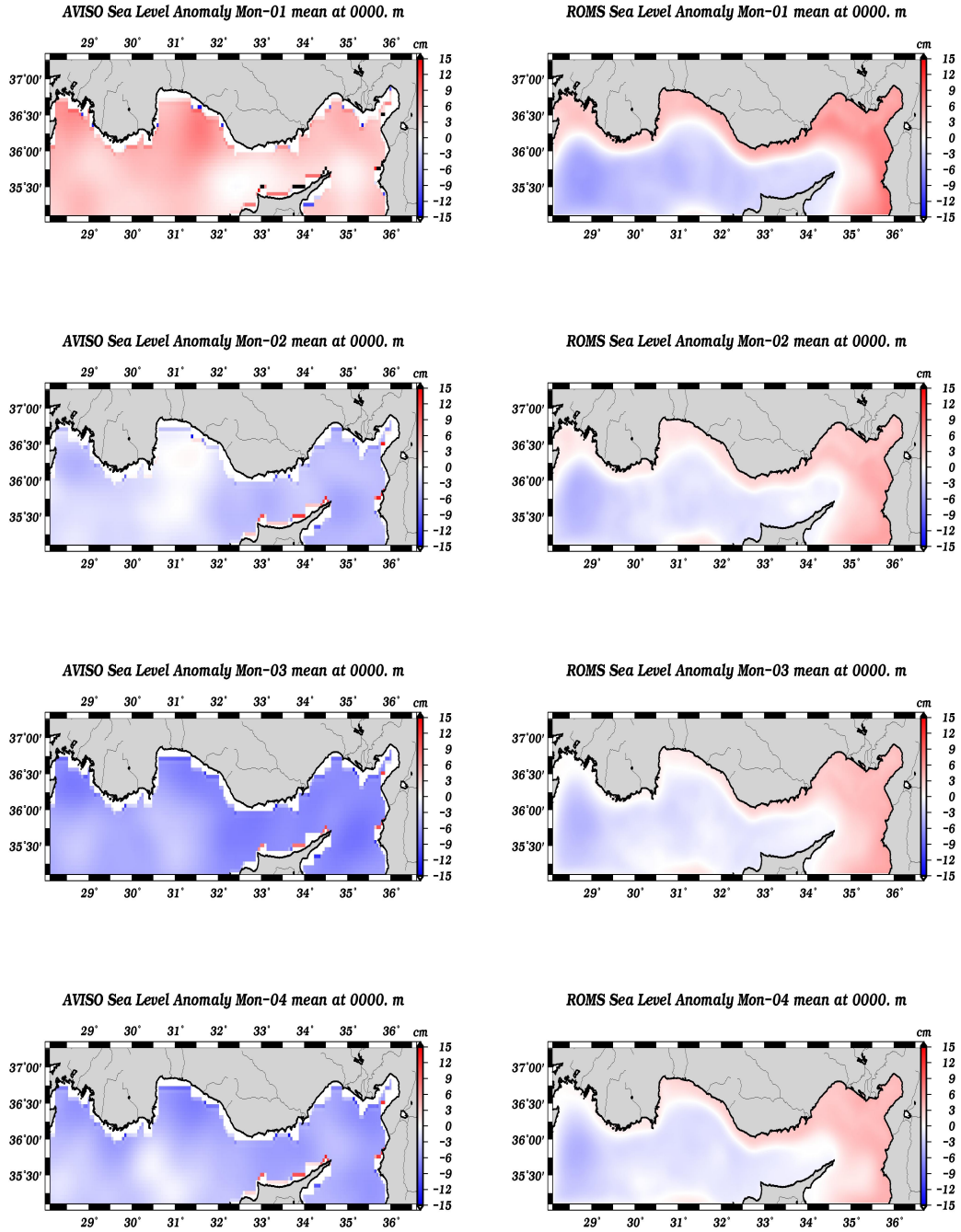

FIGURE 4.21: *Comparison of monthly averaged SLA of Aviso satellite and ROMS between 1996-2000 in January, February, March and April*

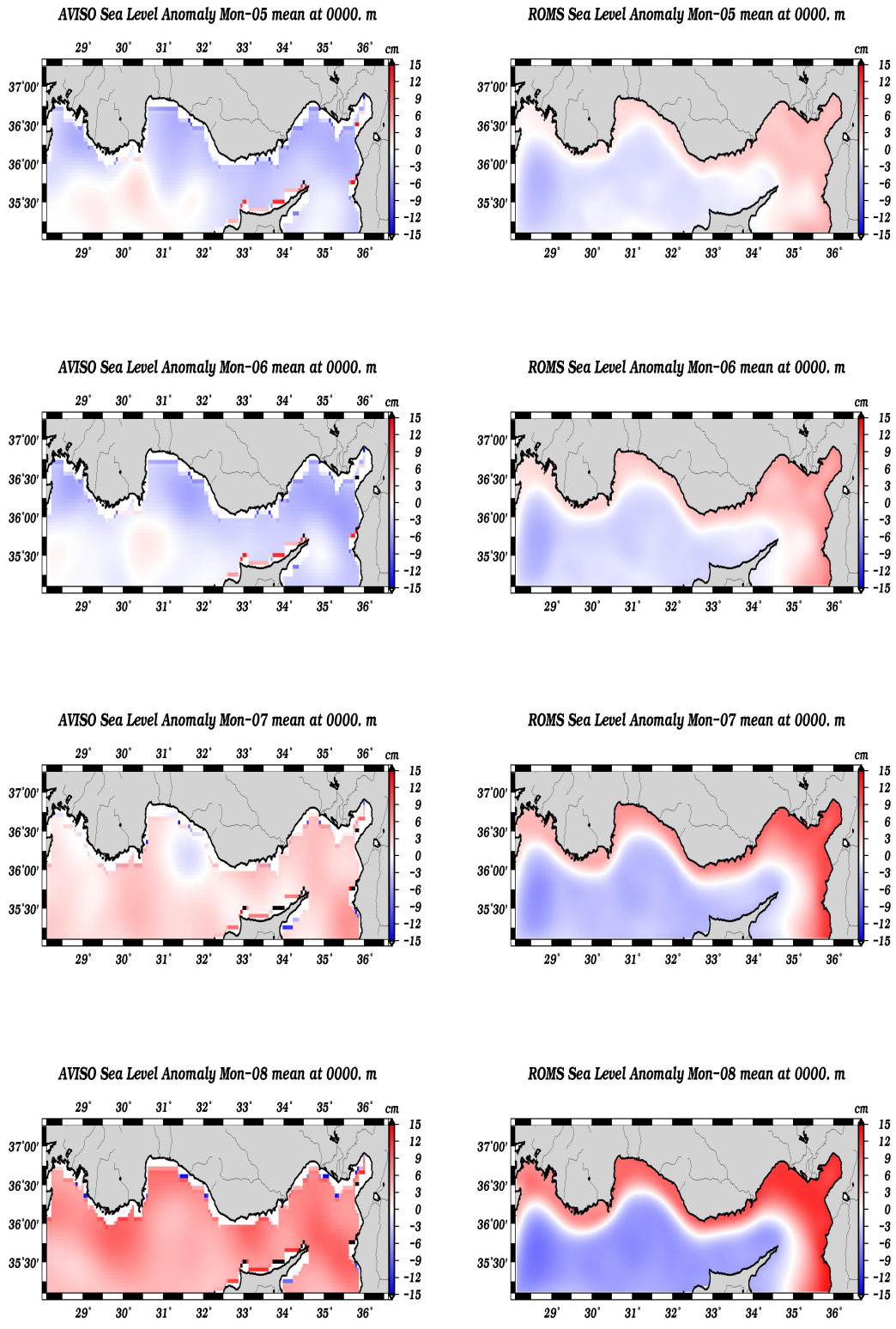

FIGURE 4.22: *Comparison of monthly averaged SLA of Aviso satellite and ROMS between 1996-2000 in May, June, July, August*

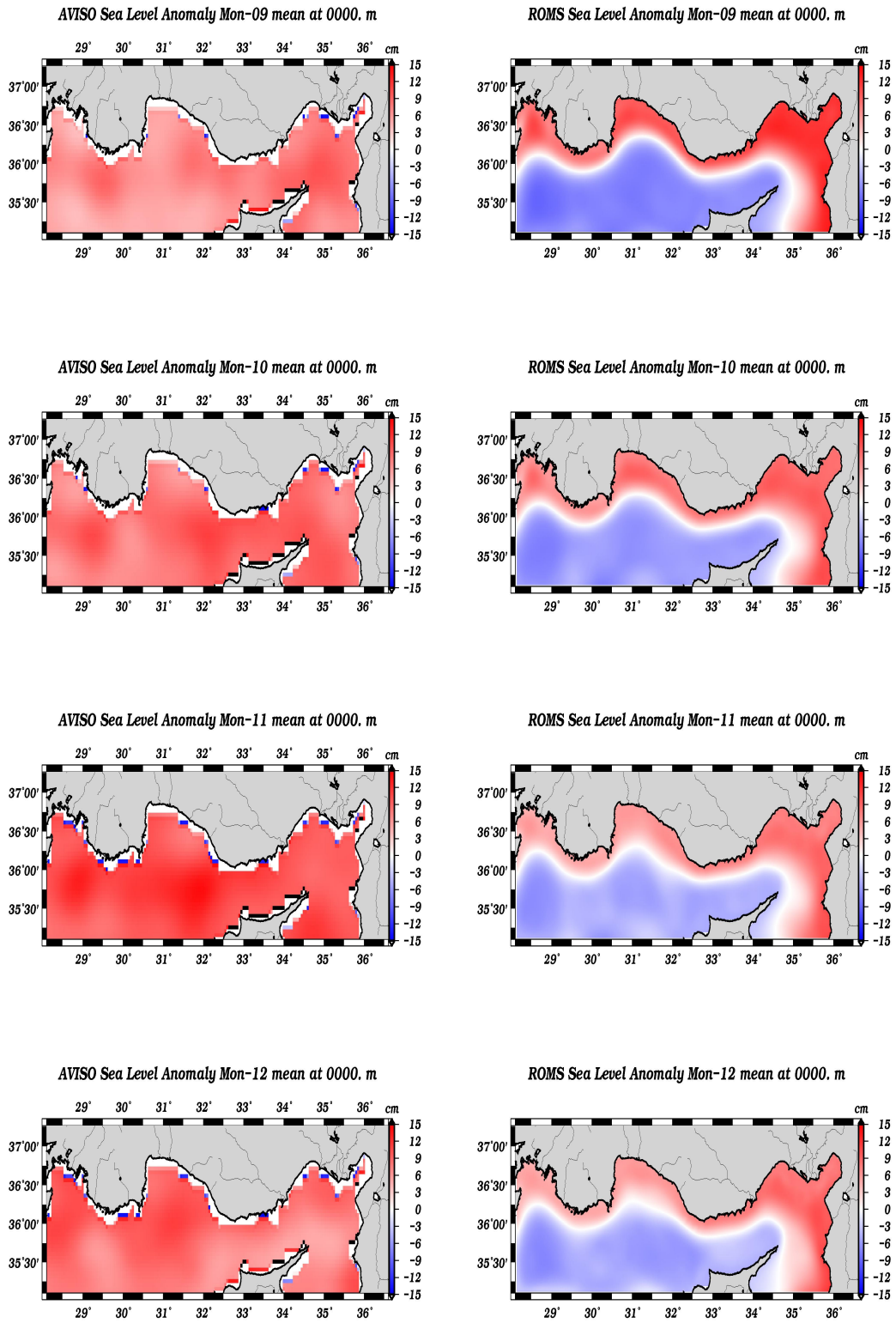

FIGURE 4.23: *Comparison of monthly averaged SLA of Aviso satellite and ROMS between 1996-2000 in September, October, November, December*

4.4.3 Sea Surface Chlorophyll

Sea surface chlorophyll distributions are validated by the monthly averaged SEAWIFS satellite data. Eventhough, the data have relatively poor quality, particularly in coastal regions, it has been utilized as reference point for model outputs.

Overall comparison of model results with SEAWIFS satellite data proposes an overestimation of chlorophyll concentration at the surface. Influence of water inflow through the channel between Latakia and Cilician Basins dominates coastal areas in accordance with strength of AMC.

However, early winter and late winter bloom periods are simulated correctly. Furthermore, in particular months, such as May, June and July, effects of the rivers in estuarines of Mersin Bay and Gulf of Antalya reflects the same patterns in both model and satellite imageries with respect to the whole basin. In addition, model captures well-known cyclonic vs. anti-cyclonic region antagonism on behalf of Rhodes Gyre and West Cyprus eddy, where former region is richer in chlorophyll concentration as a result of being an upwelling area.

Vertical distributions and timeseries of chlorophyll results will be presented in section 4.5.

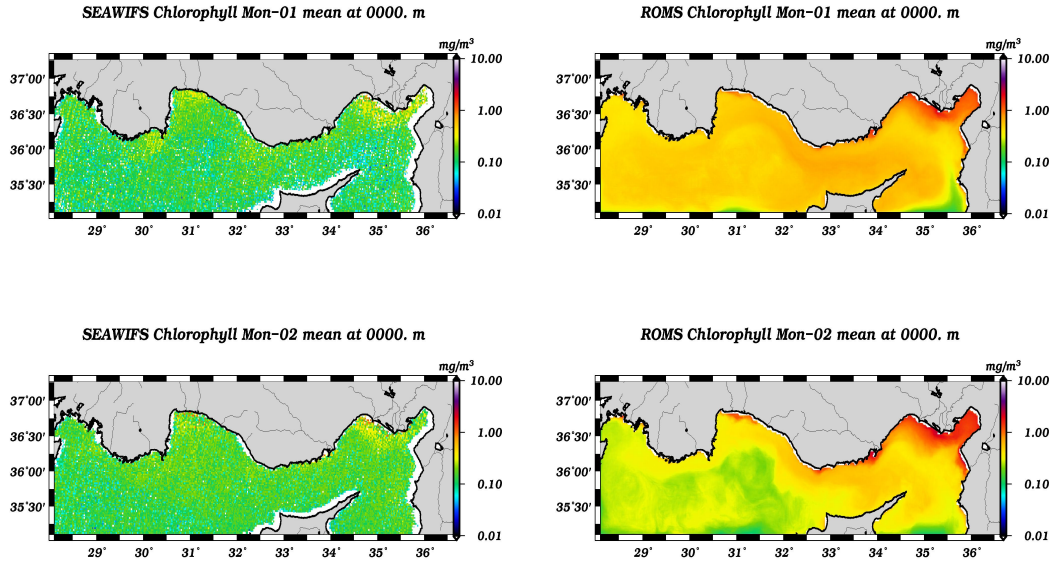

FIGURE 4.24: *Comparison of monthly averaged chlorophyll of SEAWIFS satellite and ROMS between 1996-2000 in January, February*

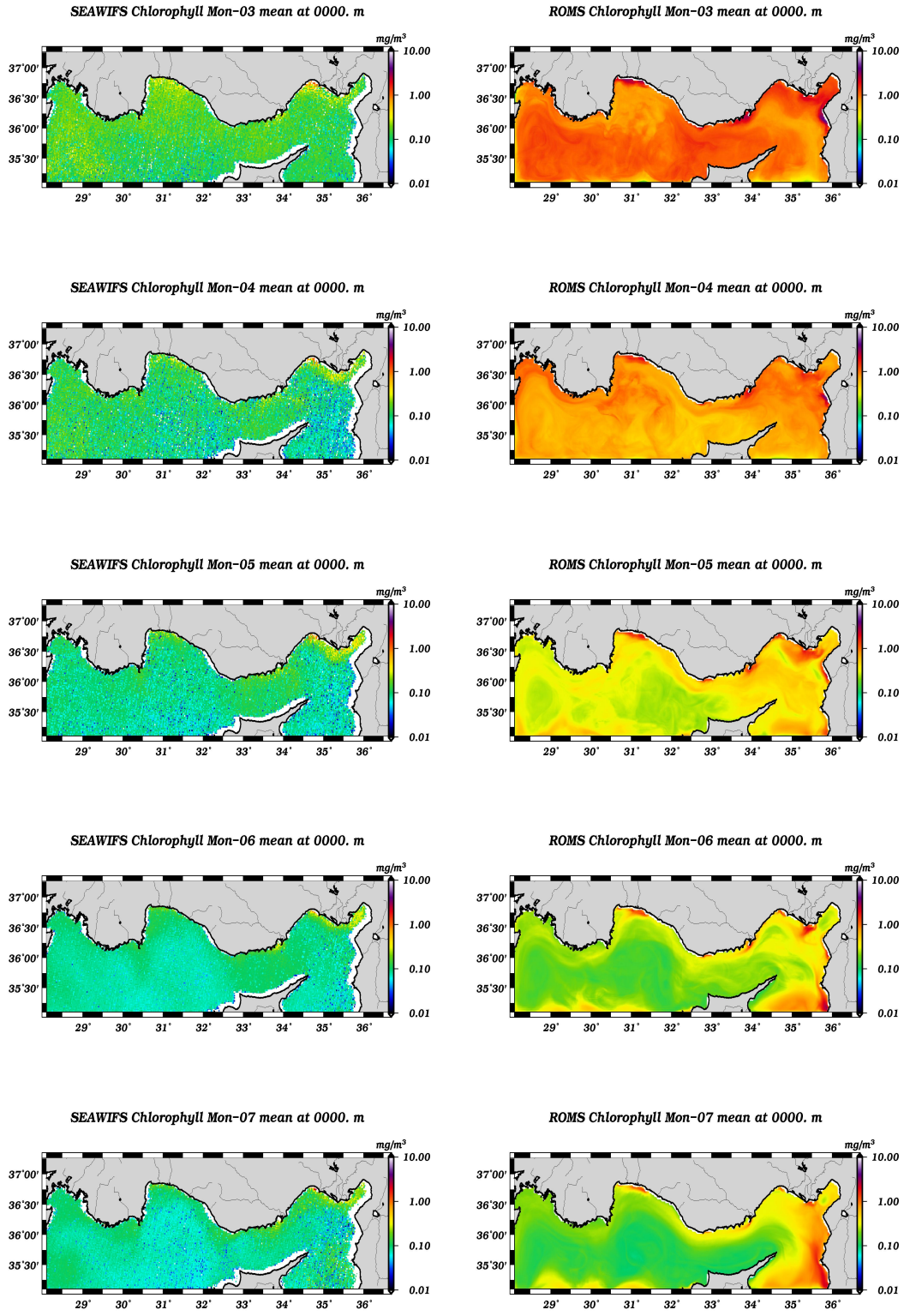

FIGURE 4.25: *Comparison of monthly averaged chlorophyll of SEAWIFS satellite and ROMS between 1996-2000 in March, April, May, June, July*

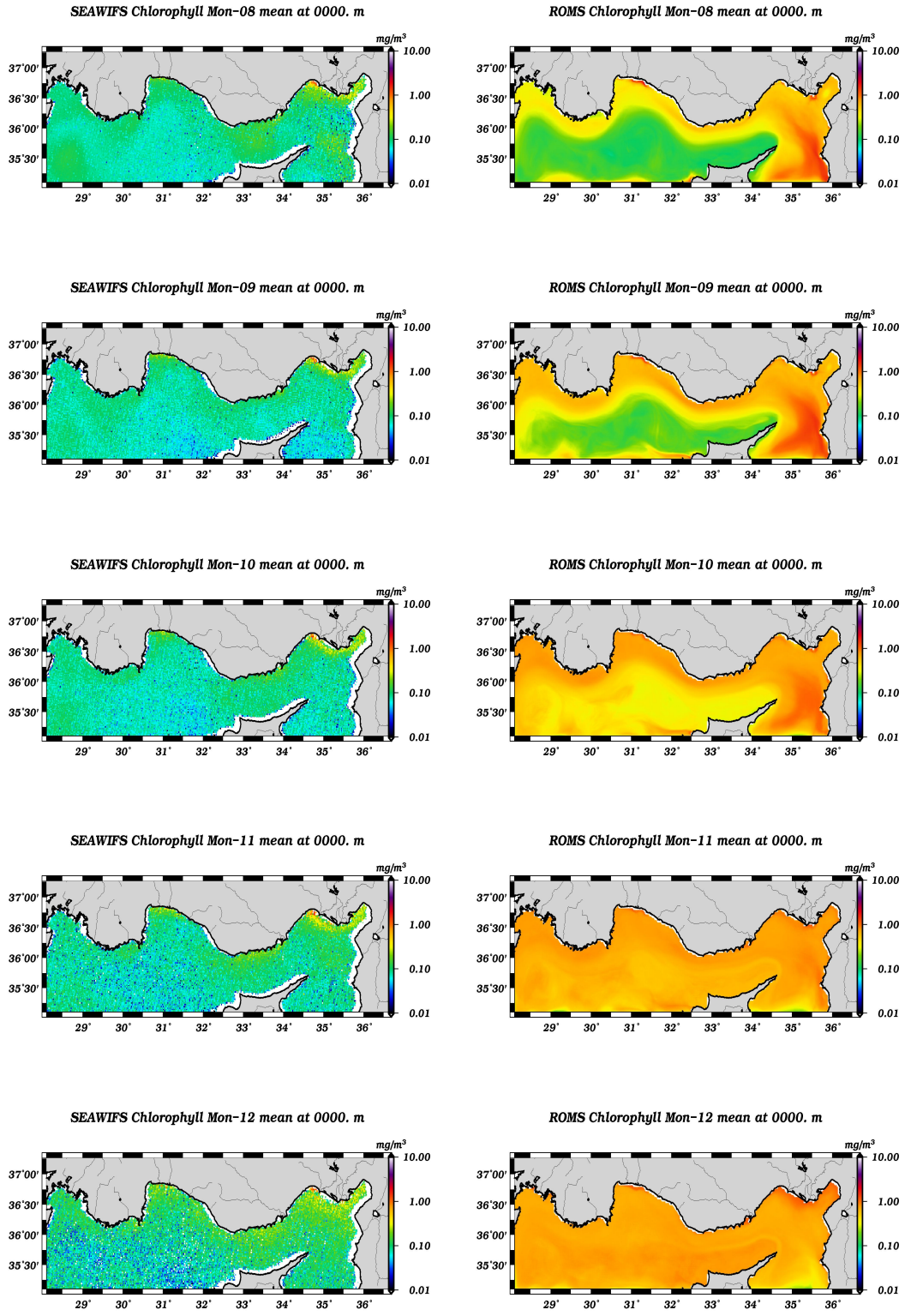

FIGURE 4.26: *Comparison of monthly averaged chlorophyll of SEAWIFS satellite and ROMS between 1996-2000 in August, September, October, November, December*

4.5 Ecosystem

As expressed in section 4.4.3, chlorophyll concentration at the surface is overestimated by the model. The same conclusion can obviously be deduced from Fig. 4.27. Signals of high concentration of chlorophyll during bloom periods are strong and reaches 100 m depth. Daily spatial average values generally ranges between 0.8 $mg\ m^{-3}$ and 3.0 $mg\ m^{-3}$. Peak value is calculated around 10.0 $mg\ m^{-3}$ during blooms which is very high for regional characteristics. The spatio-temporal average is calculated as 0.48 $mg\ m^{-3}$ for surface chlorophyll and the basin average is 0.18 $mg\ m^{-3}$ (Table 4.1).

A deep chlorophyll maximum exiths during most of the year around 40 - 50 m depths except between December and March (Fig. 4.28). However, since December, January and February are strong vertical mixing periods due to winter conditions, vertical distibution is expected to be unified along the water column during these months. The main characteristics of the Rhodes region is well-captured (Fig. 4.28) by the model. The maximum value does not exceed 1 $mg\ m^{-3}$ even in March.

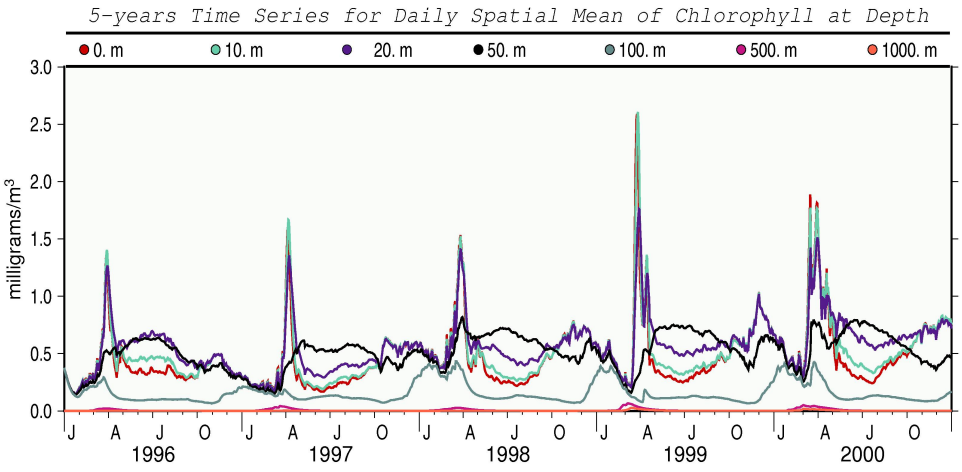

FIGURE 4.27: *Time series for daily spatial MEAN of chlorophyll between 1996 and 2000 at depths 0m, 10m, 20m, 50m, 100m, 500m, 1000m*

Eker-Develi et al. (2006) proposed an average value of 15 $\mu g\ l^{-1}$ for phytoplankton biomass, which is underestimated by the model. However, their study area is narrower and includes the relatively productive estuarine, Bay of Mersin, which may increase averages. Phytoplankton signals of the region resembles those for chlorophyll. A sharp peak appears following winter mixing in March and April. Then biomass is almost fixed in all layers (Fig. 4.29)

during stratification seasons. Upto 20 m beneath the surface, phytoplankton biomass is around 0.4 $mm\ N\ m^{-3}$ ($\sim 5.6\ mg\ m^{-3}$). Spatio-temporal averages are even smaller. The surface average is calculated to be 0.32 $mm\ N\ m^{-3}$ ($\sim 4.5\ mg\ m^{-3}$) and the basin average is less than 0.1 $mm\ N\ m^{-3}$ (Table 4.1).

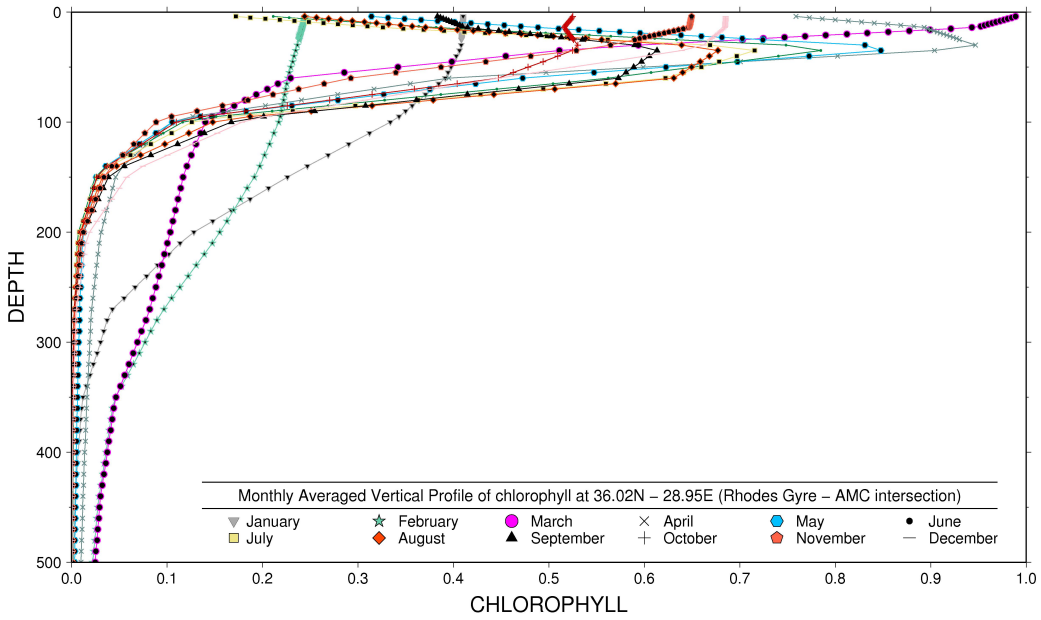

FIGURE 4.28: *Monthly averaged vertical profile of chlorophyll for 36.02N - 28.95E grid point in Rhodes Gyre over years 1996 - 2000*

Spatial averages of zooplankton notice that in terms of population, abundance is restricted only in the first 50 m and after 100 m biomass converges to zero (Fig. 4.30). Maximum of average biomass oscillates between 0.3 $mm\ N\ m^{-3}$ and 0.75 $mm\ N\ m^{-3}$ in subsurface layers and rarely exceeds 0.1 $mm\ N\ m^{-3}$ in 50 m. There is a dramatic decrease of population during the winter mixing period even in subsurface levels. Biomass approaches a minimum threshold values rapidly but community recovers suddenly after chlorophyll and phytoplankton blooms which increase production.

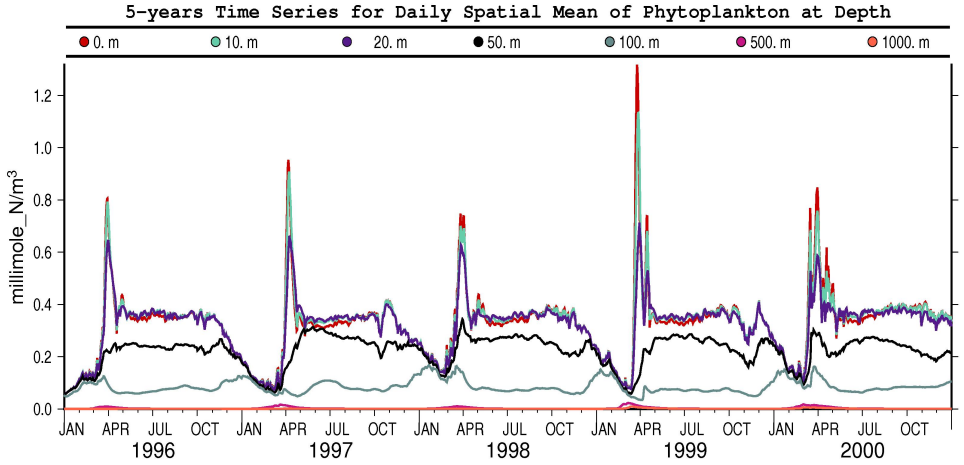

FIGURE 4.29: *Time series for daily spatial MEAN of phytoplankton between 1996 and 2000 at depths 0m, 10m, 20m, 50m, 100m, 500m, 1000m*

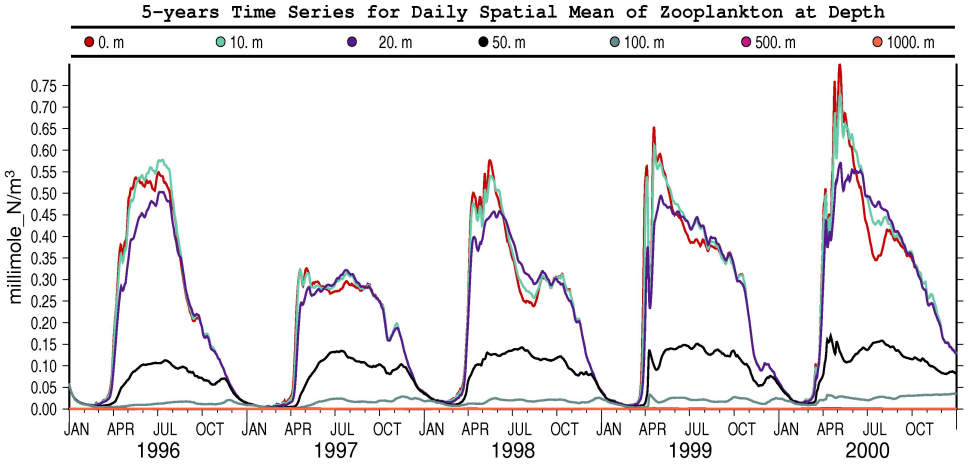

FIGURE 4.30: *Time series for daily spatial MEAN of zooplankton between 1996 and 2000 at depths 0m, 10m, 20m, 50m, 100m, 500m, 1000m*

Timeseries of nitrate indicate that standard processes during production are simulated well by the model. During winter mixing, surface nitrate abundance reaches to the levels of the nutrient at 100 *m* depth. Then almost all available nitrate in the euphotic zone is consumed during the spring bloom (Fig. 4.31 upper panel). Nitrate concentration of deep waters is clearly higher. However, a maximum over the basin is located at the surface due to discharges around estuaries (Fig. 4.31 lower panel). The basin average is estimated as 2.07 $mm\ m^{-3}$ and the surface mean drops down to 0.36 $mm\ m^{-3}$ (Table 4.1).

Vertical profile of selected Rhodes Gyre grid point clarifies monthly changes of nitrate upto 1000 m (Fig. 4.32). Surface average values at most reaches to 1.5 $mm\ m^{-3}$ in February. Nutricline appears in the first 30 m in the stratification seasons.

Unlike nitrate, ammonium is accumulated mostly in subsurface levels betwen 20 m and 100 m. On the contrary, there are negligible traces in deep waters. At 50 m, a maximum of spatial average does not exceed 1.4 $mm\ m^{-3}$ which is computed in summer of 1996.

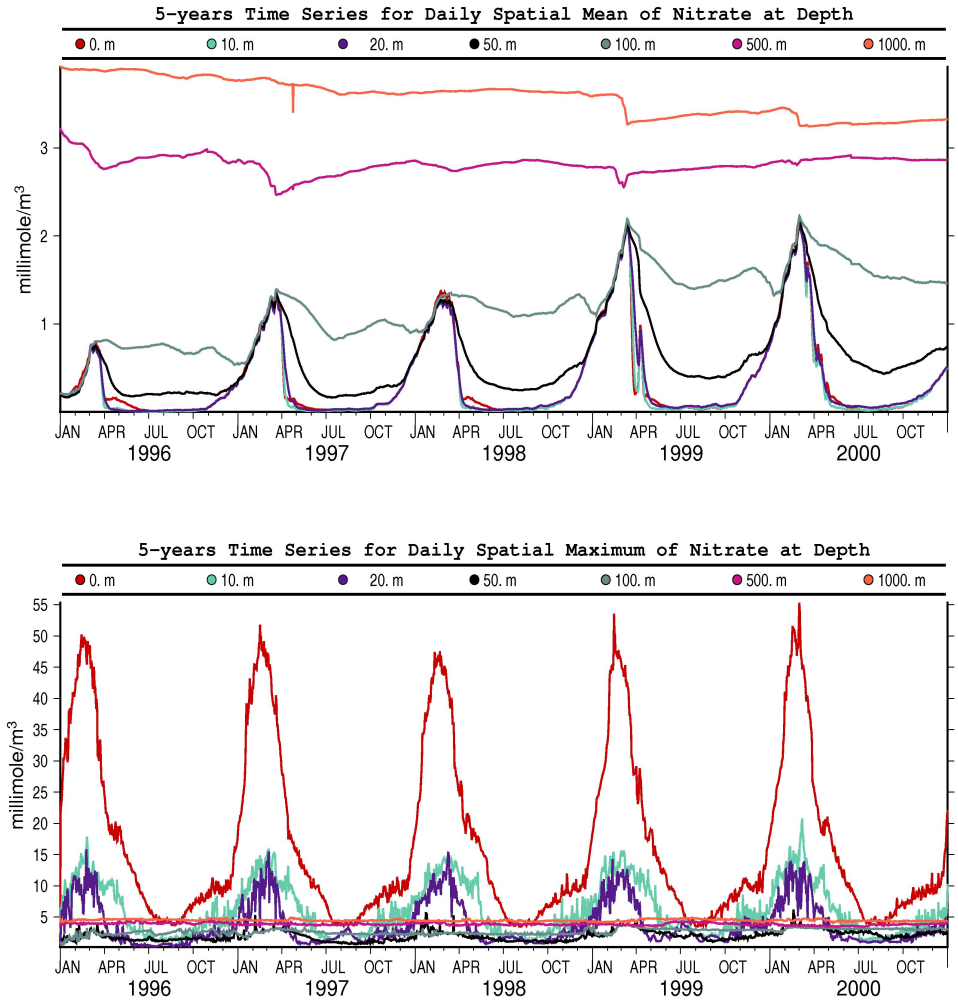

FIGURE 4.31: *Time series for daily spatial MEAN and MAXIMUM of nitrate between 1996 and 2000 at depths 0m, 10m, 20m, 50m, 100m, 500m, 1000m*

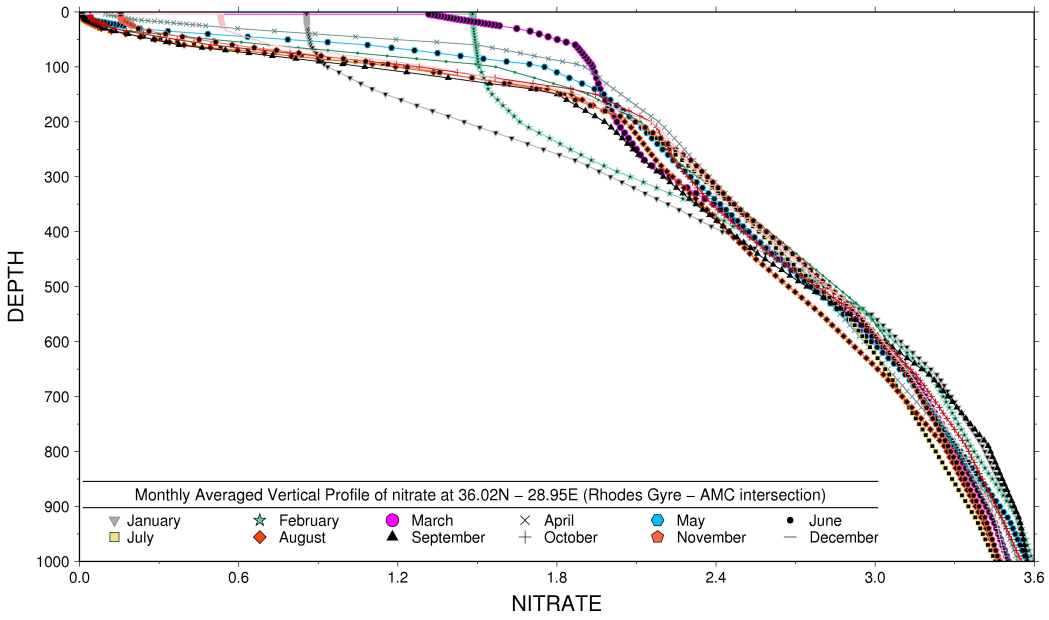

FIGURE 4.32: *Monthly averaged vertical profile of nitrate for 36.02N (AMC) - 28.95E (Rhodes Gyre) over years 1996 - 2000*

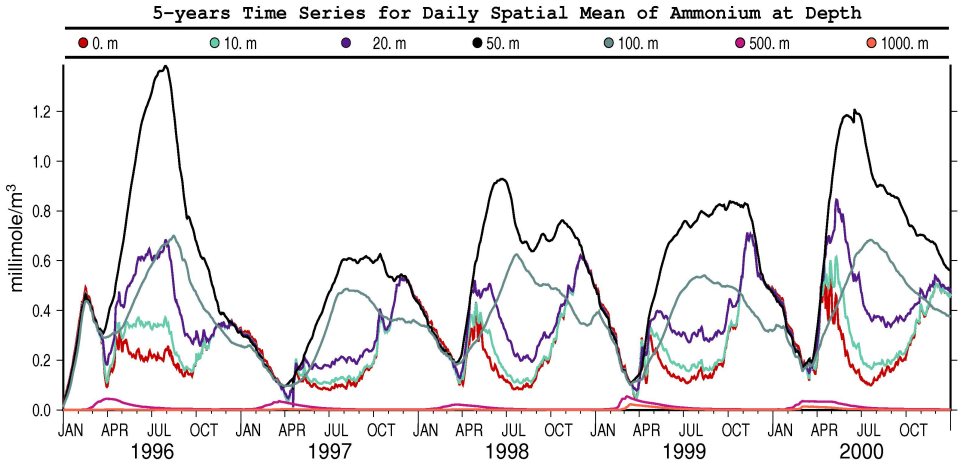

FIGURE 4.33: *Time series for daily spatial MEAN of ammonium between 1996 and 2000 at depths 0m, 10m, 20m, 50m, 100m, 500m, 1000m*

4.6 Comparison of 1996-2000 and 2030-2034 Simulations

Despite being coarse, different climatic conditions lead to remarkable changes for some variables whereas they effect some others only slightly. Changes in river water and nutrient fluxes

due to climate change projections can be seen in Section 3.4. Moreover, comparison of the atmospheric datasets used to force the model from surface can be reviewed in Table 3.3. Their impact on model variables will be presented by using the same method. In other words, surface averages and basin averages are computed along simulation time to calculate deviations between simulations (Table 4.1).

The difference in temperature between 1996-2000 and 2030-2034 for the whole basin is 0.0479 °C. Curves of timeseries for the basin fits well (see Fig. 4.34). However, the effects of global warming seem to be accumulated near surface levels. A considerable increase in SST took place especially during summer months. Eventually, the model estimated a 0.3269 °C increase in surface temperature.

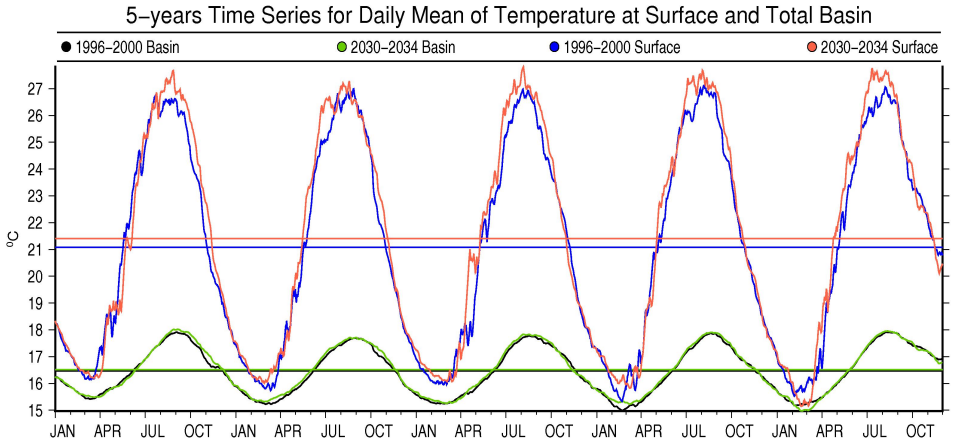

FIGURE 4.34: *Time series for daily spatial surface and basin average of temperature along years 1996-2000 and 2030-2034*

The total basin becomes more saline due to different atmospheric conditions and river inputs used to simulate the 2030-2034 period. Increment in basin average is 0.0032 psu. On the other hand, surface averages shows and increase by 0.0341 psu. Salinity variation of water along the basin can be tracked from Fig. 4.35. Differentiation occurs particularly in spring and summer months. An exception to the general trend is 2034 when there is a sharp decrease observed in salinity.

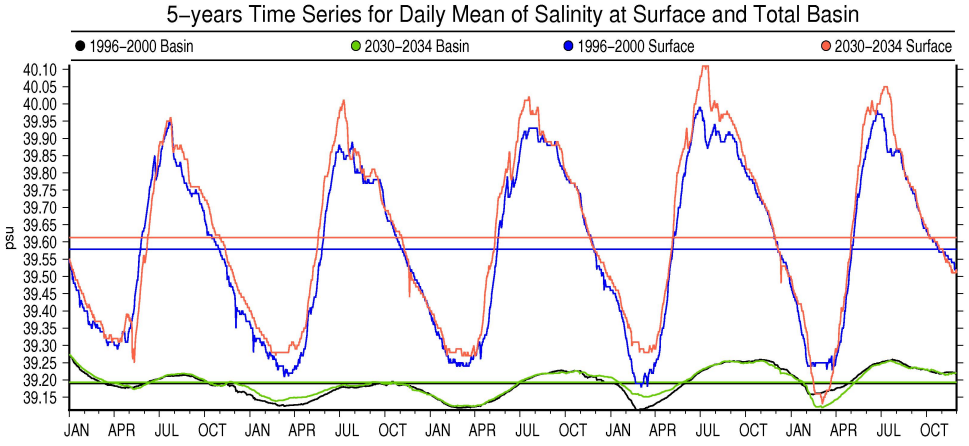

FIGURE 4.35: *Time series for daily spatial surface and basin average of salinity along years 1996-2000 and 2030-2034*

Sea level change seems to be negligible at least for non-local variability. Spatio-temporal mean of sea surface height deviates 1.5 *mm* between two simulations (Fig. 4.36).

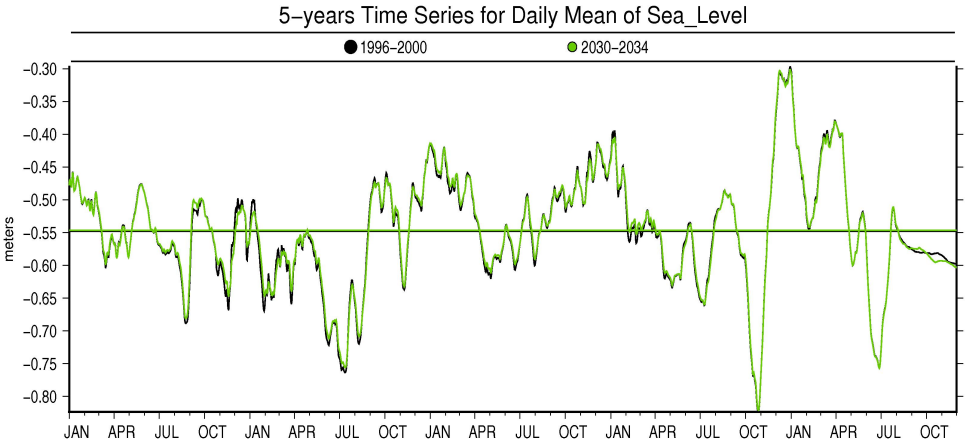

FIGURE 4.36: *Time series for daily spatial surface and basin average of chlorophyll along years 1996-2000 and 2030-2034*

The model predicted a slight increase in average current speed. In addition, signals of dramatic increase and decrease in daily scale overlay in both simulations (Fig. 4.37).

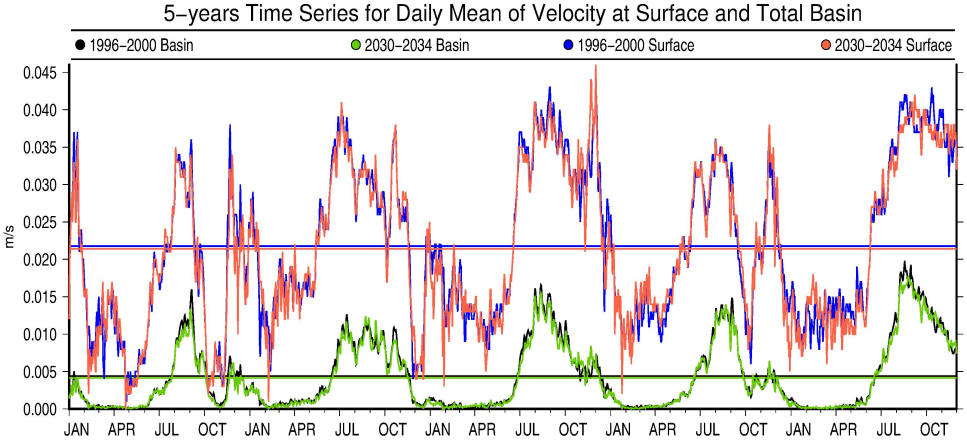

FIGURE 4.37: *Time series for daily spatial surface and basin average of current speed along years 1996-2000 and 2030-2034*

Simulation	Temperature (°C)	Salinity (psu)	Surface Height (m)	Velocity ($m\ s^{-1}$)
	Surface Average			
S1996-2000	21.0814	39.5785	-0.548117	0.0214014
S2030-2034	21.4083	39.6126	-0.546565	0.0217618
Difference	0.3269	0.0341	0.001552	0.0003604
	Total Basin Average			
S1996-2000	16.4624	39.1898	—	0.00412731
S2030-2034	16.5103	39.1930	—	0.00439489
Difference	0.0479	0.0032	—	0.0002675

Simulation	Chlorophyll ($mg\ m^{-3}$)	Phytoplankton ($mm\ N\ m^{-3}$)	Zooplankton ($mm\ N\ m^{-3}$)
	Surface Average		
S1996-2000	0.475502	0.324395	0.24523
S2030-2034	0.509773	0.326619	0.253416
Difference	0.034271	0.002224	0.008186
	Total Basin Average		
S1996-2000	0.182921	0.0937727	0.0578883
S2030-2034	0.198421	0.0965047	0.0607803
Difference	0.0155	0.002732	0.002892

Simulation	Nitrate ($mm\ m^{-3}$)	Ammonium ($mm\ m^{-3}$)	Oxygen ($mm\ m^{-3}$)	Alkalinity ($me\ m^{-3}$)
	Surface Average			
S1996-2000	0.358487	0.260892	211.19	0.625956
S2030-2034	0.38448	0.275142	210.117	0.690485
Difference	0.025993	0.01425	-1.073	0.06453
	Total Basin Average			
S1996-2000	2.07094	0.185349	202.111	0.120679
S2030-2034	2.05868	0.207401	201.876	0.156915
Difference	-0.01226	0.022052	-0.235	0.036236

Simulation	Large Carb. Det. ($mm\ m^{-3}$)	Small Carb. Det. ($mm\ m^{-3}$)	Large Nitr. Det. ($mm\ m^{-3}$)	Small Nitr. Det. (mmm^{-3})
	Surface Average			
S1996-2000	0.922064	5.76495	0.10674	0.876642
S2030-2034	0.908812	5.82517	0.104834	0.88578
Difference	-0.013252	0.06022	-0.001906	0.009138
	Total Basin Average			
S1996-2000	0.734601	1.75939	0.0764984	0.268106
S2030-2034	0.748335	1.80262	0.0787836	0.27471
Difference	0.013734	0.04323	0.0022852	0.006604

TABLE 4.1: *Comparison of surface and total basin spatio-temporal averages of model variables for simulations 1996-2000 and 2030-2034*

Averages of chlorophyll concentration indicate a significant difference. A 0.0155 $mg\ m^{-3}$ and 0.34271 $mg\ m^{-3}$ increase in chlorophyll is calculated for the whole basin and surface, respecively. In other words, the concentration of chlorophyll approximately increased 8%

in the whole basin and 7% at the surface which can't be disregarded. Moreover, modes of signals in timeseries reveal that there is also some shifts in time scale of chlorophyll blooms (Fig. 4.38).

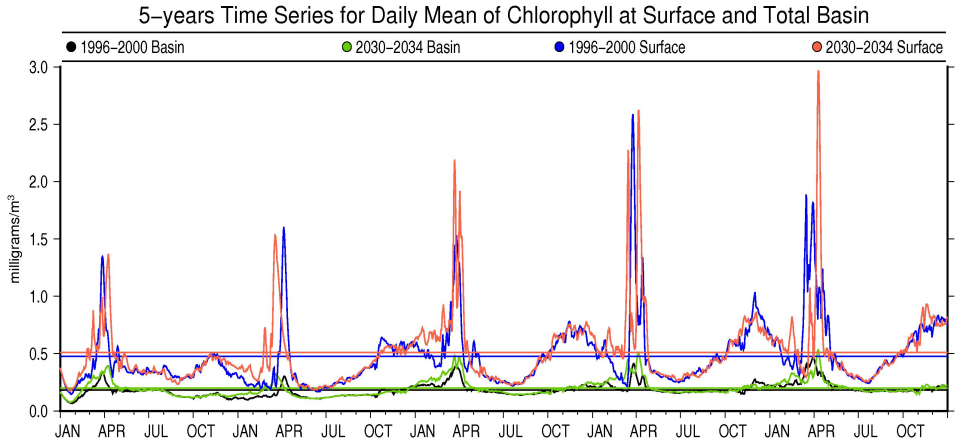

FIGURE 4.38: *Time series for daily spatial surface and basin average of chlorophyll along years 1996-2000 and 2030-2034*

Phytoplankton and zooplankton concentrations for each simulation changed slightly (Fig. 4.39 and 4.40). Periods of blooms have shifted as in chlorophyll but lesser. The differences between each model run are very small for both the surface and basin averages (Table 4.1).

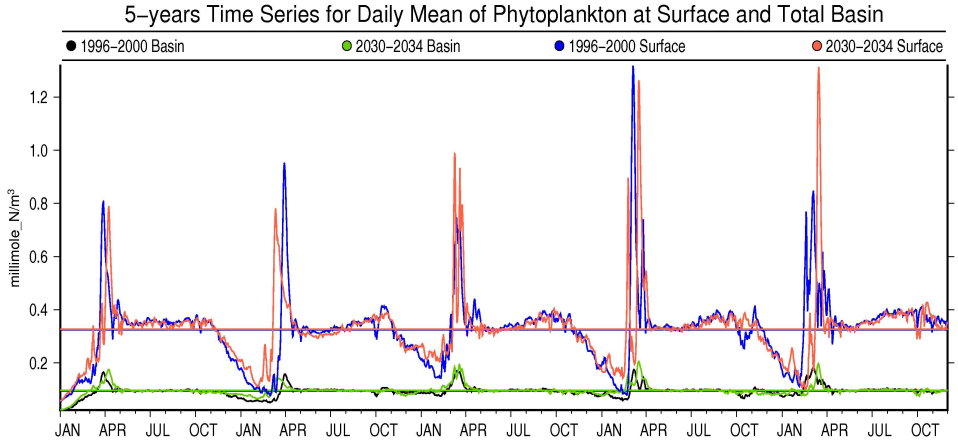

FIGURE 4.39: *Time series for daily spatial surface and basin average of phytoplankton along years 1996-2000 and 2030-2034*

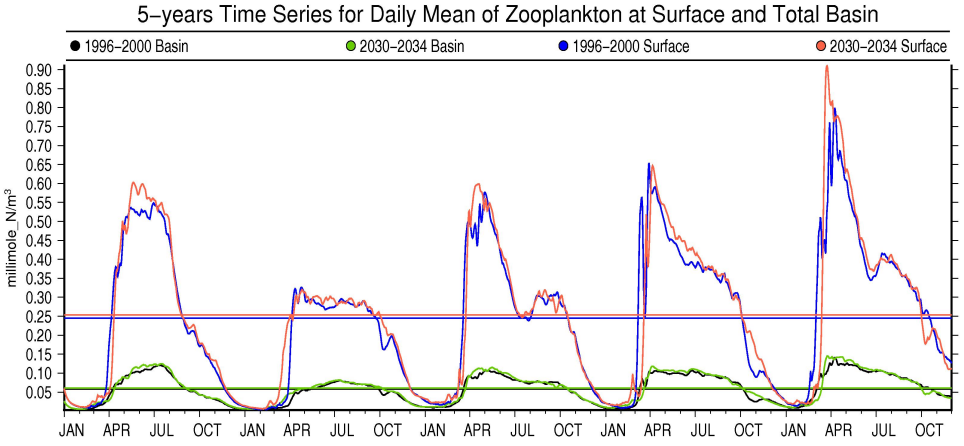

FIGURE 4.40: *Time series for daily spatial surface and basin average of zooplankton along years 1996-2000 and 2030-2034*

The nitrate abundance of the total basin decreased by -0.01226 $mm\ m^{-3}$, while an increase of 0.026 $mm\ m^{-3}$ was predicted at the surface for 2030-2034 (Fig. 4.41). Ammonium variability is more unstable than it is for nitrate. There is significant differences between the two simulations in terms of ammonium concentration. At the sea surface, an increase of approximately 5% is estimated whereas 0.12% of increase is expected for whole basin (Fig. 4.42).

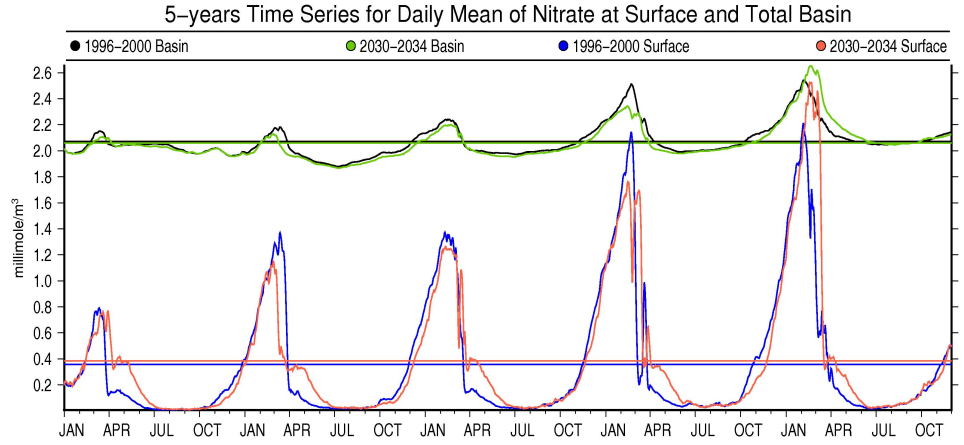

FIGURE 4.41: *Time series for daily spatial surface and basin average of nitrate along years 1996-2000 and 2030-2034*

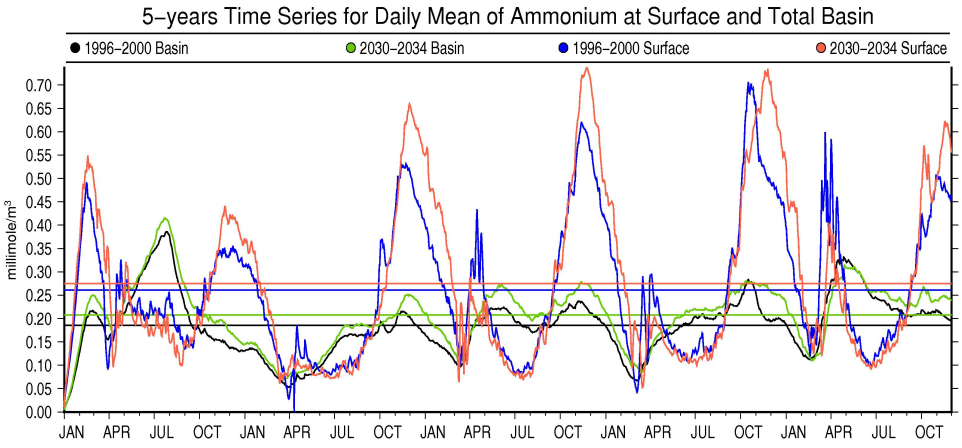

FIGURE 4.42: *Time series for daily spatial surface and basin average of ammonium along years 1996-2000 and 2030-2034*

4.7 Improvements for Hydrodynamical Model

Different horizontal and vertical mixing schemes are utilized to test the sensitivity of the model (Table 3.3). Test run2009-110714 is configured as 5-years simulations with different atmospheric forcing dataset (Section 3.3.4). Basin and surface averages of hydrodynamical variables are calculated and results are presented below.

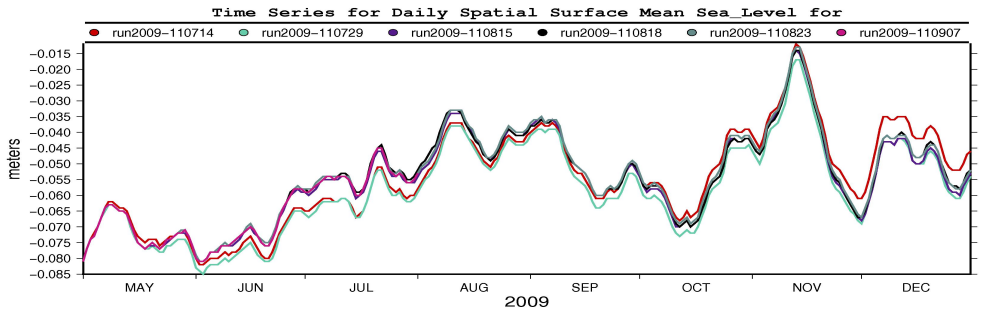

FIGURE 4.43: *Spatial average of sea level height for hydrodynamic test simulations*

Change in viscosity and diffusivity, and activated longwave switch starts to effect sea level after October when relatively strong mixing occurs (see Fig. 4.43, run2009-110714 and run 2009-110729). The model results in a relatively higher sea level with other mixing schemes than LMD except in December.

The magnitute of the basin mean velocity is almost unchanged for each test simulations (Fig. 4.44). However, there is differentiation at the surface before and after August. Reference simulation (run2009-110714) has lower surface current speed that all others, but run2009-110729 before August. In August and beginning of September all simulations have resulted in approximate velocities. Thereafter, all the tests have managed to lower surface current speed with respect to reference simulation.

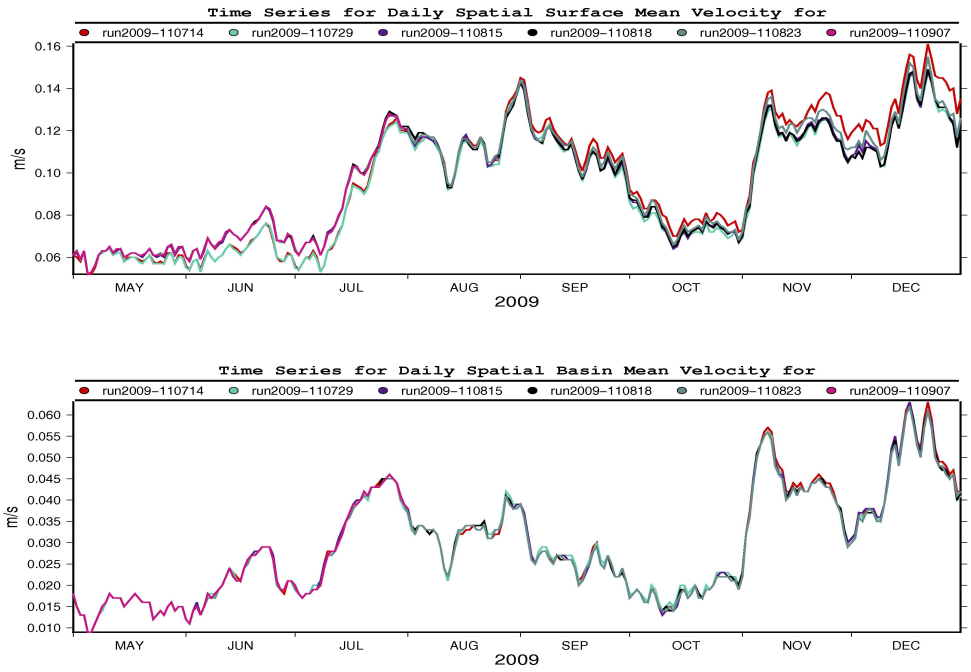

FIGURE 4.44: *Time series for spatial average of surface and basin current velocity for hydrodynamic test simulations*

Temperature and salinity averages for both surface and basin are obviously high for the reference simulation. Temperature reaches 32 °C at the surface and 17.9 °C for the whole basin (Fig. 4.45). It radically decreased when the longwave switch is activated. Moreover, changing the LMD mixing scheme to MY25 and GLS mixed surface water more effectively at vertical water column which reduced the surface water temperature a little bit more.

Observations and comments on temperature are valid also for salinity with a more dramatic relative change (Figure 4.46). Manipulations of the model setup resulted in a more reasonable salinity values. Furthermore, the slope of the the curve became more smooth. In other words, sharp gradients in salinity seem to be smoothed by the test configurations.

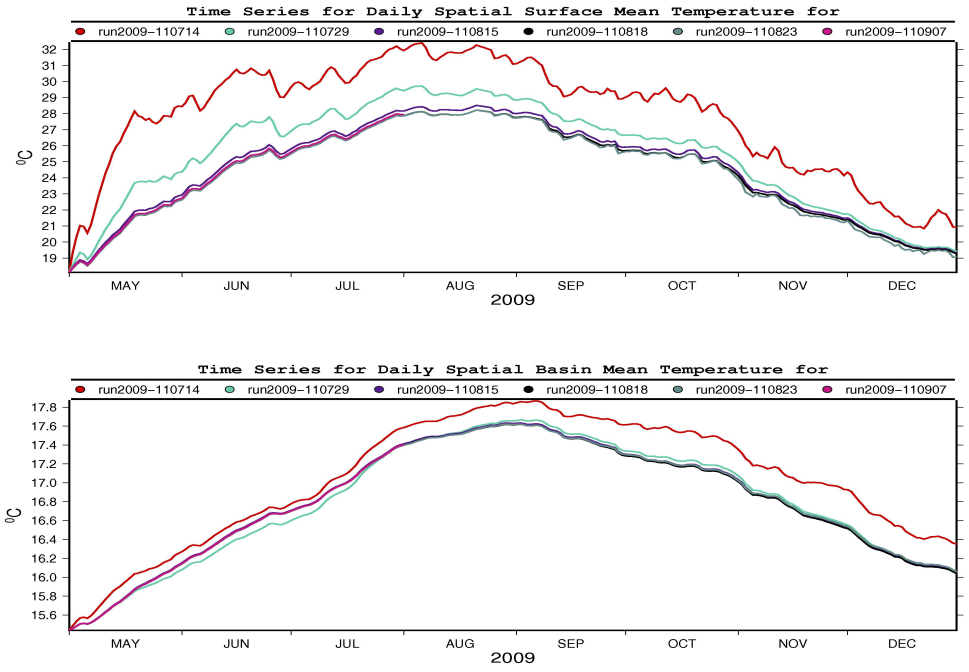

FIGURE 4.45: *Time series for spatial average of surface and basin temperature for hydrodynamic test simulations*

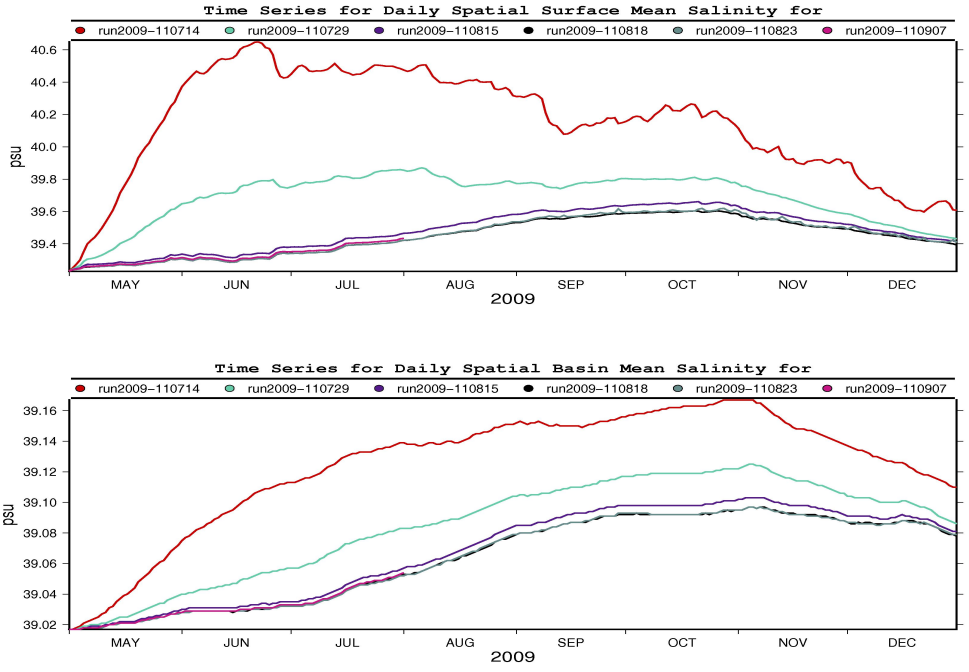

FIGURE 4.46: *Time series for spatial average of surface and basin salinity for hydrodynamic test simulations*

CHAPTER 5

DISCUSSIONS and CONCLUDING REMARKS

A three-dimensional model is utilized to see the space-time variations in hydrodynamics and biogeochemistry of Northern Levantine Sea. A 5-year hindcast is realized to see whether the model is successful to imitate the basin dynamics. Then a second 5-year forecast is demonstated to see the change of physical and ecosystem variables under different atmospheric conditions and river fluxes reflecting a climate change scenario. Although limited number of tests could be conducted due to computational expenses, attempts to model basic structures of study area are promising. Furthermore, despite coarse resolution of atmospheric data, significant signals of inter-annual variations detected.

General circulation patterns are well-represented in the model. Cyclonic character of permanent Rhodes gyre is captured in all interannual monthly averages. Moreover, domination of Asia Minor Current on the circulation is perpetuated. However, current speed seems to slightly overestimated. In addition these large-scale circulation features, well-known transitory mesoscale eddies such as West Cyprus eddy also appear in averages (Section 4.1). Sea surface height is in an acceptable range according to literature. However, comparison with satellite data reveals that AMC is highly influencial on regional variations of sea surface height. Path of AMC divides basin into two parts where coastal regions has positive sea level anomaly and negative anomalies dominate offshores which can be unrealistic. On the other-hand, satellite SLA may mislead due to low quality data.

Beside indicated promising outcomes for hydrodynamic structures, some important properties of region could not be formed by the model. Most significant of these deficits is Levantine Intermediate Water which seems to be skipped by model. A reason can be relatively low temperature in stratification seasons that may prevent formation of required Levantine Surface Water needed for the formation of LIW. On the other hand, it should be noted that

Zavatarelli and Mellor (1995) and *Alhammoud et al. (2005)* achieved this goal after a 10 years spinup following initialization. Because of that a longer runtime may be needed for LIW to be formed.

Eventhough problems in hydrodynamical model should be kept in mind, ecosystem results obtained by model are also encouraging. However, they urge to investigate ecosystem of the region with more care. Since phosphate and silicate are not available in Fennel model, some unrealistic results can be expected for some variables in order to tune some others. It has been seen that phytoplankton and zooplankton concentrations are more or less suited to regional characteristics which are cited in related section (4.5). However, inter-annual monthly averages point out that model surface chlorophyll concentration multiples related satellite data quantitively. But coastal and offshore patterns of chlorophyll mostly matches. Problem in surface chlorophyll distribution may be originated because of formation of deep chlorophyll maximum incorrectly with the configurations used in simulations. Since chlorophyll is a non-state variable of the model, in other words since it is directly propotional to phytoplankton biomass, this discrepancy is considered to be a consequence of the constant ρ_{chlo} that determines light attenuation and production-intensity (P-I) relation along water column in equations 2.26 and 2.27. Penetration of light into deeper levels will push deep chlorophyll maximum towards intermediate levels. Therefore, this may cause a reduction in chlorophyll concentration at the surface as expected. However, it should be admitted that with this configuration, model is far away from capturing ecosystem dynamics of the region.

Available nutrients are successfully represented quantitatively compared to basin properties described in literature. Monthly distribution of nitrate is negatively correlated with production as expected. Moreover, a nutricline is formed between 20-30 m successfully.

Climate change scenario (Section 4.6) applied to the model, has shortages which can prevent to have a healthy projection of the future situation of the Northern Levantine. Besides atmospheric forcings and riverine inputs, open boundary data could also be modified according to climate change scenarios realized by ocean climate models. Moreover, model could be initialized from the end of the hindcast run to have a closer initial data to the first day of forecast. In spite of these deficits, relative changes due to atmospheric variations and river fluxes merit attention.

Although atmospheric fluxes indicates a mild global warming conditions, significant responses of physical tracers to the atmospheric changes are determined in time series of daily spatial averages. Model computed considerable increase of temperature and salinity especially

at the surface level. Prediction for temperature is approximately a 0.33°increase and a rising of salinity by 0.035 psu is calculated. Some different fluctuation patterns appear in time series of sea level and velocity averages, however, considered information does not enough to get more understandings about possible changes in these variables.

Some of the ecosystem variables of the basin also gave significant resposes to different atmospheric and riverine forcings. Timeseries of spatial averages indicate variations in nutrient budgets most probably due to increse in river fluxes. Moreover, model predicted a 8% increase at surface chlorophyll and 7% increase in the whole basin. On the other hand, very slight changes were observed in zooplankton and phytoplankton concentrations. However, more statistical analysis should be conducted to understand indications and correlations between variables in a full scientific context.

Hydrodynamic tests applied to the model on mixing show that choosing mixing scheme is essential especially for temperature and salinity distributions. First test (run-110714) with LMD mixing scheme, configured as 5-year runs with different atmospheric dataset for different time period, overestimates regional characteristics. Although in terms of vertical mixing dynamics LMD seems to be the right choice for the region, tests show that high temperature and salinity at the surface occured because of the weak convection of radiation at the surface. Computing longwave radiation internally (run-110729) and using harmonic horizontal mixing scheme instead of biharmonic scheme lead more realistic tracer spatial averages. Shifting LMD scheme to MY25 (run-110815) plays a role to increase mixing of surface waters with intermediate waters more efficiently. GLS mixing schemes haven't changed the spatial averages dramatically. They result in more or less the same averages. To sum up, regarding regional properties, run-110729 with LMD vertical mixing, harmonic horizontal mixing and internal longwave calculation seems to be the best choice for the Northern Levantine Basin hydrodynamics. But, for sure, investigations should be deepened to validate with the best known features of the study area.

REFERENCES

[1] Alhammoud, B., K. Béranger, L. Mortier, M. Crépon and I. Dekeyser, 2005. Surface circulation of the Levantine Basin: Comparison of model results with observations, Progress In Oceanography, 66, 2-4, 299-320, doi:10.1016/j.pocean.2004.07.015

[2] Amitai, Y., Y. Lehahn, A. Lazar, and E. Heifetz (2010), Surface circulation of the eastern Mediterranean Levantine basin: Insights from analyzing 14 years of satellite altimetry data, J. Geophys. Res., 115, C10058, doi:10.1029/2010JC006147.

[3] Arakawa, A., Lamb, V.R., 1977. Methods of computational physics Academic Press 17, 174-265

[4] Bethoux J. P., 1979. Budgets of the Mediterranean Sea. Their dependence on the local climate and on the characteristics of the Atlantic Waters, Oceanol. Acta, 2 (1979), pp. 157-163

[5] Bethoux J.P., Morin P., Madec C., Gentili B., 1992. Phosphorus and nitrogen behaviour in the Mediterranean Sea, Deep Sea Research Part A, Oceanographic Research Papers, 39 (9) , pp. 1641-1654.

[6] Bissett, W.P., J.J. Walsh, D.A. Dieterle, K.L. Carder, 1999. Carbon cycling in the upper waters of the Sargasso Sea: I. Numerical simulation of differential carbon and nitrogen fluxes, Deep-Sea Res., 46, 205-269.

[7] Bozkurt, A., Göksu, L., Sarıhan, E. and Taşdemir, M., 2002. Asi Nehri rotifer faunası (Hatay-Türkiye), E.U. Su Ürünleri Dergisi, 19(1-2): 63-67.

[8] Budgell, W.P., 2005. Numerical simulation of ice-ocean variability in the Barents Sea region, Ocean Dynamics, DOI 10.1007/s10236-005-0008-3.

[9] Chapman, D. C., 1985. Numerical treatment of cross-shelf open boundaries in a barotropic coastal ocean model, J. Phys. Oceanogr., 15, 1060–1075.

[10] Demirov E., and N. Pinardi, 2002. Simulation of the Mediterranean Sea circulation from 1979 to 1993. Part I: The interannual variability, J. Mar. Syst., 33-34 (C): 23-50

[11] Durski, S., Glenn, S. and Haidvogel, D., 2004. Vertical mixing schemes in the coastal ocean: Comparison of the level 2.5 Mellor-Yamada scheme with an enhanced version of the K profile parameterization, Journal of Geophysical Research 109(C1): doi: 10.1029/2002JC001702. issn: 0148-0227.

[12] Ediger, D., Tuğrul, S., Yılmaz, A., 2005. Vertical profiles of particulate organic matter and its relationship with chlorophyll-a in the upper layer of the NE Mediterranean Sea, Journal of Marine Systems, 55 (3-4), pp. 311-326. doi: 10.1016/j.jmarsys.2004.09.003

[13] Eker-Develi, E., Kideys, A.E., Tuğrul, S., 2006. Role of Saharan dust on phytoplankton dynamics in the northeastern Mediterranean, Marine Ecology-Progress Series, 314, pp. 61-75

[14] Eppley, R. W., 1972. Temperature and phytoplankton growth in the sea Fish. Bull. 70, 1063-1085

[15] Evans, G. T., and J. S. Parslow 1985. A model of annual plankton cycles Biol. Oceanogr. 3, 327-347.

[16] Fasham, M. J. R., Ducklow, H. W., McKelvie, S. M., 1990. A nitrogen-based model of plankton dynamics in the oceanic mixed layer Journal of Marine Research 48(3), Sears Foundation for Marine Research. 591-639.

[17] Fennel, K., Wilkin, J., Levin, J., Moisan, J., O'Reilly, J., Haidvogel, D., 2006. Nitrogen cycling in the Middle Atlantic Bight: Results from a three-dimensional model and implications for the North Atlantic nitrogen budget. Global Biochem. Cycles 20, GB3007, doi:10.1029/2005GB002456

[18] Fiechter, J., A.M. Moore, C.A. Edwards, K.W. Bruland, E. Di Lorenzo, C.V.W. Lewis, T.M. Powell, E. Curchitser and K. Hedstrom, 2009. Modeling iron limitation of primary production in the coastal Gulf of Alaska, Deep Sea Res. II

[19] Flather, R. A., 1976: A tidal model of the northwest European continental shelf. "Memoires de la Societe Royale de Sciences de Liege, 6, 141-164.

[20] Galperin, B., L. H. Kantha, S. Hassid, and A. Rosati, 1988: A quasi-equilibrium turbulent energy model for geophysical flows, J. Atmos. Sci., 45, 55-62.

[21] Haidvogel, D.B., Arango, H.G., Hedstorm, K., Beckmann, A., Malanotte-Rizzoli, P., Shchepetkin, A.F., 2000. Model evaluation experiments in the North Atlantic Basin: simulations in nonlinear terrain-following coordinates. Dynam. Atmos. Oceans 32, 239-281

[22] Haidvogel, D.B., Arango, H.G., Budgell, W.P., Cornuelle, B.D., Curchitser, E., Di Lorenzo, E., Fennel. K., Geyer, W.R., Hermann, A.J., Lanerolle, L., Levin, J., McWilliams, J.C., Miller, A.J., Moore A.M., Powell, T.M., Shchepetkin, A.F., Sherwood, C.R., Signell, R.P., Warner, J.C., Wilkin, J., 2008. Ocean forecasting in terrain-following coordinates: Formulation and skill assessment of Regional Ocean Modelling System. Jour. Comp. Physics 227, 3596-3624

[23] Hamad, N., Millot, C., and Taupier-Letage, I. 2006. The surface circulation in the eastern basin of the Mediterranean Sea. Scientia Marina, 70(3): 457-503 doi: 10.3989/scimar.2006.70n3457

[24] Hedström, K.S., 2009. Technical Manual for a Coupled Sea-Ice/Ocean Circulation Model (Version 3) Arctic Region Supercomputing Center University of Alaska Fairbanks, 1-36

[25] Jackett, D. R. and T. J. McDougall, 1995. Minimal Adjustment of Hydrostatic Profiles to Achieve Static Stability J. Atmos. Oceanic Techn., 12, 381-389.

[26] Krom, M. D., Kress, N., Brenner, S., Gordon, L. I., 1991. Phosphorus limitation of primary productivity in the eastern mediterranean sea, Limnology and Oceanography, 36(3), 424-432.

[27] Krom, M. D., Herut, B., and Mantoura, R. F. C., 2004. Nutrient budget for the eastern mediterranean: Implications for phosphorus limitation, Limnology and Oceanography, 49(5), 1582-1592.

[28] Krom, M.D., Emeis, K-C, Van Cappellen, P., 2010. Why is the Eastern Mediterranean phosphorus limited?, Progress In Oceanography, Volume 85, Issues 3-4, Pages 236-244

[29] Large, W. G., J. C. McWilliams, and S. C. Doney, 1994. Oceanic vertical mixing: a review and a model with a nonlocal boundary layer parameterization Rev. Geophys., 32, 363-403.

[30] Larnicol, G., Ayoub, N., Le Traon, P. Y., 2002. Major changes in mediterranean sea level variability from 7 years of TOPEX/Poseidon and ERS-1/2 data, Journal of Marine Systems, 33-34, 63-89

[31] Lascaratos, A., R.G. Williams, and E. Tragou, 1993. A Mixed-layer Study of the Formation of Levantine Intermediate Water, Journal of Geophysical Research, 98, C8, 14739-14749.

[32] Lima, I. D., and S. C. Doney, 2004. A three-dimensional, multinutrient, and size-structured ecosystem model for the North Atlantic Global Biogeochem. Cycles, 18, GB3019, doi:10.1029/2003GB002146.

[33] Lionello, P., Malanotte-Rizzoli, P., Boscolo, R., Alpert, P., Artale, V., Li, L., Luterbacher, J., May, W., Trigo, R., Tsimplis, M., Ulbrich, U., Xoplaki, E. The Mediterranean climate: An overview of the main characteristics and issues Developments in Earth and Environmental Sciences, Volume 4, 2006, Pages 1-26

[34] Ludwig, W., Dumont, E/. Meybeck, M., Heussner, S., 2009. River discharges of water and nutrients to the Mediterranean and Black Sea: Major drivers for ecosystem changes during past and future decades? Progress in Oceanography, 80 (3-4). 199-217.

[35] Malanotte-Rizzoli P., Manca B.B., D'Alcala M.R., Theocharis A., Brenner S., Budillon G., Ozsoy E., 1999. The Eastern Mediterranean in the 80s and in the 90s: The big transition in the intermediate and deep circulations, Dynamics of Atmospheres and Oceans, 29 (2-4) , pp. 365-395.

[36] Manca, B., Burca, M., Giorgetti, A., Coatanoan, C., Garcia, M. J., Iona, A., 2004. Physical and biochemical averaged vertical profiles in the Mediterranean regions: an important tool to trace the climatology of water masses and to validate incoming data from operational oceanography Journal of Marine Systems, Volume 48, Issues 1-4, Pages 83-116

[37] Marchesiello, P., J. C. McWilliams, A. F. Shchepetkin, 2001. Open boundary conditions for long-term integration of regional ocean models Ocean Modelling, 3, 1-20

[38] May, P. W., 1983. Climatological Flux Estimates in the Mediterranean Sea Air Sea Fluxes. NORDA Rep., 58, vol. 2Nav. Ocean Res. Dev. Activ., NSTL Station, Mississippi 39529 (1983), p. 65

[39] Milliff, R.F. and Robinson, A,R., 1992. Structure and dynamics of the Rhodes Gyre system and dynamical interpolation for estimates of mesoscale variability, J. Physical Oceanogr., 22(4), 317-337.

[40] Morcos, S.A., 1972. Sources of Mediterranean intermediate water in the Levantine Sea. In Studies in Physical Oceanography, a Tribute to Georg Wüst on his 80th Birthday, Edited by Arnold A. Gordon, Gordon and Breach, New-York, 2 185-206

[41] Nakicenovic, N., Swart, R. (Eds.), 2000. Special Report on Emissions Scenarios. A Special Report of Working Group III of the Intergovernmental Panel on Climate Change. Cambridge University Press, Cambridge, UK.

[42] Orlanski, I., 1976. A simple boundary condition for unbounded hyperbolic flows. J. Comp. Sci., 21(3), 251-269.

[43] Ovchinnikov, I. M., 1966. Circulation in the surface and intermediate layers of the Mediterranean, Oceanology, 6, 48-57

[44] Özsoy, E. 1981. On the atmospheric factors affecting the Levantine Sea. European Centre for Medium Range Weather Forecasts,. Technical Report No. 25, 29p.

[45] Özsoy, E., Hecht, A. and Ünlüata, Ü. 1989. Circulation and Hydrography of the Levantine Basin. Results of POEM Coordinated Experiments 1985-1986, Prog. Oceanogr., bf 22 125-170.

[46] Özsoy, E., Hecht, A., Ünlüata, Ü. and Brenner, S., Sur, H. I., Bishop, J., Latif M. A., Rozentraub, Z., and Oğuz, T. 1993. A synthesis of the Levantine basin circulation and hydrography, 1985-1990. Deep Sea Res. 40 6, pp. 1075-1119

[47] Özsoy, T., Türkoğlu, E., Doğan, A., Serin, D. S., 2008. A Study of Ionic Composition and Inorganic Nutrient Fluxes from Rivers Discharging into the Cilician Basin, Eastern Mediterranean, Environmental Monitoring and Assessment, 145(1-3), pp. 17-29, doi:10.1007/S10661-007-0013-8.

[48] Parker, R. A. 1993. Dynamic models for ammonium inhibition of nitrate uptake by phytoplankton Ecol. Modell. 66, 113 - 120.

[49] Petihakis, G., Triantafyllou, G., Tsiaras, K., Korres, G., Pollani, A., and Hoteit, I., 2009. Eastern Mediterranean biogeochemical flux model - Simulations of the pelagic ecosystem, Ocean Sci., 5, 29-46, doi:10.5194/os-5-29-2009.

[50] The POEM Group, 1992. General circulation of the Eastern Mediterranean Earth-Science Rev., 32, pp. 285-309

[51] Powell, T. M., C.V. W. Lewis, E. Curchitser, D. Haidvogel, A. Hermann, and E. Dobbins. 2006. Results from a three-dimensional, nested biological-physical model of the California Current System: Comparisons with Statistics from Satellite Imagery. J. Geophys. Res., 111, C07018, doi:10.1029/2004JC002506.

[52] Reiter, E. R., 1975: Handbook for Forecasters in the Mediterranean.Tech. Pap. 5-75, 344 p. Nav. Postgrad. Sch., Monterey, Ca.

[53] Robinson, A.R., W.G. Leslie, A. Theocharis and A. Lascaratos. 2001. Mediterranean Sea Circulation Encyclopedia of Ocean Sciences. Academic Press, 1689-1706, doi:10.1006/rwos.2001.0376

[54] Shchepetkin, A. F., and J. C. McWilliams, 2005. The Regional Ocean Modeling System: A split-explicit, free-surface, topography following coordinates ocean model Ocean Modelling, 9, 347-404.

[55] Umlauf, L., H. Burchard, 2003. A generic length-scale equation for geophysical turbulence models J. Marine Res., 61, 235-265.

[56] Warner, J. C., C. R. Sherwood, H. G. Arango, and R. P. Signell, 2005. Performance of four turbulence closure methods implemented using a generic length scale method Ocean Modelling, 8, 81-113.

[57] Warner, J. C., C. R. Sherwood, R. P. Signell, C. K. Harris, and H. G. Arango, 2008. Development of a three-dimensional, regional, coupled wave, current, and sediment-transport model, Computers & Geosciences, 34, 1284-1306.

[58] Wu, P., and Haines K., 1998. The general circulation of the Mediterranean Sea from a 100-year simulation, J. Geophys. Res., 103(C1), 1121-1135, doi:10.1029/97JC02720.

[59] Wüst, G., 1961. On the Vertical Circulation of the Mediterranean Sea, J. Geophys. Res., 66(10), 3261-3271, doi:10.1029/JZ066i010p03261.

[60] Yılmaz, A. and Tuğrul, S. 1998. The effect of cold- and warm-core eddies on the distribution and stoichiometry of dissolved nutrients in the northeastern mediterranean, Journal of Marine Systems, 16(3-4), 253-268.

[61] Zavatarelli M., Mellor G. L. 1995. A numerical study of the Mediterranean Sea circulation. Journal of Physical Oceanography, 25(6), 1384-1414.

Appendix A

LIST OF ABBREVIATIONS

ADW	Adriatic Deep Water	ALERMO	Aegean-Levantine Regional Model
AMC	Asia Minor Current		
AW	Atlantic Water	CLBC	Central Levantine Basin Current
CMCC	Centro Euro-Mediterraneo per i Cambiamenti Climatici	DCM	Deep Chlorophyll Maximum
EMDW	Eastern Mediterranean Deep Water	GEBCO	General Bathymetric Chart of Oceans
GLS	Generic Length Scale	KPP	K-profile Parametrization
LDW	Levantine Deep Water	LIW	Levantine Intermediate Water
LMD	Large McWilliams Doney Parametrization	LSW	Levantine Surface Water
MAW	Modified Atlantic Water	MPDATA	Multidimensional Positive Definite Advection Transport Algorithm
MPI	Message Passing Interface	NASA	National Aeronautics and Space Administration of USA
NetCDF	Network Common Data Form	NOAA	National Oceanic and Atmospheric Administration of USA
OGS	Istituto Nazionale di Oceanografia e di Geofisica Sperimentale	OpenMP	Open Multi-Processing
POEM	Physical Oceanography of Eastern Mediterranean	ROMS	Regional Ocean Modelling System
SLA	Sea Level Anomaly	SSH	Sea Surface Height
SST	Sea Surface Temperature	UTOPIA	Uniformly Third-Order Polynomial Interpolation Algorithm

Appendix B

BIOGEOCHEMISTRY cont'd

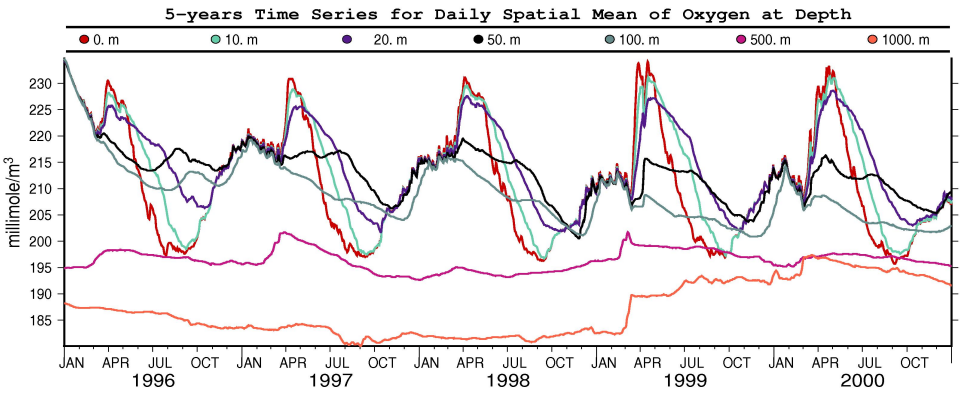

FIGURE B.1: *Time series for daily spatial MEAN of oxygen between 1996 and 2000 at depths 0m, 10m, 20m, 50m, 100m, 500m, 1000m*

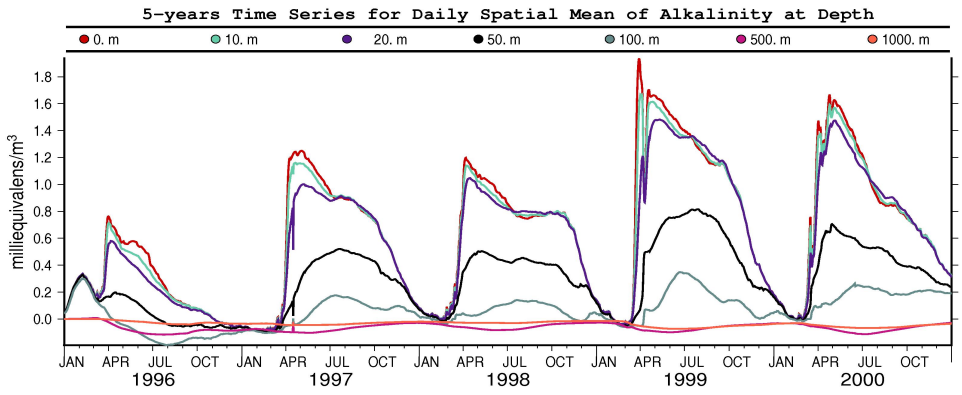

FIGURE B.2: *Time series for daily spatial MEAN of alkalinity between 1996 and 2000 at depths 0m, 10m, 20m, 50m, 100m, 500m, 1000m*

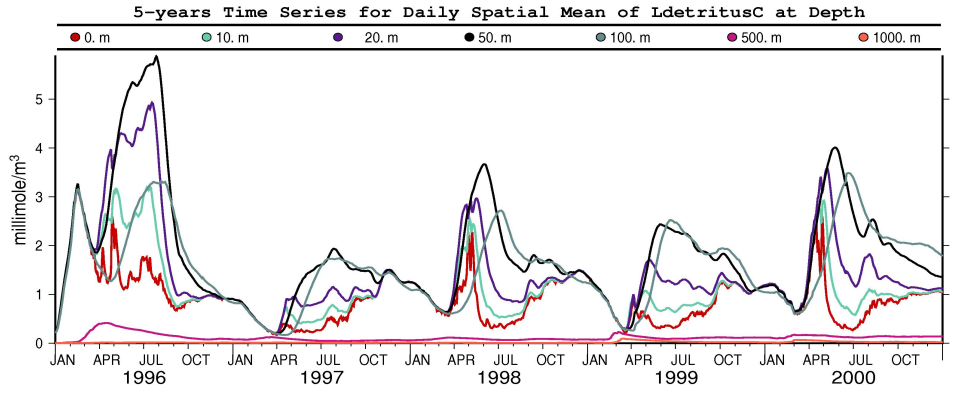

FIGURE B.3: *Time series for daily spatial MEAN of large carbon detritus between 1996 and 2000 at depths 0m, 10m, 20m, 50m, 100m, 500m, 1000m*

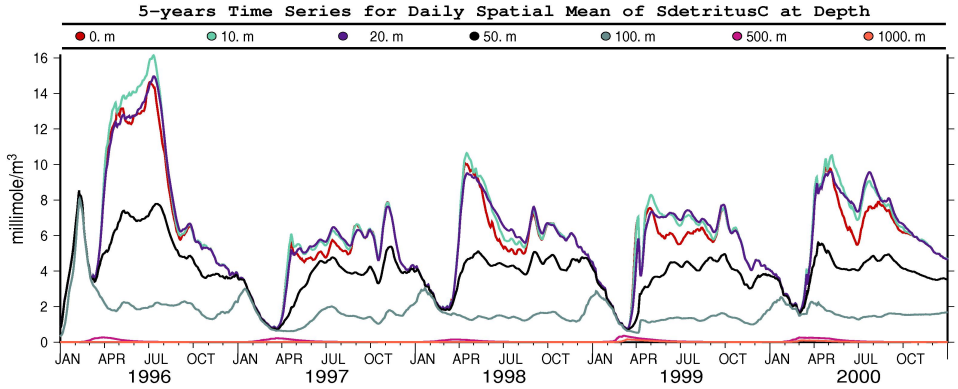

FIGURE B.4: *Time series for daily spatial MEAN of small carbon detritus between 1996 and 2000 at depths 0m, 10m, 20m, 50m, 100m, 500m, 1000m*

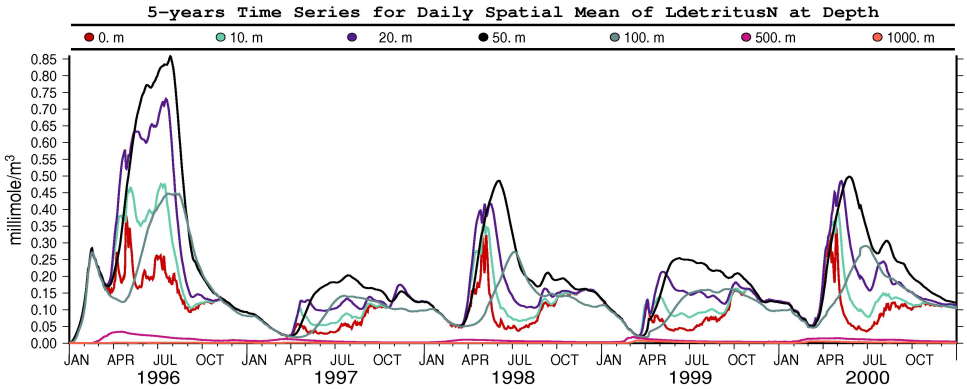

FIGURE B.5: *Time series for daily spatial MEAN of large nitrogen detritus between 1996 and 2000 at depths 0m, 10m, 20m, 50m, 100m, 500m, 1000m*

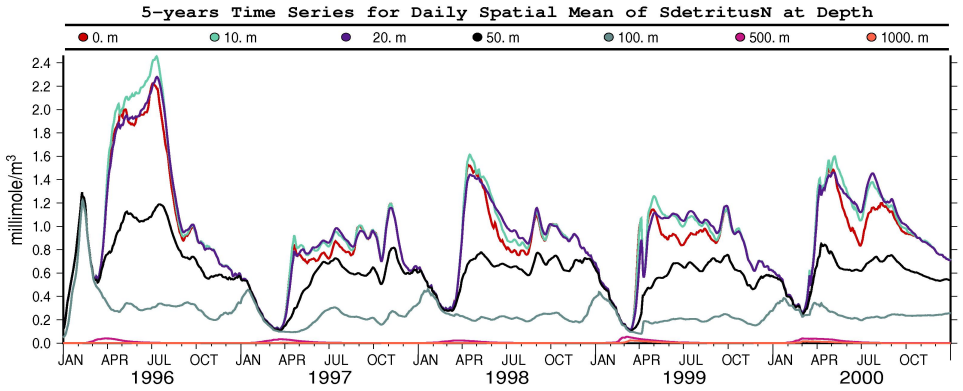

FIGURE B.6: *Time series for daily spatial MEAN of small nitrogen detritus between 1996 and 2000 at depths 0m, 10m, 20m, 50m, 100m, 500m, 1000m*

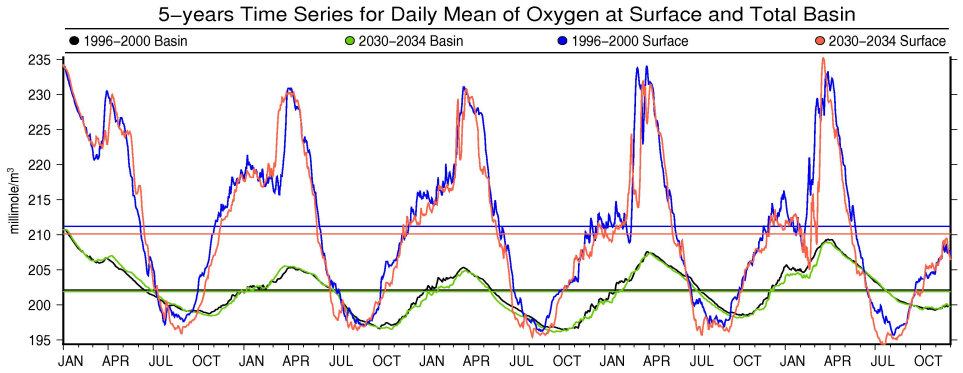

FIGURE B.7: *Time series for daily spatial surface and basin average of oxygen along years 1996-2000 and 2030-2034*

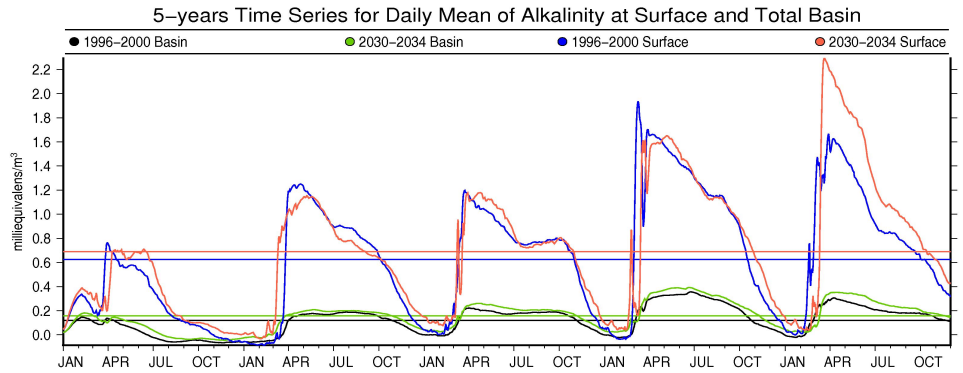

FIGURE B.8: *Time series for daily spatial surface and basin average of alkalinity along years 1996-2000 and 2030-2034*

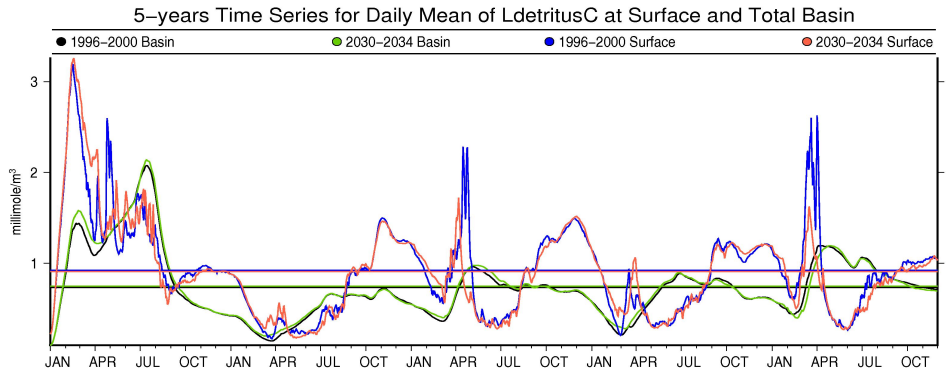

FIGURE B.9: *Time series for daily spatial surface and basin average of large carbon detritus along years 1996-2000 and 2030-2034*

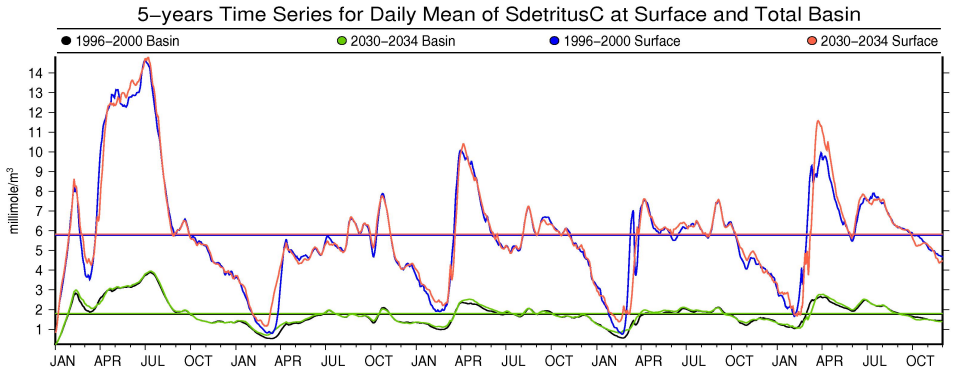

FIGURE B.10: *Time series for daily spatial surface and basin average of small carbon detritus along years 1996-2000 and 2030-2034*

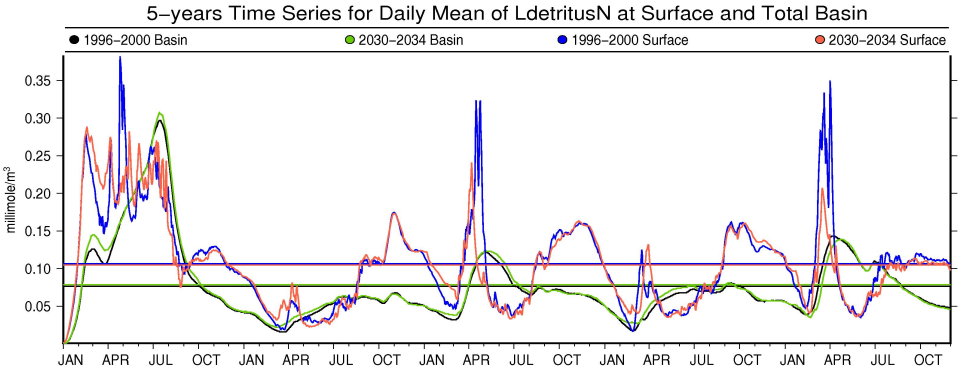

FIGURE B.11: *Time series for daily spatial surface and basin average of large nitrogen detritus along years 1996-2000 and 2030-2034*

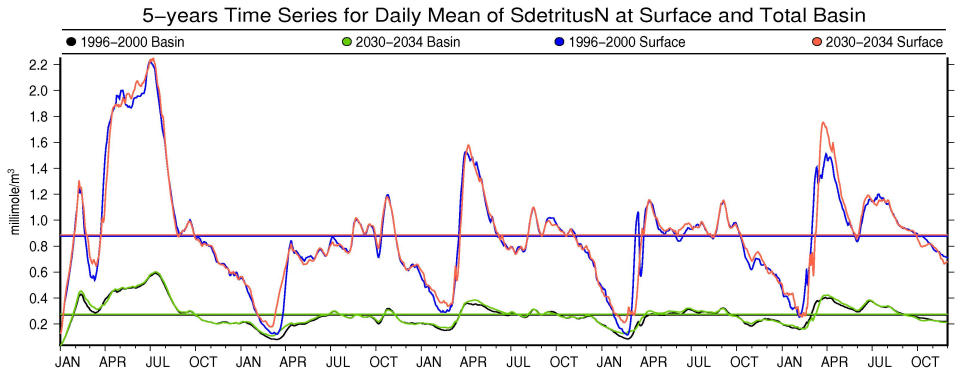

FIGURE B.12: *Time series for daily spatial surface and basin average of small nitrogen detritus along years 1996-2000 and 2030-2034*